2D and 3D Segmentation of Medical Images

Jonathan-Lee Jones

Submitted to Swansea University in fulfilment
of the requirements for the Degree of Doctor of Philosophy

Swansea University
Prifysgol Abertawe

Department of Computer Science

Swansea University

2015

Declaration

This work has not been previously accepted in substance for any degree and is not being concurrently submitted in candidature for any degree.

Signed   .... (candidate)

Date   ....

Statement 1

This thesis is the result of my own investigations, except where otherwise stated. Other sources are acknowledged by footnotes giving explicit references. A bibliography is appended.

Signed   .... (candidate)

Date   ....

Statement 2

I hereby give my consent for my thesis, if accepted, to be available for photocopying and for inter-library loan, and for the title and summary to be made available to outside organisations.

Signed   .... (candidate)

Date   ....

Abstract

Cardiovascular disease is one of the leading causes of the morbidity and mortality in the western world today. Many different imaging modalities are in place today to diagnose and investigate cardiovascular diseases. Each of these, however, has strengths and weaknesses. There are different forms of noise and artifacts in each image modality that combine to make the field of medical image analysis both important and challenging. The aim of this thesis is develop a reliable method for segmentation of vessel structures in medical imaging, combining the expert knowledge of the user in such a way as to maintain efficiency whilst overcoming the inherent noise and artifacts present in the images. We present results from 2D segmentation techniques using different methodologies, before developing 3D techniques for segmenting vessel shape from a series of images. The main drive of the work involves the investigation of medical images obtained using catheter based techniques, namely Intra Vascular Ultrasound (IVUS) and Optical Coherence Tomography (OCT). We will present a robust segmentation paradigm, combining both edge and region information to segment the media-adventitia, and lumenal borders in those modalities respectively. By using a semi-interactive method that utilizes "soft" constraints, allowing imprecise user input which provides a balance between using the user's expert knowledge and efficiency. In the later part of the work, we develop automatic methods for segmenting the walls of lymph vessels. These methods are employed on sequential images in order to obtain data to reconstruct the vessel walls in the region of the lymph valves. We investigated methods to segment the vessel walls both individually and simultaneously, and compared the results both quantitatively and qualitatively in order obtain the most appropriate for the 3D reconstruction of the vessel wall. Lastly, we adapt the semi-interactive method used on vessels earlier into 3D to help segment out the lymph valve. This involved the user interactive method to provide guidance to help segment the boundary of the lymph vessel, then we apply a minimal surface segmentation methodology to provide segmentation of the valve.

Acknowledgements

It would be very remiss of me to start the acknowledgements chapter of my thesis without thanking my supervisor, Dr. Xianghua Xie. I consider myself lucky to have him as my supervisor, for he has always gone out of his way to help whenever he can. His support throughout this endeavor has not only made this document possible, but has brought me to where I am today. During the progress of this PhD, he has always been there to provide aid with any difficulties, and has inspired me see problems in a different light, and to nudge me in the right direction as needed. Without his tireless help and encouragement, this thesis would not have been possible, and he has all my thanks for that. I am also grateful to my other supervisor, Dr. Rita Borgo for her help and support.

I would also like express my gratitude to my colleagues that have worked with me in the lab during my PhD, and have always been there to bounce ideas off: Jinjing Deng, Dr. Feng Zhao, Robert Palmer, Mike Edwards. A most heartfelt thankyou goes to my colleague and friend Dr. Ehab Essa, who has provided valuable insight and support throughout this PhD and the MSc before it, without his genuine kindness and help, a lot of the programming skills I now take for granted I wouldn't have developed. I wish him the best of luck in his new endeavor.

A special thankyou to my family, especially my mother (who works far too hard, and deserves a lot of praise)and my wife, Yun, who have supported me throughout my PhD and not been too harsh on me when I have spent odd hours working and not been the best of company. Thanks also to my friends Ceri and Aron who have distracted me when things have got stressful, and always been there when I needed to vent. Thanks especially to Ceri, for providing me with the programming anecdote I always use when teaching people JAVA.

When I was growing up, and heading to university, my Father always had faith in me, supported me through everything, went without so that I may have. It was his dream that I make something of my life, and he knew, even when I did not, that one day I would have my doctorate. I would like to dedicate my thesis to the memory of my father, as without him none of it would be possible.

Table of Contents

List of Tables

List of Figures

Assessment Metrics

Contents

Hausdorff Distance - HD

This is a measurement of how close two sets of points are to each other. The HD represents the distance from one point (pixel) in one set, to the corresponding point (pixel) in the compared set. It is therefore a metric to compare the accuracy of a segmentation, as it looks at the mean distance of a pixel from its corresponding pixel in the compared set (in most cases the ground Truth).

Area Overlap Ratio - AOR

The AOR is a similarity measure used in this work, and is related to the Jaccard index. The AOR measures the area of overlap between two sets (in this case the area of the segmentation and that of the ground truth). AOR is defined as the size of the intersection betwwen the two sets, divided by the smaller of the size of the two sets.

$$\text{overlap } (G_T, R_S) = \frac{|G_T \cap R_S|}{min \ (|G_T|, |R_S|)} \tag{1}$$

where G_T and R_S in our case represent the Ground Truth and the Segmentation result respectively.

Specificity

Specificity, also known as the true negative rate, is measures the proportion of negatives that are correctly identified as such. i.e It is a measure of the amount of True Negatives, and therefore

quantifies the avoidance of false positives.

$$\text{Specificity } TNR = \frac{TN}{N} \tag{2}$$

$$\text{Specificity } TNR = \frac{TP}{TP + FP} \tag{3}$$

where TNR is the True Negative Rate, TN are true Negatives, N are all Negatives, and FP are False Positives.

Sensitivity

The Sensitivity, also known as true positive rate, is a measure of the proportion of correctly identified true positives, and it therefore quantifies the avoidance of false negatives.

$$\text{Sensitivity } TPR = \frac{TP}{P} \tag{4}$$

$$\text{Sensitivity } TPR = \frac{TP}{TP + FN} \tag{5}$$

where TPR is the True Positive Rate, TP are true Positives, P are all positives, and FN are False Negatives.

Accuracy

Accuracy is a measure of the number of correct (true) results, both positive and negative, over the total number of cases recorded. This means that an accuracy of 100% represents all the recorded values (both positive and negative) being correct.

$$ACC = \frac{(TP + TN)}{(TP + FP + FN + TN)} \tag{6}$$

where ACC represents accuracy, TP and FP are true and false positives respectively, and TN and FN are true and false negatives likewise.

Chapter 1

Introduction

Contents

The main goal of the work was to provide a stable and efficient image segmentation method for medical images. In that respect, throughout this work, we concentrate on medical applications (although in some cases real world data is used to demonstrate versatility). Image segmentation has become ubiquitous across many fields in many different research approaches; such as computer vision [28, 29, 30], motion tracking [31, 32, 33], pattern recognition [34, 35, 36] and medical imaging [37, 38, 39]. In fact, it finds common usage in many applications where there is a need to separate objects from the image, or classification of different regions is paramount. In the modern world, image segmentation has become so ubiquitous a method that it is often included in all manner of software packages, and often we take its use for granted. As with other technologies, medical imaging techniques have advanced a considerable amount since their inception. Today we use a plethora of imaging techniques for diagnostics, prognosis and to aid in treatment. In the field of cardiology alone, X-ray, magnetic resonance imaging (MRI), ultrasound and optical coherence tomography (OCT) are becoming more and more common [40, 41, 42]. Cardiology is of vital importance as cardiovascular disease (CVD) is one of the

main causes of mortality in the developed world [1, 43]. Although cardiologists have a wide variety of imaging modalities and techniques at their disposal, all suffer (to a greater or lesser extent) from noise and image artifacts. It is therefore of utmost importance, in this field to be ale to provide a suitable wide ranging selection of image processing tools, such as image segmentation [44, 45, 46], registration and reconstruction of images [47, 48, 49, 50], and image enhancement [51, 52]. The main body of this thesis concerns itself with investigating and developing a semi-interactive approach to segmentation of artery walls from images obtained through IVUS and OCT modalities. Once this has been achieved, the methodology will be expanded on to provide a tool for 3D reconstruction of vessels of rat lymph vessels, from images obtained from confocal microscopy. Less work has been carried out on the segmentation of the lymphatic system, and lymphoedema (caused by a blockage or failure in the system) can lead to serious illness and be a sign of a greater underlying problem [53, 54] and have even been linked to cardiovascular disease [55].

1.1 Aims

1. To provide a stable and efficient segmentation method that can be used in different medical applications, but specifically the IVUS and OCT modalities to segment images. The aim is to provide segmentation support for the cardiology field, optimized for two common imaging modalities.

2. To further develop a segmentation method to act on 3D medical images, specifically those of Lymph Vessels obtained by confocal microscopy.

3. To reconstruct lymph valve regions in 3D, using segmentation techniques to reconstruct both the wall and lymph valve.

1.2 Motivation

One of the main driving forces in this work was to investigate how imaging techniques could be applied to investigate vessel structure segmentation. As cardiovascular disease is so prevalent in the Western world, the main body is dedicated to the study of coronary arteries (although, as we show, the technique can be utilised in other applications), with further study of the
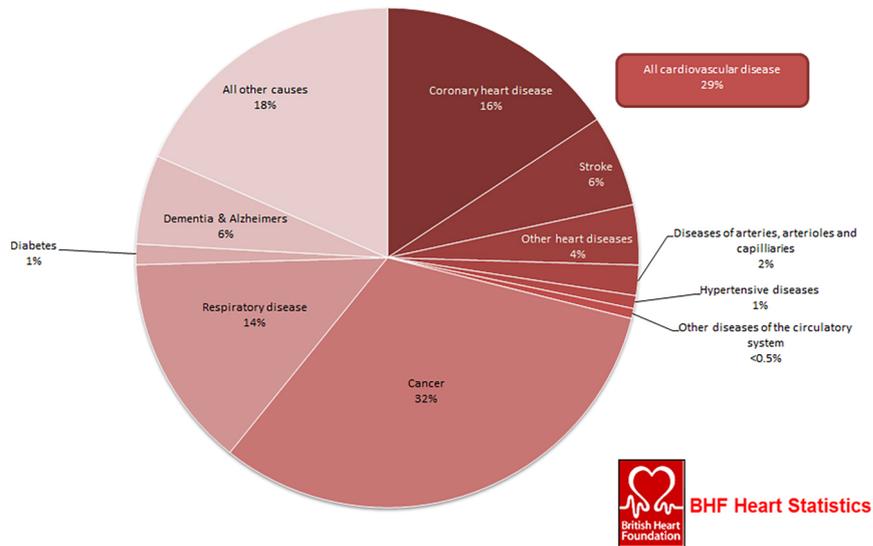
Figure 1.1: Mortality statistics for UK in 2012, adapted from [1] study by the British Heart Foundation.

lymphatic system, which is another cause of decrease quality of life, and can be linked to other disease states.

Cardiovascular disease is a major cause of death and morbidity in the world today [1, 43], and in Britain alone accounts for almost 30% of deaths Fig. 1.1, and almost 10% of hospital inpatient visits Fig. 1.2, which creates an extensive demand on hospital staff time and resources, even in minor cases. The heart is, at its most simple, a pump that pushes blood around our body. It is however, much more than that. The heart is a specially adapted muscle that maintains a contraction and relaxation cycle throughout our entire life. In order to maintain this workload, the heart needs to have its own supply of blood to the muscles that make up its walls. This is the function of the coronary arterial network. Coronary artery disease (otherwise known as ischaemic heart disease) is a serious disease, leading to large numbers of deaths, especially in men worldwide [56]. One of its causes is a thickening or occlusion of the coronary artery walls, by formation of plaques. This prevents blood getting to the beating muscle of the heart wall, and leads to ischaemic incidents, or myocardial infarctions (so-called "Heart Attacks"). One of the main drives of this work is to study images of coronary arteries to provide image segmentation to support diagnosis in this field.
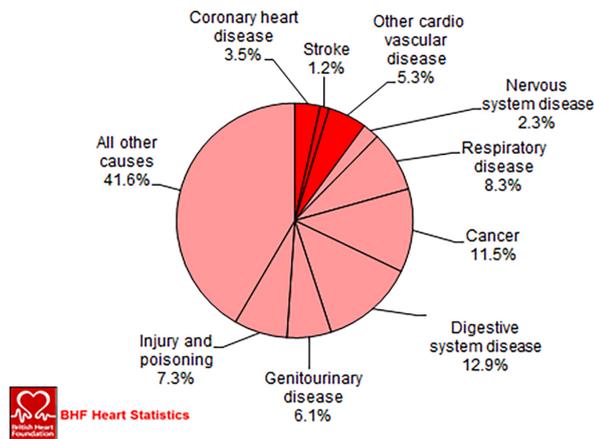
Figure 1.2: Hospital visit statistics for UK in 2012, adapted from [1] study by the British Heart Foundation. As can be seen, a significant proportion of hospital visits are concerned with complications arising from cardiovascular problems. This provides a considerable amount on stress on hospital resources and time.

Our aim is to provide a method to help investigate medical images that is very robust, and draws upon the expert knowledge of the user, whilst allowing a degree of freedom. The main objective of this work looks at creating a robust, segmentation tool that can be used to combine the ease of a automatic, computer driven, segmentation, with that of a manual, user driven method. This is achieved by allowing for minimal user input (which does not need to be precise) to create an accurate segmentation. Although we concentrated primarily on arterial structures, our method was designed to be very versatile, able to fulfil the needs not only in our chosen medical applications, but also able to be used for other modalities, both medical and real world.

The second part of this work looks at Lymph vessels. The valve regions of these vessels are seldom investigated, with the major research drive being lymph nodes, but are a great cause of morbidity in cardiovascular disease, cancer, and other diseases [57, 58, 59, 60]. By using segmentation methods to reconstruct the region around the lymph valve, the underlying structure of the vessel can be studied. From this, it may be possible to understand the mechanisms of failure that lead to the lymphoedema and have a base to investigate mechanisms to alleviate this. The human lymphatic system plays several crucial roles in maintaining health, and the understanding of its function is of great importance in health care. Amongst its roles are the

maintenance of fluid and protein balance, transport of immunological cells, and nutrient up-take. These important tasks are fulfilled by transporting fluid, cells and solutes to and from the blood and the interstitial spaces. This is achieved via the lymphatic compartment, consisting of a series of vessels and nodes throughout the body. Unlike the arteries studied in the other sections of this work, lymph vessels are thin walled and the flow is maintained by the use of valves, as they are low pressure systems. It is the region of the vessels near to these valves that guides our work. In order to understand the malfunction states of the lymph system, under-standing of the mechanics of the normal system is required. We will investigate mechanisms to segment and reconstruct the lymph valve regions of these vessels in 3D.

1.3 Methodology

The aim of this work is to utilize image segmentation techniques to investigate and analyst medical images from a several of differing modalities, including Magnetic Resonance Imag-ing (MRI), Computed tomography (CT), and X-ray, but with most emphasis on IVUS, OCT, and confocal microscopy. Throughout the course of this work we investigate the segmenta-tion of images obtained via common imaging techniques and use provide a novel segmentation technique in 2D and then 3D segmentations. The aim is to provide a reliable, robust image segmentation technique that can be used in a variety of different applications. We present the work showing results for a selection of medical images (from differing capture modalities) and from generic real world imaging, yet the main drive of the work is to produce an application specific solution to be used with catheter based techniques, such as intravascular ultrasound (IVUS) and optical coherence tomography (OCT). We present a method of semi automatic segmentation with minimal user input, combining both edge based and region based values to show improved segmentation results when used to segment both open and closed results. We will compare the results of this both qualitatively and quantitatively with other segmentation methods in IVUS and OCT. We then expand upon this, with the inclusion of automatic tech-niques for 3D segmentation of a whole vessel, and a user guided segmentation of the lymph valve in 3D.

For our work we use three medical image data-sets: one from each of the 3 main modalities we study (IVUS, OCT, and Confocal). These data-sets are manually labeled with ground truths so we can use them to quantify our results. We also use the Berkely Image Database [61] to qualitatively assess our method on real world images.

1.3.1   Image Segmentation

Image segmentation is ubiquitous in many fields today, and involves many varied methods [62], which can be roughly divided into two camps; interactive and automatic methods. Both of these have distinct advantages and drawbacks associated with them. Interactive methods, require the user to provide input to help guide the segmentation. Interactive methodologies require the user to provide selections to define the target region in some way. This can be, for example to select a region to define as background or foreground [63, 64], providing guide points on the edge of the surface [65], or even drawing a boundary box around the desired object [66] In some cases, interactive methods prove problematic, for example if the image is noisy, or the target region is difficult to visualize. There are often solutions to these problems, such as those discussed in Cui *et al* [67]. Interactive segmentation can also be improved by using various optimization methods to assist the segmentation. These methods often involve training the segmentation algorithm with images and known object shapes [63], or using a shape prior to inform the segmentation [39]. One of the main advantages of interactive segmentation is that it allows the expert knowledge of the user to be used to inform the segmentation process. This is especially true in the medical field, as clinicians develop a vast experience of the images they view. This advantage is also one of the drawbacks, as interactive techniques require user input, which puts an extra time demand on the user. It is important therefore, to allow the user to inform the process, but to minimize the amount of input required, which in itself can produce problems requiring additional support to obtain accurate segmentation [68].

Although the fundamental methodologies used in interactive segmentation all require the user to select regions, seed-points or guide-points on edges, how the system uses this information varies greatly. As already mentioned, there are many different approaches for solving the segmentation, which can be divided into broad categories, which we will now look at. These are, learning based approaches, and energy minimization based approaches (such as graph-cut or deformable model based approaches). In learning based approaches, the system reacts dynamically to the user input, refining its segmentation results for the user. It is common-place in these methods for the user to select region based data (usually in one image of a series) and the system will perform the segmentation of the set of images. In early work using this method, Elliott *et al* [69] compared the results obtained after user input with those obtained using default parameters. This was then used to inform the segmentation for the rest of the images. More recent work, such as that by Saffari *et al* [70], uses random forests to predict the labeling

(background or foreground) using a series of pixel based feature descriptors. The principal goal of the learning based approach is to adapt to the user selected features and improve and inform the segmentation (usually of a set, or series of images) based on minimal input from the user. Likewise, there are many different methods used in the energy minimization group, however they all share one feature in common. They all strive to partition the image into different regions by using a process of energy minimization. One of the most commonly used categories of energy minimization methods is graph cut [71, 72]. Graph cut methods often utilize an energy function based on cost terms derived from region based data, edge based data, or a combination of both [21]. It is essential when using graph cuts to define the cost terms adequately to avoid producing a series of local minima instead of the desired global. Another common energy minimization paradigm is that of deformable model segmentation [73]. This is based on variational frameworks, and deformable modeling segments images by minimizing the energy function that is defined on a continuous contour or surface [74]. These methods represent contours in the image in parametric form, having the ability therefore to track the points on these surface curves with time. This makes them suitable for real-time solutions, however they sometimes have difficulties with certain topological changes in the image, which sometimes can pose a problem in medical image segmentation.

Automatic segmentation takes the emphasis away from the user, freeing up their time considerably, but is a difficult process for medical imaging. Automatic methods can use various methods to inform their segmentation [75], such as shape prior [45], or other application specific methods [76]. The main goals of automatic segmentation are to automate a process that is too large (due to the number of cases in a study, or the number of images in a sequence for example) for the user to interactively segment all the data. This can be a difficult task as medical images are often very complex, and have large numbers of anomalies and problems with the images, such as artifacts, occlusions, partial images, and noise. As for interactive methods, automatic methods can be divided into different categories. These are often based on texture features, or grey level features (including histogram features, edge based techniques and region based techniques).

Grey level based techniques are quite common place, and can be quite simple, such as is the case with histogram feature based techniques. Histogram based techniques work by assigning a threshold to values based on their grey level and is the most simple technique [77]. These techniques work well when the image has an area of uniform brightness distinct from the

background (ideally a bright image against a dark background). This simple method works well for certain images, but is very reliant on the quality of the image, and the level that the threshold is set for, which may be difficult in more complicated images, though there are modifications to deal with more complicated images [37]. One of the more common type of grey level segmentation is edge based detection. These use one of the many edge detector functions, such as Canny or Sobel, to find edge information for the image. However, after applying the edge detectors, the algorithm still needs to separate the desired edges from others that could have been detected. There are several approaches that can be taken to obtain a suitable result, including edge relaxation [78, 79], and border detection [80, 81, 82]. Once again the performance can be detrimentally affected by poor quality noisy images, and it is often common-place to carry out a pre-processing stage prior to segmentation, for example using a log Gabor filter [83] or other methods such as anisotropic filtering [84]. The third category of grey level based techniques is region based features. These look for homogeneity in the image, and can be further divided into three principles of region growing [85], namely; region merging [86], region splitting [87], and split and merge [88]. Once again some pre-processing may be required, and this technique can sometimes have a tendency to over or under segment and image.

Texture based approaches use features such as granularity, or smoothness in an image regions to perform a segmentation. The aim is to divide the regions of an image up based on texture properties. A texture may be fine, coarse, smooth or grained, and is dependent on its tone (intensity of the pixels or voxels) and structure (the spatial relationship between the pixels or voxels) [89]. The texture base approach can be further subdivided into three categories, these being statistical [90], syntactic(structural) [91, 92], or spectral [93]. Each approach requires the textures of the image to be defined, in the statistical method, they are defined as a set of extracted features, which are represented by a vector in feature space. For the structural method, they create a link between structural pattern and language syntax, and in spatial methods, spatial frequencies are used to define the texture. Spectral feature based approaches are often combined with other approaches although statistical methods are the most widely used.

There are also methods, such as that described by Zhang *et al* [94], that provide a method that utilises both automatic and interactive methodologies; and recently there has been a shift towards semi-interactive methods [95].

1.3.2 Bottom-up Approach to Segmentation

Bottom-up segmentation is a data-driven method that segments the image based on extracting some low-level features, such as pixel intensity, texture information, color, or edge-based features; rather than top-down approaches that rely on more abstract decision making processes [96]. There are several existing bottom-up segmentation methods currently in use for segmenting IVUS and OCT images which include [97, 98, 99]. The first section of work in this thesis is concerned with developing low-level bottom-up segmentation methods which can not only be used for IVUS and OCT, but are versatile enough to be used in other methodologies, utilizing open (the desired segmentation is similar to a line rather than a closed shape, such as segmentation of cartilage in knee joint, or the horizon in a landscape image, and closed curve, segmentation of a distinct closed shape, segmentations. A combination of complementary features are used, instead of image intensity, to form the the cost functions, including edge based features, obtained with the edge detector; and region based values, especially the discontinuity between similar regions. A pre-processing scheme is also used to refine image features and improve segmentation by the removal of noise in the image. A 3D shortest path segmentation is then carried out to obtain the boundary in the desired region. A comparative study with quantitative experimental results on IVUS and OCT images is presented.

1.3.3 Top-down Approach to Segmentation

Whereas the bottom-up approach was data-driven, basing the segmentation on low level features such as color, luminance, and texture; top-down approaches use higher level features, such as shape, or other class-specific information [2]. The difference in approach provides different styles of results, as shown in Fig. 1.3. Higher level approaches often require training with a sample set of the desired object, shape, or similar feature, and often it is the case that they will not work as efficiently outside the category they are designed for. Both approaches can also be combined, as in Borenstein and Ullman [100] where they combine the approaches in a serial manner to perform the segmentation, using the low-level structure from the bottom-up approach to create a bank of class specific segments that is used in a top-down manner.

1.3.4 Proposed Methods

The coronary artery segmentation developed in this wore used an interactive technique using a combination of region based and edge based features. The segmentation is then be solved
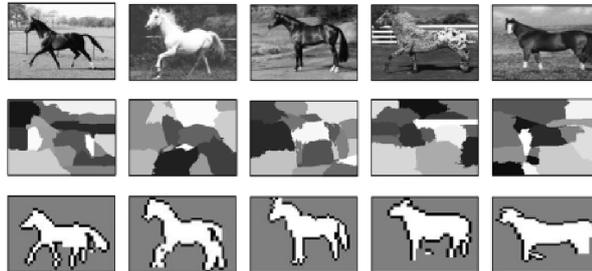
Figure 1.3: Comparison of top-down and bottom-up segmentation of natural images from [2]. The top row represents the input image, the middle row low-level, bottom-up segmentation of the image into regions. The bottom layer shows the results from a high-level, top-down approach. The method depicted used a bank of shape sections specific to a given class (horses) in order to segment the image subject from background.

using a modified graph cut algorithm to segment the desired image. This method allows for segmentation of open or closed objects in the image, making it very versatile as it can be used for multiple applications. In the case of the coronary vessel images used predominantly in this study we segment closed boundaries, namely the media-adventitia and the lumenal boundaries, though we do provide examples of open object segmentation. We minimize the work required by the user, by ensuring that a small number of control points are needed in order to obtain accurate segmentation, and these do not have to be precisely aligned to the edge features, thus reducing the length of time required for user input. We achieve this by adapting our graph construction method and creating a 3D graph to segment. This uses the control points as a non rigid, soft constraint to draw the segmentation towards it, but not force the segmentation to include it. In order to allow the user to segment both open and closed boundaries whilst including regional data, we build up a map of the probabilities of any given point belonging to the foreground or background. This probability map is then used to find the gradient magnitudes of changes in probability, which allows us to formulate the cost in such a way as it can be combined with the edge based term. This provides an accurate, robust segmentation that can be used in a variety of circumstances.

For the segmentation of lymph vessels we utilize an automatic segmentation method. This is both desirable, as in this case we are segmenting a large series of images, which would take more time to label by the user; and appropriate, as with the exception of image quality issues, there are no occlusions, such as stents or calcification present to require specific user attention.

We use an optimal surface segmentation on a scaled down image to perform the initial segmentation that is used as a seed for an Hidden Markov Model (HMM) based segmentation of the vessel walls using the Viterbi algorithm. We also look into a method to modify this to simultaneously segment both boundaries, using an s-excess graph minimization, described later, rather than the standard HMM using the Viterbi we used for the single boundary. This provided comparable results, but improved the extreme cases, making it more qualitatively suitable for vessel reconstruction. For the last part of this work, we will endeavor to reconstruct a 3D representation of a lymph vessel from confocal microscopy images. 3D vessel reconstruction can be done using a variety of methods, such as those shown in [101, 102, 103]. The common diagnostic tools used in cardiology are Angiography and IVUS. The aforementioned IVUS and OCT give a very useful cross-sectional view of the artery, with differing resolutions and penetrance. However, they do not take into consideration any of the vessels topography, as all the images are taken from a centrally situated catheter. Angiography, gives a great 2D view of the arterial system targeted, and is of vital importance in detecting and location occlusions, but gives no structural view. Combination of the two techniques could add topographical information to the structure recorded from catheter based approaches.

In this work, we will look at using sequentially produced 2D images (in this case confocal images of lymph vessels) to expand 2D image segmentation paradigms to create a robust method to reconstruct vessel structure in 3D. We chose lymph structure as although the image quality is poor (due to the imaging modality used) it provides a clear inner and outer boundary for testing the segmentation methodology.

1.4   Contribution

In this work, we present a novel method for semi-interactive segmentation of medical images. This is a robust method, with a small amount user input to guide the segmentation. This method is combined with a boundary tracking method in 3D, allowing the segmentation and reconstruction of vessels and the 3D user assisted segmentation of lymph valve structures.

The main contributions are summarized below:

1. Combined user input. We utilize a novel method based on both region and edge data to provide a robust segmentation a small number of imprecise user points. This method can

be used to segment a variety of images, which can be either open or closed curves.

2. Graph pruning with super-pixel segmentation. In order to improve the efficiency of the above method, we pre-segment the image to prune the graph. This is combined with region information to increase the execution time of the algorithm. A mean shift algorithm is used to create the superpixel cells. These are then run through a low threshold canny edge detector, to provide a binary mask of edges. The user input regional data is utilized to further prune the graph, as edges constrained in a non desired region are grouped together.

3. Automatic segmentation to reconstruct lymphatic vessel valve regions. We provide a method to utilize optimal surface segmentation (OSS) and hidden Markov models (HMM) to automatically detect both vessel walls in lymph vessels, in order to reconstruct the vessel in 3D. We use a coarse OSS segmentation as the seed input for our HMM segmentation, which uses a series of Radial Basis Function (RBF) centers to shift the seed segmentation. This segmentation is performed in polar coordinate images, with samples taken evenly along the segmentation line. In order to improve the quality of the lymph vessel images prior to this segmentation, we pre-process them using a Vessel Enhancing Diffusion (VED) filter to improve the image quality, then process to improve contrast and to create a cross-sectional shape.

4. Using s-Excess graph to simultaneously segment both borders. Using a modification of classical HMM methodology, we simultaneously segment both borders using an s-excess graph minimization algorithm. This includes weights for inter-border arcs, so control over the thickness of the wall can be maintained. This provides a solution to some of the error cases in HMM segmentation alone (as there are many images which have broken, and incomplete borders), whilst maintaining the same overall accuracy levels.

5. Semi-automatic segmentation of lymph valve border. Expanding on our 2D semi-interactive segmentation we segment the boundary of the lymph vessel in 3D. By constructing the graph in a similar manner to earlier, we can segment the boundary of the lymph vessel in 3D. However, as this is working with a much larger graph, we need to minimis the amount of nodes that are worked on. We do this by pruning nodes too far from a cube created with minimum and maximum user values. Also, we utilize one of the features of Dijkstra's algorithm, and only create nodes for layers as they are needed in order to

diminish the memory overhead of the graph. Using the border we segmented, we can then use a minimal surface segmentation to find the border in 3D. This is then smoothed using a series of RBFs in order to provide the final result.

1.5 Thesis Outline

The rest of the thesis will be organised as follows:

Chapter 2 -Background and Literature Review: Providing an overview of medical imaging techniques, with emphasis on catheter approaches, such as IVUS and OCT. An overview on segmentation techniques is presented along wit a discussion of their usage in both medical and the general field.

Chapter 3 -Semi-Interactive segmentation of vessel borders. This chapter, presents a novel technique for segmenting borders in arterial images, namely the media-adventitia (IVUS) and lumenal (OCT) borders. The novel graph construction and energy minimization problems are discussed and results are presented to compare the findings with other methods in both afore-mentioned medical applications and a series of other images to demonstrate the versatility of the method.

Chapter 4 -3D reconstruction of vessel walls. Looking at lymph vessels as a target application, segmentation (both individually and simultaneous) of the vessel walls is carried out the resultant inner and outer boundaries to reconstruct a 3D model of the vessel

Chapter 5 -Lymph Valve reconstruction. Expanding our 2D segmentation method discussed in chapter 3, we use an adapted version to aid in segmentation of the valve structures of lymph vessels in 3D.

Chapter 6 -Conclusions and future work. This concludes the thesis with a discussion of the methods used, and possibly ideas for their later expansion.

Chapter 2

Background

Contents

2.1 Introduction

Over the course of this chapter, we will look at the anatomical structures of the Cardiovascular and Lymphatic systems. These two systems are vital to the health of the individual, and form the main subject for the research presented. After an overview on the systems is given, the chapter will move on to discuss medical imaging techniques, such as those used to obtain the raw data for this work. Once the medical background is covered, the methodologies for segmentation and processing of the images will be addressed. An overview of different methods and approaches, covering many aspects of the field will be given. It is important to understand the various options available, and the advantages and limitations of each approach to image segmentation.

superior vena cava

right pulmonary arteries

right atrium
right coronary artery

right pulmonary veins

conus arteriosus branch

right anterior ventricular artery

right marginal artery

right ventricle

inferior vena cava

aorta
pulmonary artery
left pulmonary arteries

left atrium

left pulmonary veins

cirumflex artery
left marginal artery

left anterior descending artery
left ventricle
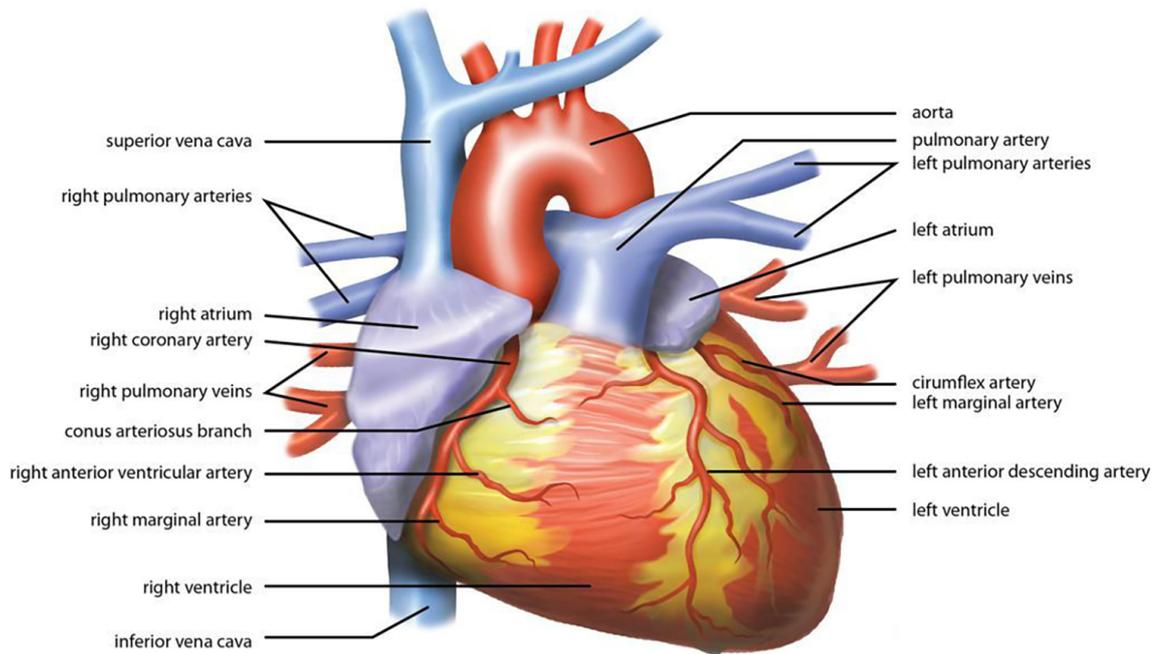
Figure 2.1: External anatomy of the heart, adapted from [3]. Showing the coronary arteries.

2.2 Cardiovascular Anatomy

In its simplest form, the cardiovascular system can be thought of as a pump (the heart) and a system of pipes (the blood vessels). Although this analogy is true in the most basic and literal sense, the reality is far more complex and interesting. The heart is a specialized muscle that pumps blood around the body continuously for the whole of your life without any rest periods. In order for it to accomplish this task, it must have a continuous supply of oxygen and nutrients. This is achieved through a system of blood vessels ringing the heart called the coronary arteries. These arteries branch off the ascending aorta (the largest artery) as the left and right coronary arteries before further subdividing as shown in Fig. 2.1. The branches of the right coronary artery provide blood supply to the right atrium and ventricles (as well as a small area of the left atrium and ventricle) and the atrioventricular septum; the branches of the left coronary artery supply the rest of the left atrium and ventricle as well as the ventricular septum. Occlusion of any of these vessels can interrupt the blood supply to the heart, leading to ischaemia and damage.

Arteries, including coronary arteries, consist of three distinct regions. These are the lumen,
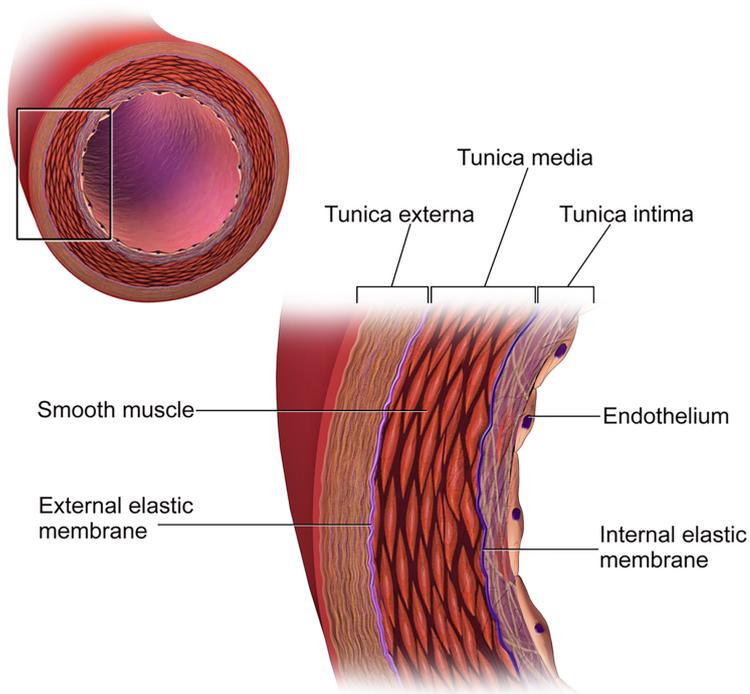
Figure 2.2: Anatomy of an Artery, adapted from [4]. The artery wall comprises of layers as shown, namely the tunica intima (nearest the lumen of the vessel), tunica media, and tunica externa (also known as tunica adventitia) as the outermost layer.

in the center where blood flows,the vessel wall proper (made up of tunica intima and tunica media layers), and the tunica adventitia (or tunica externa), a layer of connective tissue around the vessel providing support. The diameter of the vessel varies with type, the aorta being the thickest. The thicker vessels have more smooth muscle present in their wall to maintain pressure on the blood. The tunica intima is the most inner layer of the vessel, made up of elastic tissue and is lined with endothelial cells, which prevent clotting and take an active part in controlling blood flow through the release of Nitric Oxide(NO). The internal elastic lamina separates the tunica intima from the tunica media, which contains smooth muscle and elastic fibres. There is a thin layer, the external elastic lamina, separating the tunica media from the adventitia, which forms the outermost layer see Fig. 2.2.

2.3 Cardiovascular Disease (CVD)

A major underlying cause of CVD is coronary artery disease. Coronary artery disease, also
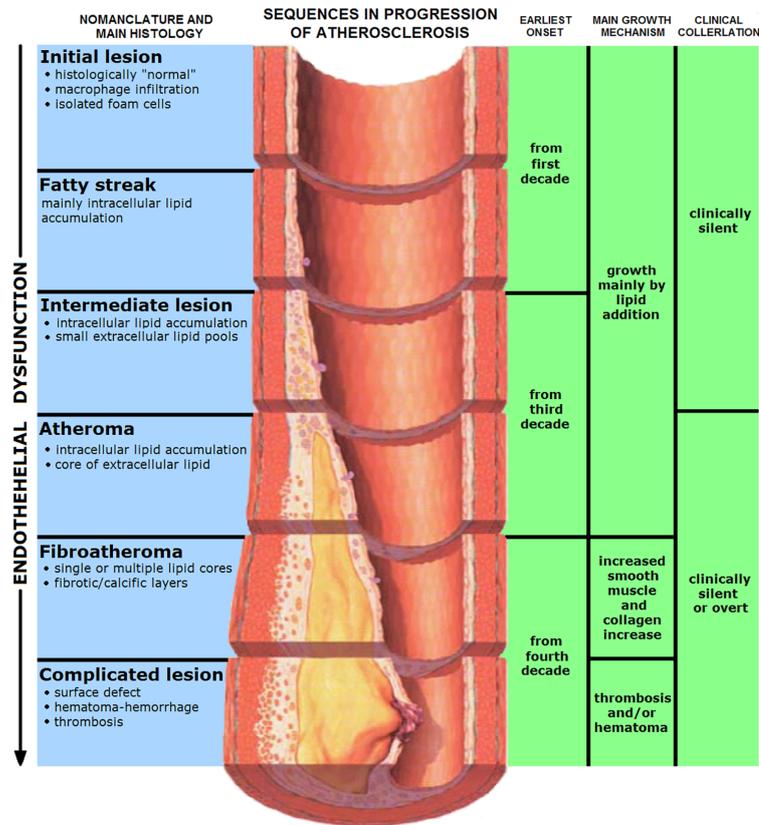
Figure 2.3: Progression of atherosclerosis, from [5]. Showing the stages of lesion development, including time-frame and whether the symptoms can be detected.

known as atherosclerosis, is a disease state that leads to thickening and eventually occlusion of artery walls. Due to the narrow nature of the coronary arteries, they are especially vulnerable to this. Atherosclerosis is an inflammatory disorder involving the deposition of fatty substances, such as cholesterol, on the vessel wall. This produces a gradually worsening occlusion of the artery and can lead to a variety of complications. For example, if the blockage becomes free to move it could lead to clinical angina (as the blocking effect is transitory). The fatty deposit can also break off, or rupture. Both of these are very serious, as they can cause full occlusion of vessels leading to acute myocardial infarction (a "Heart Attack"), either due to the fatty material itself blocking the artery, or the damage of the rupture provoking the clotting mechanism and leading to a blood clot (or thrombus) to be formed, see Fig. 2.3.

2.4 Lymphatic System

The lymphatic system is vital for maintaining healthy functionality in the body; fulfilling this task by the transport of fluids and immunological cells from and to the blood and interstitial spaces (see Fig.2.4. The lymphatic system at its most basic is a system of pipes and valves to ensure unidirectional flow, but unlike the cardiovascular system it is not closed system. Lymph drains into and out of the organ beds, perfusing the interstitial space and is involved with homeostasis and the functions of several body systems [104].

The vessels are thin walled and not under pressure, so without the valves it would be impossible to maintain unidirectional flow. The system works in conjunction with the cardiovascular system in transporting lymph (made up in the most part from interstitial fluid collected from the organs), before draining into the cardiovascular system in the subclavian veins. Lymph vessels are made up of a very thin layer of smooth muscle, lined with endothelial cells and are surrounded by an adventitia, which secures it to the tissues it passes through. In general, the valves ensure that lymph flows away from the tissues to lymph nodes and eventually lymph ducts, then veins. The smallest lymph vessels, lymphatic capillaries, lack the smooth muscle and can even lack the adventitia. Certain disease states can lead to a compromise in flow, causing lymphedema, decreasing overall health. This leads to painful swelling of limbs and other complications, and currently, health care is concerned with treating the symptoms, rather than identifying the underlying cause and preventing the situation. By reconstructing the vessels from the confocal images, we hope to produce a system which we can expand upon, to examine valve function in lymph vessels, and identify any areas where flow may be compromised. The lymph system, draining from the tissues as it does, is also of key importance in the metastatic spread of cancer cells, so understanding the flow through the system will help understand this spread.

2.5 Medical Imaging

The modalities used in medical imaging can be grouped into two very broad categories, namely invasive and non-invasive procedures. Invasive procedures requires a sensor, or recording device to be inserted into the target area. In cardiology, this is often achieved by the use of catheter based approaches. In these catheterization techniques a thin guide wire if fed up into the target artery (for example a coronary artery), and used to insert a catheter tube. Examples of
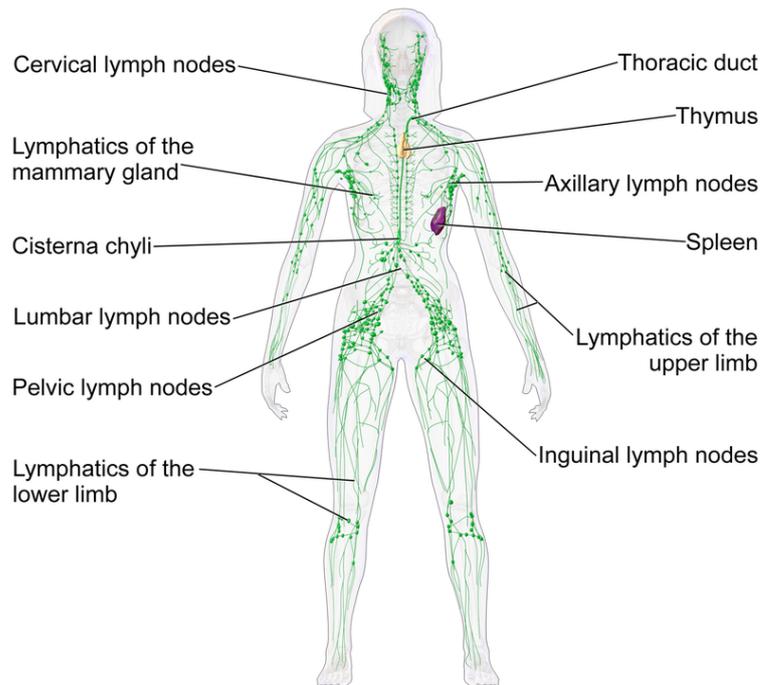
Figure 2.4: Representation of the Lymphatic System [6]

this technique include X-Ray Angiography, Intravascular Ultrasound (IVUS) and Optical Coherence Tomography (OCT). X-ray angiography is very widespread, and is used to show the branching structure of vessels (by directly injecting contrast, that is picked up by the recording unit) and can be used to detect the location of an occlusion or stenosis. Although it is a gold standard for mapping the arteries and detecting areas of occlusion and narrowing, it does not give very accurate information of any pathologies present. In order to detect and classify pathologies such as plaque erosion and rupture as well as clot formation and others, IVUS and OCT are used. Both these images can be used for diagnosis, and produce a two-dimensional cross section of the artery, with the probe (inserted along the catheter) at the center. By pulling the probe back along the catheter (A so-called "pull-back") a sequence of images can be obtained through the region of the occlusion (usually identified by X-ray angiography).

2.5.1   X-ray Angiography

X-ray angiography is one of several commonplace catheterization techniques in place today. It provides a diagnostic procedure for identification of occlusions in the vessel. This is done,
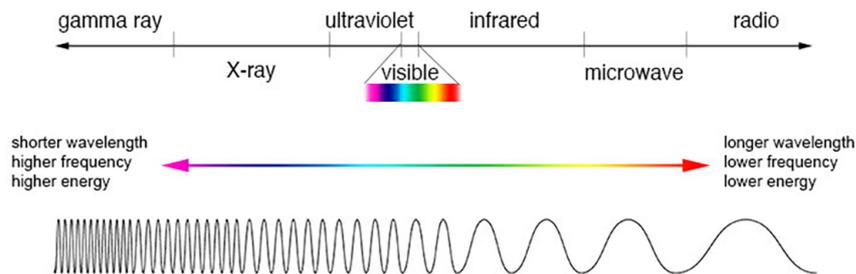
Figure 2.5: The Electromagnetic (EM) spectrum. [7]

however, without providing any information about the type of occlusion or wall thickness.

X-rays are an electromagnetic wave, with a much higher energy and shorter wavelength than visible light (see Fig. 2.5).

X-rays are produced in a vacuum tube with a hot cathode, and an anode made of a high atomic material (such as tungsten). A large potential difference accelerates electrons from the cathode to the anode, where they hit the rotating tungsten disk to provide a focussed beam of x-rays. These can be detected using a detector based on photographic plates (or in more modern machines today, a digital detector).

The functionality of x-ray imaging comes from the attenuation of the x-ray itself. X-rays have a differing penetrance based on the material they pass through. For example, bones cause a higher degree of attenuation than soft tissue (leading to the classical use of x-rays to investigate bones and fractures). Certain disease conditions can effect the attenuation characteristics of a medium too, a factor that leads to x-rays being of great use in identification of cancer. However, from a cardiology standpoint, it causes a problem as blood and the surrounding soft tissue have the same levels of attenuation. This problem is solved by the use of a contrast medium (e.g. an iodinated contrast material) that is injected via catheter inserted via the femoral artery. Modern methods utilize a technique called Digital Subtraction Angiography, where an image is taken before and after the addition of the contrast material, so as to digitally remove the surrounding tissues, leaving only the vessels desired. Angiography images provide a topographical "map" of the arteries, but present very limited structural information Fig. 2.6. Although the diameter of the vessels, their shape, and any occlusions can be seen, structural information such as wall thickness, and the type and quality of any stenoses or lesions cannot be ascertained.

Figure 2.6: An example angiography image [8]. The layout of the arteries of the left coronary circulation, and their relative thicknesses can be clearly seen. The arteries visible include the distal left main coronary artery (LMCA) (left upper quadrant) and its main branches (the left circumflex artery (LCX), and the left anterior descending (LAD) artery)

2.5.2 Catheter based Imaging techniques: Intravascular Ultrasound (IVUS) and Optical Coherence Tomography (OCT)

IVUS is a catheter based invasive diagnostic method, widely used in hospitals, using an ultrasound probe to produce cross sections of the artery wall. Catheter based approaches, such as this, provide the clinician with a valuable tool, which can be used to assess the severity of any stenoses present, to categorize their morphology. Catheter based approaches use a probe that is inserted into the coronary arteries on a guide wire. This is then pulled back along the wire (hence the term "pull back" refereing to one series of images) whilst images are recorded. The tool can be further used by clinicians to measure the vessel diameter (allowing the severity of any occlusions to be assessed), and the location of any lesions to be identified, as well as many other clinical and therapeutic studies [105],and can be used for post operative assessment of stent location [106]. IVUS images can be taken in 'A' mode or 'B' mode. 'A' mode displays echo amplitude on the *y-axis* and time on the *x-axis*, and 'B' mode uses "dots" of different intensities to represent the intensity of the echo received. to In most IVUS B-mode images, a cross-section of the arterial wall is produced, with three distinct regions: the lumen, the vessel (made up of the intima and media layers), and the adventitia surrounding the vessel wall (see Fig. 2.7). It is very difficult to differentiate between the tunica media and tunica intima with IVUS images. The media-adventitia border, which is the target for our segmentation in IVUS images, is the dividing layer representing the outer arterial wall. In IVUS images, the

media can be seen as a dark band, with no other distinct features. It is encapsulated by the adventitia, which is a wide layer of fibrous connective tissue. IVUS segmentation as a cost function minimization problem has been a popular approach to solve this problem. As can be seen in Fig. 2.7, IVUS images have many artifacts, mainly due to the mechanism of obtaining the image or the nature of ultrasound. The most commonly found artifacts include: guide-wire (the wire used in the procedure interfering with the image), catheter ring-down artifacts (a halo surrounding the catheter), stents (inserted by a previous medial intervention, can cause bright regions and shadows on images) and calcification (a large brighter area, with shadow underlying, showing a pathology present) shadowing. Any or all these artifacts may be present in a particular pull back, and all create problems and complexities in the segmentation process, as they often produce dark occluded regions with no detail or features present. It is in dealing with these occluded regions, that the inclusion of user input becomes very important.

OCT, like IVUS, is a catheter based technique used in cardiology, however it utilises optical rather than ultrasound technologies. OCT is a newer approach, debuting in 1991 [107], which uses light from the near-infrared region of the electromagnetic spectrum (Fig. 2.5), this enables OCT images to have a higher resolution (15-20μm) than those obtained by IVUS (100-200μm), but due to the optical nature of the system, have much less penetration (1-2.5mm compared to 10mm in IVUS), and so are more useful for looking at surface structures in the vessel, see Fig. 2.8. The OCT images, therefore, are segmented to reveal the lumen border, which is far clearer on these than in the IVUS images (Fig. 2.8). This is clearly visible for the most part, but in a similar fashion to IVUS images there are a number of artifacts present which lead to occlusions. These are reflections/shadows caused by the guide wire, reflections/shadows caused by stents, and other anomalies such as shearing (sew up errors), presence of blood in lumen etc, see Fig. 2.9 for some examples. These anomalies lead to a characteristic shadowing, often accompanied by a bright region (such as reflections of stents and the guide wire).

Due to the nature of these artifacts, automatic methods employed in these applications require a significant amount of pre-processing [108], [109]; a large data set for training set [110], or a method to remove the artifacts [111]. Our proposed method, by giving the user control to help the process removes the need for extensive pre-processing or large data sets for training, allowing user guidance to avoid pitfalls used by image quality or artifacts present. The nature of the IVUS and OCT images, with very pronounced artifacts lend themselves well to this semi-automatic approach, with most parts of the image being such that the automatic process
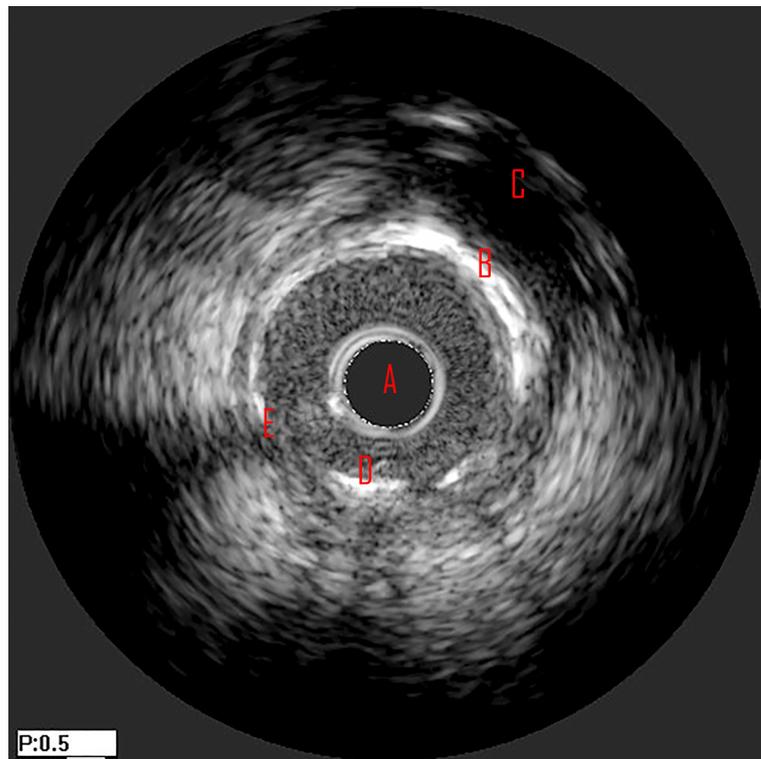
Figure 2.7: Overview of an IVUS image acquired by 40MHz transducer Boston Scientific ultrasound machine, showing a selection of the artifacts found in the images: A = Catheter Region, B = Calcification (a medium to large bright region), C = Shadow region (as result of calcification), D = Stent (a single small, bright region with underlying shadow), E = Guidewire shadow (a long regularly shaped shadow region, often extending into lumen with bright regions along it).

will be suitable, but by allowing user input, the difficult regions (such as shadows and various artifacts) can be accommodated easily. Interactive segmentation that can efficiently and effectively transfer user knowledge to the segmentation is thus highly desirable in this application. It also allows us quantitatively evaluate our method, including both efficiency and accuracy.

2.5.3 Confocal Microscopy

Confocal microscopy is a method that allows for the visualization and imaging of 3D volume objects that are thicker than the focal plane of a conventional microscope using a pinhole, situated in front of the photo-detector. This serves to attenuate any signals originating outside the focal region, allowing for "optical slices" to be obtained through an object [112]. This optical sectioning is much stronger than the depth of focus of the microscope; allowing for the
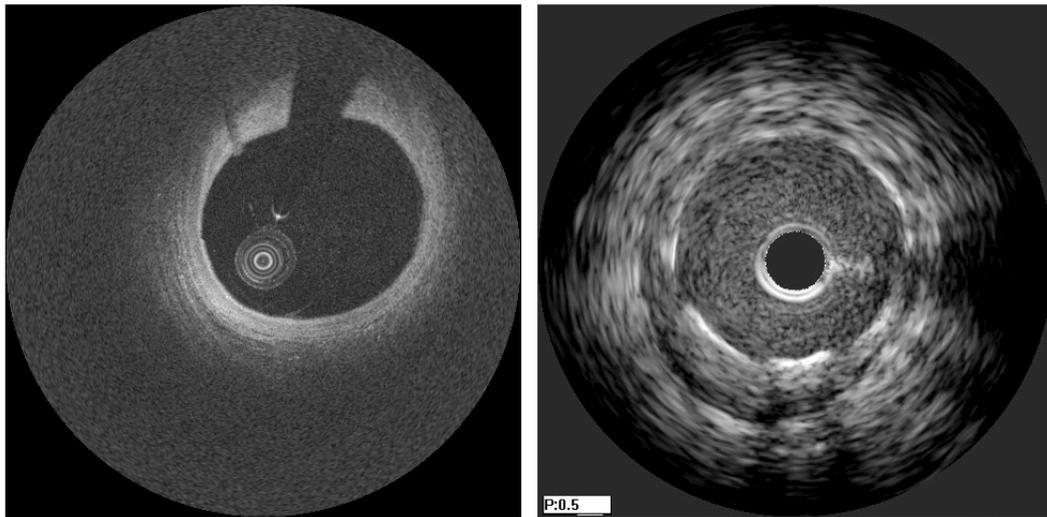
Figure 2.8: Overview of an OCT image (Left), compared to an IVUS image (right). Not the difference in resolution and penetration of the images. Both images have a catheter visible in the lumen (the dark circle on the IVUS image, and the series of bright rings in lumen (OCT). Not the lumen is clearly visible as a dark region in the OCT image, which is not the case with IVUS. Also the lumenal border is much clearer in OVT compared to IVUS, buyt the IVUS image shows more deep detail (such as the media adventitia border (a dark line)).

objects in the layer of interest to be in focus, and making the capturing of the relevant image to the computer a simple procedure. Unlike conventional microscopy only one point of the sample is illuminated at a time in confocal microscopy. During operation, a laser beam scans the object pixel by pixel, line by line and any light outside of the focal plane is blocked by the point detector. This data is then reconstructed by the computer into the 3D image $I(x,y,z)$. It is necessary to build up the image by scanning the microscope over a regular pattern. This pattern (called a raster) is made up of multiple parallel scanning lines. It is essential to do this, as the nature of the confocal microscope means that only one point in the sample is illuminated at any given time, the multiple scans are therefore required to build up the complete image. The thickness of the focal plane is defined by the inverse of the square of the numerical aperture of the objective lens, but can also affected by the optical properties of the specimen and the ambient index of refraction, and is limited by the wavelength of light. A schematic of this technique is shown in Fig. 2.10.
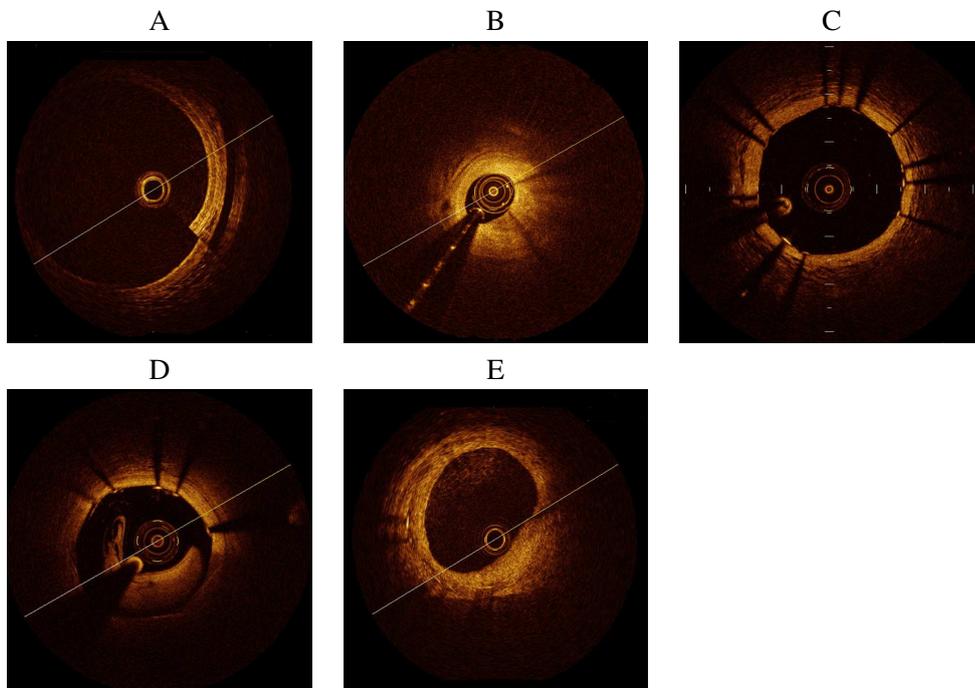
Figure 2.9: Examples of artifacts in OCT images. These are A: Sew-up (shearing, caused by rapid movement of probe or artery causing misalignment)) error, B Guide-wire reflection/shadow, C: stents (surgical interventions to treat occlusions in the artery), D: swirls (bolus of blood in lumen obscuring image) and E: speckles (caused by small amounts of blood in lumen occluding the light source).

2.6 Image Analysis

Image segmentation is of great importance and commonly used in various applications, from agriculture [113], surveillance [114] and medical applications [62]. Image segmentation can be defined as partitioning an image into distinct and meaningful regions, delineating each region boundary based on a set of extracted features. In medical imaging paradigms, such as vessel segmentation, the image segmentation is concerned with segmentation of the tubular like structures from the background for example. There have been several good reviews on the subject, for example, those by [105, 115, 116]

There are two broad categories of techniques: automatic and interactive, each of which can be categorised into different classes, such as; simple region-based approaches (e.g. thresholding, energy minimization approaches (which can include combinatorial optimization and deformable models), and machine learning based approaches. Methods can also be categorised
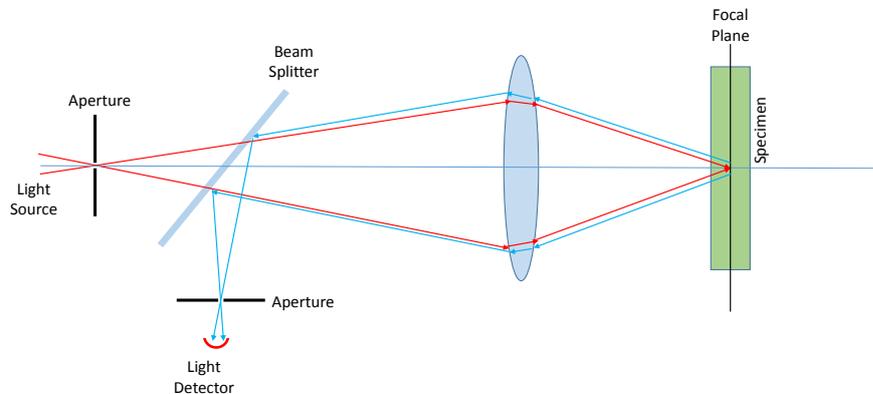
Figure 2.10: Schematic showing the principles of Confocal Microscopy. From [9]. This represents one point on the image, in order to obtain a complete image, movement through scan lines or rasters is required.

into the aforementioned bottom-up (or low level) and top-down (high level) approaches. Most of the methods discussed in this chapter follow a bottom-up approach (to a greater or lesser degree). These approaches all use some distinct features, such as edges, texture, or just plain luminance values in the image data to perform a segmentation. Automated techniques (such as [10] shown in Fig. 2.11 and [117]) are appealing in terms of efficiency, as they do not require extra work from the user. More often than not, however, prior knowledge about object appearance and/or shape is necessary to achieve meaningful results; and in the medical idiom, any training or prior knowledge would have to be such that it was enough to deal with unexpected variations and non-standard data. The situation is further complicated by problems that are inherent to most medical imaging modalities, such as noise and artifacts. It is therefore, not always practical, or even possible, to obtain comprehensive prior information and a sufficiently robust learning algorithm to deal with large and sometimes unpredictable variations that occur in medical images. An alternative approach to automated segmentation is to allow and encourage user input and provide interactive segmentation results to suffice user demand. This has the advantage of being able to use expert user knowledge to avoid problems, and to inform the segmentation. This, however, leads to a dilemma; as the increase in the amount and precision of user input, whilst improving the segmentation is many cases, takes time and is less efficient and optimum for the user. The goal is to balance user involvement and interaction flexibil-
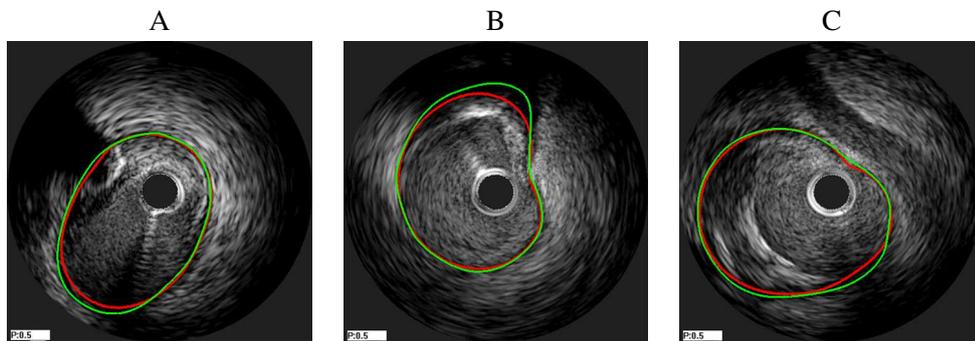
Figure 2.11: An example of automated segmentation of media-adventitia border in IVUS images [10]. Both appearance and shape priors are necessary to constrain the segmentation. The results are shown in red and the manual labeling is shown in green. This gives good results overal, but in regions of shadow or severe occlusion (especially in B) it differs considerably from the ground truth.

ity, particularly given the ubiquitous imaging device and ever increasing amount of images in modern age. To effectively and efficiently capture user intent is vitally important, allowing the expertise of the user to be used, without the system being too labor intensive for the user, or so inflexible that it cannot adapt to extreme cases.

Another aspect that needs to be considered is what method for separating objects will be used. This is of vital importance, as different segmentation procedures have their own strengths and weaknesses; for example, the ability to segment both closed, discrete, regions and open contours may also be important. A large number of automatic segmentation processes will require the object to be segmented to be discrete. This is not necessarily of use, as in some cases these methods will not be able to identify the specific region the user wishes to be selected for, which may not form a closed curve, but may instead be of a more open nature. Hence, methods that are capable of both may have a wider appeal in medical applications than those, for instance, can only partition images into disjoint and self-enclosed regions.

2.6.1 Interactive Segmentation

This broad category is defined as requiring a degree of input from the user in order to guide the segmentation process. The user interaction is conventionally made either by simple mouse click or drag operations on the region of interest, or on the object boundary; mechanisms that are familiar to the user, and without specialist hardware and training. For example, in
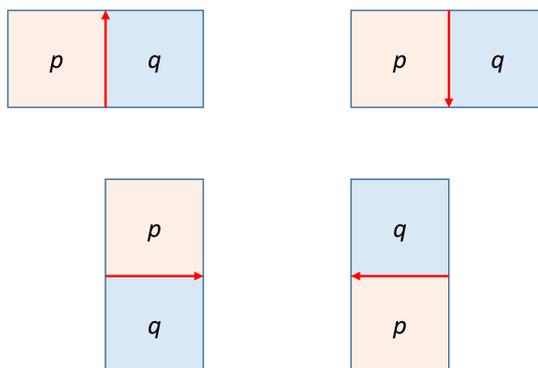
Figure 2.12: The four directional edges between pixels, adapted from [11] showing the different boundary elements that can occur

Intelligent Paint [118],which is a simple interactive method that allows the user to identify all the regions inside an object. The object region is interactively expanded by a simple click and drag operation. Then a homogeneous area that has the same intensity profile is selected, which is very similar to those techniques adopted in commercial software. Similarly, with Magic Wand, e.g. in Adobe Photoshop, a user can highlight all the homogeneous area that has the same intensity profile by simple mouse clicks.

The Intelligent Scissors [20], shown in Fig. 2.16, and Live Wire [11], shown in Fig. 2.17 methods are among early methods to perform on the fly segmentation by allowing the user to follow the object boundary, instead of region, through a few mouse clicks. These methods are based on well-known shortest path algorithms, such as Dijkstra's method, to find the optimal shortest path between two user points. Shortest path methods have an advantage of segmenting both open and closed objects. Livewire segmentation as described in Falcão *et al* [11] treats a feature as a function to be assigned to each boundary element $b = (p, q)$ of any given scene $\mathbf{C} = (C, g)$ and integer to represent a property value. It creates the scene $\mathbf{C}$ as a pair (C, g) finite 2D rectangular array of pixels C and a function g that assigns an intensity value to each pixel p. Boundary elements are further defined as orientated pixel edges, with a given direction see Fig. 2.12.

Boundary features which can be looked at include intensity (both inside and outside the boundary), gradient magnitudes, orientation-sensitive gradient magnitudes, and distance from previous boundary. These boundary features are then allocated cost values using cost functions

Figure 2.13: Demonstration of the limitation of using hard constraints for user input [12]. User points away from boundary force the segmentation to move through them, resulting in errors.

(which they refer to as feature transforms). The shortest path between two points is then found by minimizing the cost of the corresponding boundary elements.

However, often only edge-based features are used to find the shortest path, and more importantly usually those user points are treated as anchor points that the segmented path has to go through. This requires precise input from the user, and without post-processing results in uneven edges as the result is forced to move through the user point, even if it is not on the strongest edge, see Fig. 2.13.

Another method of segmentation that are commonly used are active contour models (or snakes). These methods all provide a framework for segmenting a 2D model using a deformable spline to match the contour. Fitting these splines to the contour is a process controlled by external constraints, forcing its movement towards features such as lines and edges [74]. Kass *et al* represent the position of the "snake" parametrically as:

$$v(s) = (x(s), y(s)), \tag{2.1}$$

where s is a spline in the snake. They formulate an energy function for the segmentation as follows:

$$
\begin{aligned}
E_{snake} &= \int_0^1 E_{snake}(v(s))ds \\
&= \int_0^1 E_{int}(v(s)) + E_{image}(v(s)) + E_{con}(v(s))ds
\end{aligned}
\tag{2.2}
$$

Where E_{int} represents the internal energy of the spline due to bending, E_{image} represents the image forces, and E_{con} represents the external constant forces.

Active contour models provide a good quality segmentation, but many suffer from initialization-tion dependency problems. Typically, this is tackled by adding a prior to the model to give the segmentation a better initial state or an overall constraint, which may not be always practical. There are various solutions proposed to alleviate this problem, such as [119] that uses another automatic segmentation method on a coarse down-sampled image to provide the initialization for their active contour model, and [13] that uses coarse results extracted by spatial fuzzy C-means clustering, see example results in Fig. 2.14. There are however other methods that attempt to achieve global minima, either through global minimization or through deriving external force field that is initialization independent. For example, in [120, 19], the authors show that even using conventional gradient based boundary description it is possible to achieve global minima with gradient descent. Its force field is computed based on global interaction of image gradient vectors and its force is always perpendicular to the evolving contour. Fig. 2.15 provides a comparative example of classical gradient based methods and the MAC model [19].

With the help of powerful optimization techniques, the method of user interaction has been expanded, for example, adding object/background strokes, at the same time simplify user involvement compared to painstakingly tracing the object boundary [21, 25, 121, 24, 122, 11, 12]. For example, the user can simply draw multiple strokes inside and outside the object then the segmentation model can learn the distribution of pixel intensities for both object and background. These techniques usually are more suited for segmenting closed objects, but not for open curve segmentation, but in the proposed method we adapt the method so that it can be used with both open and closed objects.

In terms of optimization technique, graph cut and shortest path search are two of the most common categories of methods of interactive segmentation. Graph cut algorithms are widely used to find optimal solution in interactive segmentation at polynomial time complexity and are most usually used for segmenting closed objects.

Boykov and Jolly [21] (shown in Fig. 2.18) introduced a graph cut based interactive segmentation method by defining unary and pairwise costs of each pixels. The unary cost is inversely proportional with the probability of each pixel to be in the object or in the background while the pairwise cost is based on the intensity difference between two neighboring pixels. The
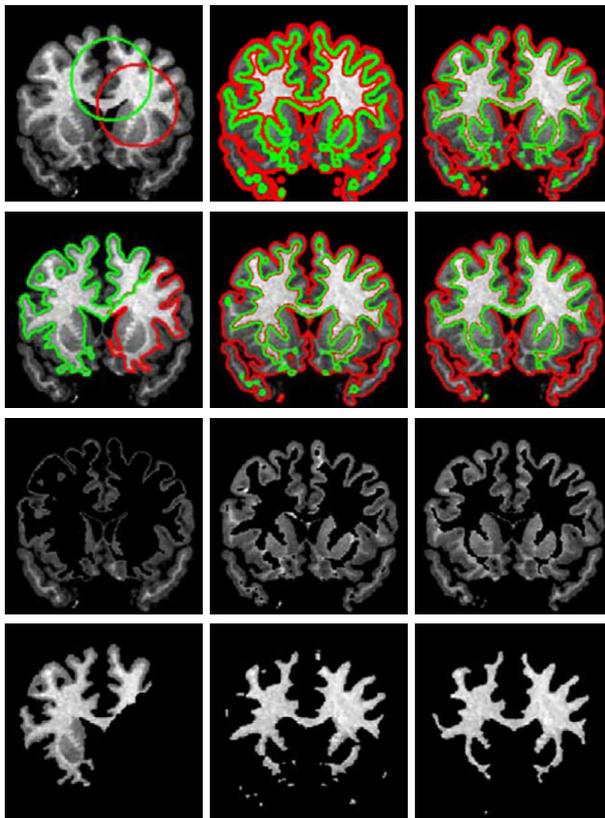
Figure 2.14: Example of MRI segmentation using active contour, showing the effect of three different initialization methods [13]. The top row shows the initial curves. The second row shows the stable curves obtained from the method; The last two rows show the segmented gray and white matter respectively. The first column shows manual initialization, which gives unsatisfactory convergence. The center column uses a threshold method based on coarse segmentation and right hand column uses pre-processing as suggested by [13].

principle of graph cut techniques is to divide any graph $\mathcal{G} = (\mathcal{V}, \mathcal{E})$ into two subsets, one connected to the source (usually labeled *s*), and one connected to the sink (usually labeled *t*). The cut $C = (S, T)$ is a partition of $\mathcal{V}$. The min-cut/max-flow theory states that the maximum value of flow from *s* to *t* is equal to the minimum capacity over all the $s - t$ cuts.

Many methods have been introduced to extend this method, such as to combine shape prior with user initialization [22] (shown in Fig. 2.19), Grab Cut [25] and Lazy Snapping [23], shown in Fig.2.20. In Grab Cut, the authors proposed to use a Gaussian mixture model to build a local color model to build the cost term. It reduces the user intervention by allowing the user to define a rectangular window surrounding the object, and also allows iterative interaction to refined the
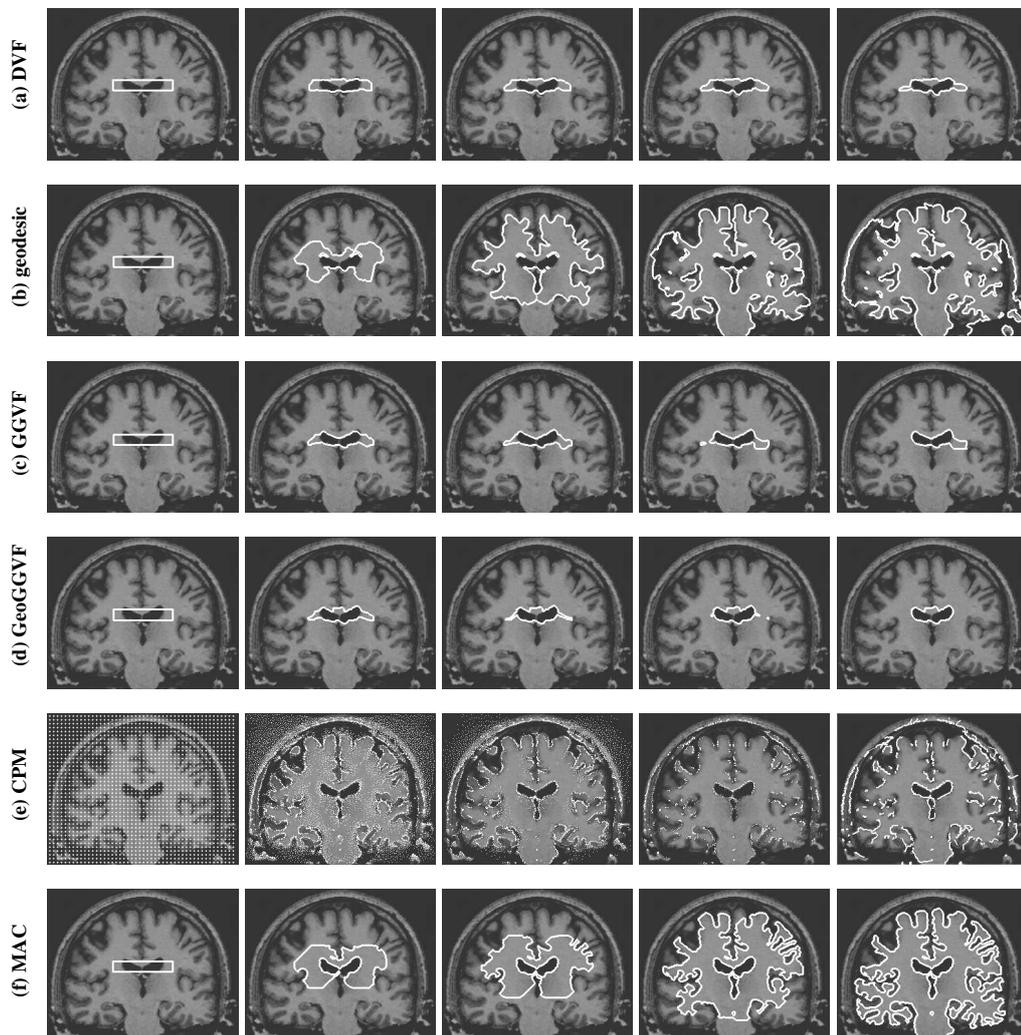
Figure 2.15: An example showing comparison among several gradient based active contour techniques, that are popular in interactive segmentation. User interaction however is simplistic and generally limited to initialization.Results by row: (a) DVF [14], (b) geodesic [15], (c) GGVF [16], (d) GeoGGVF [17], (e) CPM [18], (f) MAC [19].

result. Lazy Snapping is also based on using a graph cut over a pre-segmented image using a watershed algorithm for thresholding. K-means is used to cluster the foreground/background colors and assign each pixel to the nearest cluster. The method usually incorporates a boundary editing tool to refine the result. However, this method usually needs multiple user interventions to correctly cut out the object, due to the simplicity in its cost function, which is often build on simple image features, resulting in over or under segmentation at the super-pixel stage.

Figure 2.16: Selected frames from an example of live-wire segmentation [20]. The red dots show the seed points; the green cross-hair is the free point; the blue contour segments correspond to portions of the set boundary; and the yellow contour segment is the live-wire boundary segment. Top row (left to right) shows selected frames from the interactive segmentation process and the main image shows the result.
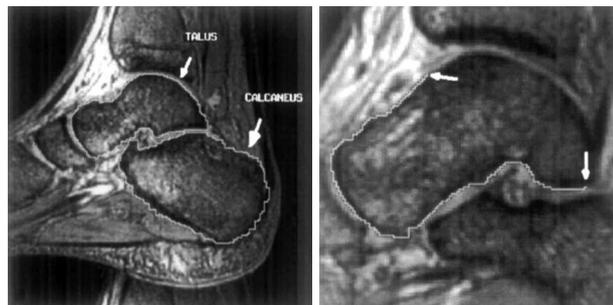
Figure 2.17: Live Lane segmentation example from [11]. The left shows an MRI slice of the foot of a subject showing the bones talus and calcaneus (marked). The Image on the right shows a zoomed-in image of a tracing on the boundary of the talus.
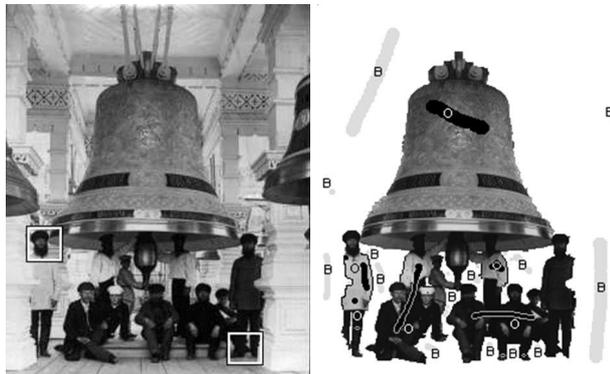
Figure 2.18: An example of graph cut segmentation using s-t cut [21]. The original image is on the left, and the results are shown on the right. The results are marked '"O" for object and "B" for background.
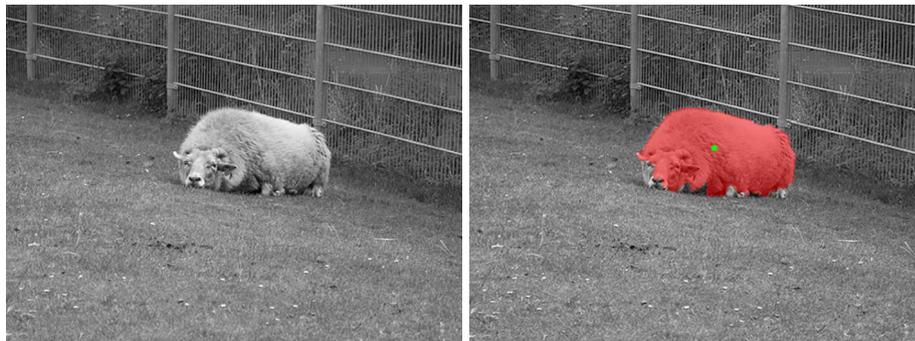
Figure 2.19: Semi-automatic segmentation with minimal user input (green point marking the center of an object) [22]. This is a modification of star based graph cuts using gradient vector based image feature

Shortest path is another optimization technique that has been used in interactive segmentation, e.g. [20, 11, 12]. These methods place the emphasis on boundary based features; edge based features are used to define the cost between pixels, and can be used on both open and closed segmentations. One weakness with these methods is a susceptibility to artifacts, such as noise, and poor quality images with fainter edge features. These can sometimes pose a problem, and methods are often applied to improve the image quality (in pre-processing) to alleviate this [123, 124, 125]. Most shortest path methods require the user interactively identifies a starting point of the path and iteratively adds more seeds around the outline of the object. On the other hand, the intelligent paint method [118] allows the user to identify regions inside the object instead of the boundary. The region is interactively expanded by simple click and
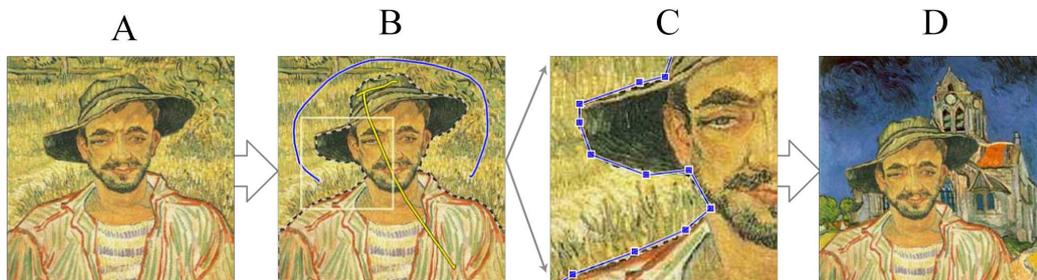
Figure 2.20: Lazy Snapping [23] is an interactive image cutout system, consisting of two stages: firstly, an object marking stage and secondly boundary editing. In (B), the two user selections (yellow to indicate the foreground, blue background) are drawn. The box represents the zoomed section in the (C). In (C) (zoomed) image, the segmentation is shown, with control points. (D) shows the cut out is superimposed onto another Van Gogh painting.

dragging operations. Shortest path has an advantage of segmenting both open and close end objects, however many of them only use edge-based features to find the shortest path and the user points are generally treated as hard constraints, though some methods [12, 126] use soft constraints. The advantage of soft constraints is that the need for accuracy in the user input diminishes. This dramatically reduces the effort required in the user input stage, making the method more useful in situations where the user's time is valuable.

Incorporating shape prior (a weighting based on a pre-constructed, generalized, shape) into graph based segmentation has also shown improving the segmentation result, e.g. [127, 128, 129, 24, 10]. Veksler [24] introduced a star shape prior to graph cut, also through user interaction. The star graph cut uses a prior that is generic, not based on a high-level object class (for example "person", or "horse"), but rather it exhibits the geometric properties of the object. A *star* object is defined by the user specifying the center of region of interest (ROI) as the star point, and hence all boundary points of ROI lie on the radial spikes from the star point. Additional points, specifying foreground and background, are often necessary. By allowing the user to select the centre point, and not calculating it based on geometric centre, more complicated and convex images can be segmented, provided they are star shaped with respect to the arcs from the user point. Star shaped graph cut formulates a graph in a similar manner to other graph cut paradigms, namely a graph $G = (V, E)$ with each edge $e \in E$ having a non-negative weight w_e. A ballooning term is also used to discourage bias towards the formation of small segments. However, the method can only segment the convex shapes. A commonly used energy function
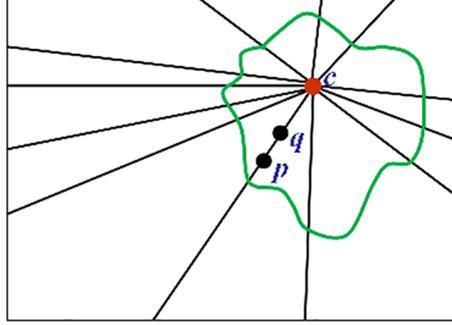
Figure 2.21: Star shaped graph cut. Radial lines from the user point c provide the star shape [24]. As both p and q are points that lie on the same line through c, and q is closer to c than p. It therefore follows that if p is labeled object, q must also be labeled object.

for these types of graph cut is:

$$E(f) = \sum_{p \in P} D_p(f_p) + \lambda \sum_{(p,q) \in N} V_{pq}(f_p, f_q). \tag{2.3}$$

The first term is referred to as the data term, and the second the boundary term and measures how well a given pixel p fits into the background or foreground regions by looking at the penalty $D_p(f_p)$ to assign the label f_p to that pixel. To ensure correct segmentation, $D_p(0) = \infty$ is set for object seeds, and $D_p(1) = \infty$ set for background seeds (points labeled as such by the user). The second term, $V_{pq}(f_p, f_q)$ is the penalty for assigning labels f_p and f_q to neighbouring pixels, which is zero if the labels are the same, but penalizes differing labels. $\lambda \geq 0$ is a weight for scaling the relative importance of the two terms.

An example showing the arrangement of lines and points is shown in Fig. 2.21. In the example, if point (pixel) p and q lie on a line through the user centre c with q in between p and c, it therefore follows that is label 1 for object is given to p, then all points between p and c must be so labeled. β is a bias added to prevent shriniking in the absence of a strong data term. This is implemented using the pairwise shape constraint term shown:

$$S_{pq}(f_p, f_q) = \begin{cases} 0 & \text{if} f_p = f_q, \\ \infty & \text{if} f_p = 1 \text{ and } f_q = 0, \\ \beta & \text{if} f_p = 0 \text{ and } f_q = 1 \end{cases} \tag{2.4}$$

Gulshan *et al.* [130] have extended the method to multiple stars by using geodesic paths instead of Euclidean rays. Other interactive segmentation methods such as a transductive framework of Laplacian graph regulariser [131] have been also introduced.

2.6.2 Log Gabor Filters

Gabor filters are a family of bandpass filters widely used in many aspects of image processing [132]. Indeed there have been many applications using these filters such as vehicle identification [133, 134], face recognition [135, 136, 137], biometrics [138, 139], and even character recognition [140, 141]. In our work we use Log-Gabor filters [142] to remove noise based artifacts from the image prior to segmentation. They can be described in the Fourier domain using the following equation:

$$G_k(r,\phi) = \exp\left(-\frac{1}{2}\left(\frac{\log(\frac{r}{r_k})}{\sigma_s}\right)^2 - \frac{1}{2}\left(\frac{\phi - \phi_k}{\sigma_a}\right)^2\right) \tag{2.5}$$

where (r_k, ϕ_k) represents the centre of the filter, and σ_s and σ_a represent the scale and common angular bandwidths respectively. All the filters share one scale bandwidth, and $\frac{\pi}{4}$ angular bandwidths. Log-Gabor filters are common for image enhancement and noise reduction as they possess a similarity to how the visual cortex processes images [143, 142]. Gabor functions comprise of two components; one real part, and the other imaginary, with the actual Gabor function being a multiplication of a Gaussian function and a complex sinusoidal function in the corresponding spatial domain.

The Log-Gabor function which we use in this work $Gab(f)$, has a frequency response defined as a symmetric Gaussian on a log frequency axis:

$$Gab(f) = \exp(-\frac{[\log(f \backslash f_0)]^2}{2[\log(\sigma \backslash f_0)]^2}) \tag{2.6}$$

where $f0$ is the centre frequency of the filter, and s is the filter bandwidth. The Log-Gabor function has no DC component for any bandwidth filter compared to the Gabor function.
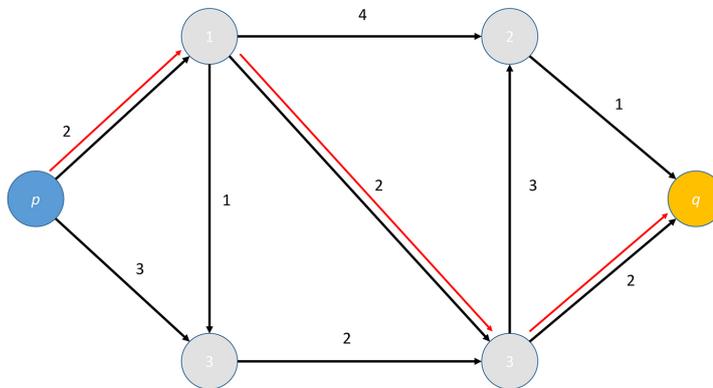
Figure 2.22: Simple schematic representing shortest path segmentation using Dijkstra's algorithm. The resultant path is shown with red arrows. The method will select the unvisited vertex with the lowest cost (in this case 1, calculates the total cost of visiting it and each unvisited neighbor, and updates the neighbor's distance if smaller

2.6.3 Shortest Path Methods - Dijkstra's Algorithm

Shortest path segmentation is an edge based approach to image segmentation. There are many different methods and algorithms used [144, 145, 146, 147], one of the most common is Dijkstra's Algorithm This algorithm was published by Dijkstra in 1959 [148]. Dijkstra's algorithm is a method to find the shortest path between two points (pixels) p and q. The algorithm supposes that there is a point r that exists on the minimal path between p and q. The algorithm finds these minimal paths from point p to various points r until q is reached. The nodes on the graph are divided into three sets A, B, and C. These represent the set of nodes where the minimal path to p is known, those nodes connected to a node just added to A (that is those nodes to be examined next), and the rest of the nodes in the graph respectively. The edges are thusly also divided into three sets, with similar groupings. The algorithm thus finds the shortest path between the node p and every other node r until q is reached. This is not the most efficient algorithm for calculating the shortest path as it runs in time $O(|V|^2)$, where $|V|$ is the number of nodes in the graph. Fig. 2.22 shows a simple example of Dijkstra's algorithm. The result from p to q will include node 1 and 3 and will have length 6.

Modern implementations of the Dijkstra Algorithm however, employ a Fibonacci heap, which

provides them with a runtime of $O(|E| + |V|\log|V|)$ where E is the number of edges in the graph [149].

2.6.4 Edge based Detection

Throughout this work, we utilize edge based detection methods to identify features. Edge detection is ubiquitous in object detection [150], medical imaging [151, 152], as well as in other image processing applications, and although there are many different mechanisms to achieve the desired result, most rely on a change in the gradient of specific values (more often the luminance) that occurs across the border (or edge) [153]. The principle is to assign a value to a threshold change in luminance (usually in a grey-scale image), this threshold represents the minimum gradient across the edge that will be defined as a boundary. This will usually be after performing any pre-processing to enhance the edge features [154].

For a relatively simple edge detector, a step edge with applied Gaussian blur could be used [155, 156] which uses a gradient magnitude to form the basis of the edge detector. Edge detection can be classified into several different categories, based on how it works and the types of pre-processing required. Pre-processing can either be local, regional or global depending on the requirements of the system. These different methods of preprocessing look at different size neighborhoods to improve the edge quality prior to detection. Both local and regional methods apply various size templates to the image, with idealized edge conditions to improve the edge feature. Global methods apply a filter to the whole image. In our method, our first stage of preprocessing involves applying one of these global filters. After pre-processing, there are many different methods that can be used for edge detection. In this work, we mainly use two different algorithms, Canny and Sobel edge detectors. The Sobel Filter (or Operator) is a commonly used edge detector in image processing [154, 157, 158, 159], performing a 2-D spatial gradient measurement on the image. This has the effect of emphasizing regions of high spatial frequency, which in turn correspond to edges in the image. Applying the Sobel Filter to a Greyscale image can be used to approximate absolute gradient magnitude at each point. It is named after the researcher Irwin Sobel, who presented the Operator in his work. The filter itself consists of two $3x3$ matrix kernels that can be applied to a given (x,y) image $\mathcal{I}$. These are used to map horizontal and vertical changes in gradient, giving the approximations G_x and G_y respectively (2.10). The image I can be convolved with both G_x and G_y to give the approximate gradient magnitude G at any given point (2.9).

$$G_y(x,y) = \sum_{k \leftarrow 1}^{1} \sum_{l \leftarrow 1}^{1} S_1(k,l) f(x+k, y+l) \qquad (2.7)$$

$$G_x(x,y) = \sum_{=k1}^{1} \sum_{l \leftarrow 1}^{1} S_2(k,l) f(x+k, y+l) \qquad (2.8)$$

$$G(x,y) = g_1^2(x,y) + g_2^2(x,y) \qquad (2.9)$$

$$G_x = \begin{bmatrix} -1 & 0 & +1 \\ -2 & 0 & +2 \\ -1 & 0 & +1 \end{bmatrix} \star \mathcal{I} \qquad G_y = \begin{bmatrix} -1 & -2 & -1 \\ 0 & 0 & 0 \\ +1 & +2 & +1 \end{bmatrix} \star \mathcal{I} \qquad (2.10)$$

Where $\star$ represents the 2-dimensional convolution operation.

After the filter is applied, G can be approximately calculated using the equation (2.11).

$$G = \sqrt{G_x^2 + G_y^2} \qquad (2.11)$$

The Canny edge detector [160, 161], expands upon the results obtained from the Sobel Filter. Taking the gradient magnitude obtained by applying the Sobel filter to the image (2.11), and applying further processing to it. Firstly, an "edge thinning" technique is applied to the image resulting from the Sobel filter. This suppresses all non-maximum values for the edge to zero, resulting in a single, maximum value for each edge. The next stage is to remove erroneous edges caused by noise in the image. THis is done by setting two threshold values (a high and low threshold). Edges where the pixel value falls between these are labeled as weak edges, and those below the low threshold are suppressed. Finally edge tracking is used to select which weak edges (those connected to a strong edge) should be included in the final image. The Canny edge detector again is quite commonplace in image processing [162, 163, 164] being found in many different applications. The direction of the gradient obtained by the Sobel filter can be achieved [165] using the following formula:

$$\theta(x,y) = \tan^{-1}\left(\frac{G_y}{G_x}\right) \qquad (2.12)$$

The edge detected from the gradient magnitude is quite "blurry". The Canny filter improves upon this by using an edge thinning technique. It uses the direction of the gradient to reinforce

Figure 2.23: Comparison of Sobel (centre) and Canny (right and far right) edge detector (high and low thresholds respectively) filters applied to an image

edges in a certain direction, and reduce edges in the other directions. This results in the resultant edges being more defined, with less smoothing Fig.2.23. By changing the threshold value used, the canny edge detector can be used to detect weaker edges. This made it very suitable for the over-segmentation stage used in our preprocessing.

2.6.5 Radial Basis Function

A Radial Basis Function (RBF) can be used for a wide range of interpolation and smoothing tasks in a variety of different fields, including smoothing of 2D [166, 167, 168] and 3D contours [169, 170, 171]. An RBF is a real-valued function, and it derives its value from the distance from a predetermined point, called a *centre*, c, with any given function ϕ being *radial* if it satisfies the property $\phi(x) = \phi(\|x\|)$.

$$\phi(x,c) = \phi(\|x-c\|) \tag{2.13}$$

There are several different types of RBF commonly used, depending on the approximations and smoothing required. These can be Gaussian, Multi-quadratic or Poly-harmonic, as well as Thin plate Splines, amongst others (such as the inverse of the above). When writing an RBF, it is common to use the term r, where $r = \|x - x_i\|$. For a Gaussian RBF, we can use the following term:

$$\phi(r) = e^{-(\varepsilon r)^2} \tag{2.14}$$

RBFs can be used in kernel smoothing, which is what we use them for in this work. A typical RBF used for kernel smoothing can be represented by (2.15) where $y(x)$ is our approximation

function, represented by the sum of *N* RBFs, each of which has a different associated centre x_i, with its associated weight w_i.

$$y(x) = \sum_{i=1}^{N} w_i \phi(\|x - x_i\|) \tag{2.15}$$

2.6.6 Hidden Markov Model (HMM)

HMM is a stochastic model, in which over a finite set of hidden states, the Markov property can be assumed to be satisfied. The Markov property represents the "*Memoryless*" nature of the series and, for a *first order* Markov Property, states that for any given state at observation time t (S_t), this state is governed by the state at $t-1$, but is independent of all previous states before $t-1$ [172]. What this means is that the current state, confers all we need to know about the previous states. This must also therefore hold for the outputs, as they must be independent of the historical states as well. This means that given S_t, Y_t must be independent of all the previous states and observations. HMMs have been utilized in a variety of fields, such as speech recognition [173, 174] , classification [175, 176] and tracking [177, 178]. HMM has been used in the medical field both for segmentation [176, 179, 180] and image processing, such as image denoising [181]. In this work, we propose multi-border segmentation and tracking method based on the HMM, in order to delineate the inner and outer vessel borders in lymphatic images with the presence of noise and occlusions.

In its most basic sense, a HMM is a tool for investigation and representation of a series of probabilities for a selection of observations [182]. We can use HMM for any variable, Y_t observed at time t, provided that we can define its probability distribution and that the observations can be sampled at discrete times (t must be an integer). In order to be a HMM, certain criteria must be met. Firstly, our observation at time t must be triggered by a process that is hidden from the user, and this state which we shall refer to as S_t maintains the *Markov property*. The final assumption we make when assigning the Markov property to a system is that each state S_t is also discrete, taking on $k \in (1, ..., K)$ integer values.

We can represent this sequence of states using the following equation to show the distribution of a sequence of states and observations:

$$P(S_{1:T}, Y_{1:T}) = P(S_1)P(Y_1|S_1)\prod_{t=2}^{T} P(S_t|S_{t-1})P(Y_t|S_t) \tag{2.16}$$
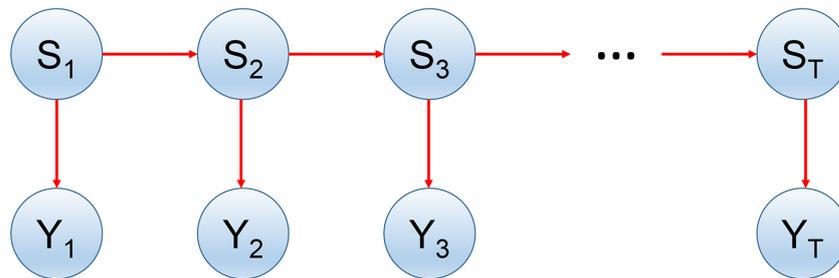
Figure 2.24: Representation of a simplified Bayesian network representing the dependencies in HMM

Where the observations at time $t \in T$ are taken for each state S and observation Y. We can represent this graphically (as shown in Fig. 2.24). This representation of the hidden states and their observations is known as a *Bayesian* (or belief) network. We can represent a Bayesian network as a graph, with each variable we consider being represented as a node. Each node will therefore be connected to nodes that are dependent on it, and also be connected to those node on which it depends by using a series of directed and weighted arcs.

In order to use the HMM in our method, we must first define the probability distribution over the initial state $P(S_1)$, the $K \times K$ transition matrix used to define $P(S_t|S_t - 1)$, and how we model the output defined by $P(Y_t|S_t)$. It is standard practice to ensure that both the transition matrix and the output models are not dependent on t. This means that the model must be *time invariant* apart from in defining the initial state. Our observations (position of the boundary in each slice), being discrete, can take one of L values, so we can define our output by using a $K \times L$ *emission* matrix.

2.7 Optimization

In image segmentation, it is important in most cases that accurate segmentations are performed with a high degree of fidelity. This, however, isn't the only requirement in a great number of situations. For the most part, it is also essential that the segmentation process have some degree of optimization, to reduce the run-time or the computational cost of the algorithm. One can broadly separate optimization problems into two categories, being either continuous or discrete, or in some cases, they may be a combination of both. The principle difference between

the two cases is the type of variable that they deal with. Discrete optimization, for example, is primarily used in the case where the variables may only take on discrete (most commonly integer) values. Continuous optimization deals with the opposite case, that in which the variables are allowed to take on any values permitted by the constraints, so-called continuous variables. Discrete problems are often very hard to solve, often only enumeration of all possible points is required in order to obtain a solution; although, fortunately, this is not always the case and simple (greedy) algorithms can suffice. As well as the two broad categories of optimization, it is also essential to understand whether the method used provides a global minimization (all the variables are considered as a whole) or produces localized *minima*.

2.7.1   Global Minimization

This can be defined as finding the global minimum (or in some cases the maximum) over a series of *n* parameters, with or without the addition of constraints [183]. For finding the global minimum this can be expressed as:

$$\underset{x}{minimise} f(x) \tag{2.17}$$

Where f is the objective function and x is a vector incorporating the variables. If these variables that enter x are real numbers, then the problem in continuous, and if they are integers, then the minimization problem is discrete. It is quite common for global minimization problems to be governed by constraints (such as box constraints that set an upper or lower boundary to the problem). In this case, the algorithm will find a global minimum *within* the constraints established. This global minimization paradigm will be used in this work, to avoid segmentations forming undesirable local *minima*.

2.7.2   Discrete Optimization

In discrete optimization, there is present a set of *n* discrete variables (such as integers, binary values, etc.), and the solution is found within a combination of them. An example of this would be trying to "guess" at a PIN. This seems quite straight forward at first, as all possible combinations can be predicted, but the number of combinations soon becomes high. In the trivial example of the 4 digit PIN, there are 10^4 combinations, simple for a machine, but time consuming for a human. However, in image processing, the number of permutations is increased

by orders of magnitude. For example, a 512×512 JPG color image has (for one color channel alone):

$$512 \times 512 = 262,144 \text{pixels}$$

$$262,144^{256} \text{combinations} \tag{2.18}$$

$$\text{(which MATLAB reports as Inf)}$$

As demonstrated above, without tight boundaries, discrete optimization problems become quite taxing on computational resources and time. As discrete optimization problems are relatively common in a lot of fields (such as manufacture, engineering, telecommunications, etc.) it is important to provide algorithms that can find solutions to the problem in faster time than simply iterating through the possible permutations. Discrete optimization problems can also occur in graph theory, something that is widely used in image segmentation. The set of all possible solutions S for any given graph might include the set of spanning trees (a spanning tree of graph $\mathcal{G}$ is a subgraph that includes all vertices) in the connected graph. For any given graph $G = (V, E)$ comprised of n vertices, there will be n^{n-2} spanning trees. This creates a problem in the same order of difficulty as sorting the $\binom{n}{2} = n(n-1)/2$ different edge weights. Another commonly cited problem is that of the traveling salesman, which has an hypothetical salesman visiting n sites on his route. Without some governing constraint, this gives $(n-1)!/2$ possible combinations, and is in in fact NP-hard, being very computationally expensive. It is generally considered that any algorithm is *theoretically efficient* if the number of computational steps can be solved in polynomial time (i.e. it is not NP-Hard) [184]. In this work, we will utilize a sequential order to our graph in order to prevent the problem becoming NP-hard.

2.7.3 Continuous Optimization

Continuous optimization methods deal with data that transitions gradually between values in the range, i.e. continuous data. As discussed in Unger *et al* [185] these methods are inherently parallel, making them ideally suited to modern GPU applications. It is possible to apply standard methods, such as max-flow/min-cut, which is traditionally used with discrete optimization, to continuous optimization problems. Strang [186] provided an extension to the max-flow/min-cut theorem for continuous flow. In the continuous case, it becomes easier to solve for the minimum cut rather than looking at the maximal flow. In the continuous opti-

mization problem, the flow is looked at as a continuous flow bounded in a domain plane, and its direction and magnitude are given by the vector field σ for any point (x, y) where:

$$\sigma = (\sigma_1(x, y), \sigma_2(x, y)) \tag{2.19}$$

By integrating $\sigma \cdot n$ where n is the unit normal to the segment, we can obtain the flow across a line segment. The capacity constraint for this, takes the pointwise form:

$$|\sigma(x, y)| = (\sigma_1^2 + \sigma_2^2)^{\frac{1}{2}} \leq (c(x, y) \tag{2.20}$$

In place of a conventional source and sink, the continuous flow exits and enters through the boundary of the domain, with positive values for flow leaving through the boundary associated with a sink, and the converse for negative flow (representing, therefore, leaving the boundary representing the source).

As the balance of flow can be formulated as:

$$\int \int F \, dx dy + \int f \, ds = 0, \tag{2.21}$$

allowing the problem to be expressed as:

$$\begin{aligned}
&\text{Maximize } \lambda, \\
&\text{subject to } |\sigma| \leq c, \\
&\qquad \sigma \cdot n = \lambda f, \\
&\qquad \text{div} \sigma = -\lambda F,
\end{aligned} \tag{2.22}$$

As you can see from the graph cut example, continuous optimization problems are generalized in the form:

$$\begin{aligned}
&\underset{x}{\text{Maximize}} f(x), \\
&\text{subject to } g_i(x) \leq 0, i = 1, \ldots, m \\
&\qquad h_i(x) = 0, i = 1, \ldots, p
\end{aligned} \tag{2.23}$$

Where $f(x) : \mathbb{R}^n \to \mathbb{R}$ is the objective function; i.e the function to be minimized over the variable x, and g_i and h_i form the inequality and equality constraints respectively. This is defined by convention as a minimization problem 9obviously a maximization problem could be solved by negating the objective function).

Chapter 3

Interactive 2D Segmentation: Utilizing edge and region information to enhance segmentation

Contents

3.1   Introduction

In this chapter, we proposed an approach combining two different types of user interactions, i.e. boundary based interaction (utilizing the user input control points) and region based stroke interaction, to segment medical images from Intravascular Ultrasound (IVUS) and Optical Coherence Tomography (OCT) images.

By utilizing a series of soft constraints to guide the image segmentation, in combination with stroke based region selection we obtain a robust segmentation method, that deals with the quality issues present in images obtained with these (IVUS and OCT) modalities. Soft constraints

Figure 3.1: Overview of an IVUS image acquired by 40MHz transducer Boston Scientific ultrasound machine, and segmentation by the proposed method. (A) Original IVUS image. (B) User input. (C) Segmentation result.

do not require the segmentation path to go through the points exactly, acting as a guide rather than a fixed point. The opposite are hard constraints, which require the pathway to travel through the point itself. In both IVUS and OCT images there are varying amounts of image noise, and artifacts (caused by both medical conditions and as a result of the imaging method), which by using the dual method of edge based and region based features the effect of these on the quality of the segmentation is minimized. By switching to soft constraints, rather than the more common hard constraints, imprecise user input is allowed without adversely affecting the segmentation. This use of imprecise user input reduces the time taken for the user to make user selections (and therefore the convenience of the technique) allowing for an easier balance between the desire to use expert knowledge to inform the segmentation and convenience of use for the end user. To further augment this edge based approach, we allow the user to select regions for foreground interest with strokes; allowing effective combination of boundary and region based features in a wide variety of image modalities. The user points give the user control over the segmentation process, allowing errors in segmentation to be easily prevented and a more desirable result to be obtained. Fig. 3.4 is an example of an IVUS image which shows the typical quality of the image type where not only artifacts, but pathologies may increase the difficulty of the segmentation. In both the IVUS and OCT image sets we look at the segmentation results in both qualitative and quantitative fashion, comparing them to other methods of segmentation. To further demonstrate the versatility of the method, we will then look at some examples from other imaging modalities, such as x-ray, MRI and CT, and "real world" images (landscapes, animals, people and objects. In these examples, we demonstrate the capacity of method to allow both open and closed selections to be made, one of the fundamental features of our method.

In this chapter, the principle drive is to investigate image segmentation in images obtained from catheter based diagnostic methodologies, widely used in hospitals, namely IVUS and OCT. Due to the differences in both imaging modalities (IVUS having a higher penetration, but lower resolution, for example) we look at the medi-adventitia border on the IVUS images (clearly visible as a dark band), and the lumenal border in the OCT data-sets (much more visible in this modality).

The rest of the chapter is organized as follows: Section 3.2 presents the proposed method, including user input, super-pixel segmentation, and multilayered graph segmentation, as well as an overview of the cost terms and minimization method. Experimental results from segmenting medical data sets with ground-truth are presented in Section 3.3. These show the results for IVUS and OCT images, and quantitative data obtained from these data-sets, demonstrating the effectiveness of the technique compared to other methodologies. We show a selection of examples from other medical imaging modalities to demonstrate that the method can be used for other image types and then show results for generic images, further demonstrating the versatility and robustness of the method. Section 3.5 concludes the chapter.

3.2   Proposed Method

The proposed method involves following these steps, summarized in Fig. 3.2:

1. The user selecting a series of user control points on the image. These represent the start and the end point for the segmentation, and the user selected points act as the attraction points in the shortest path search which results in the segmentation. These user selected points act in a fashion similar to an elastic band, pulling the segmentation towards them. In this way, it is possible for the user to influence the segmentation process allowing them to preferentially select features that they want, but without the caveat that these points must be precise. In order to enhance the image segmentation, the user can also select areas for foreground using strokes.

2. With the assumption that the user points are in a sequential order (as without this the problem will be NP-hard and computationally intensive), we construct a multi-layer graph with each layer encapsulating a single individual user point, each layer being a complete rendition of the image. Effectively, we create multiple identical layers, all
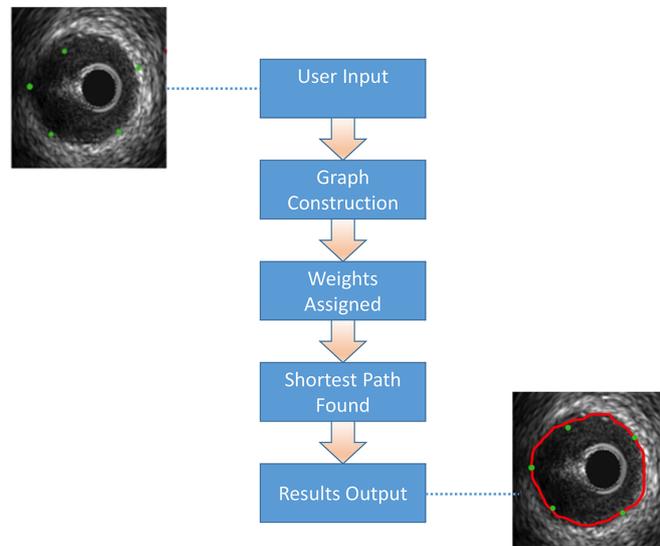
Figure 3.2: Schematic of the stages involved in the method. Starting with user input, a 3D graph is constructed for $n+1$ layers, where n is the number of user points. Weights are then assigned, and the shortest path found. This is then converted back to a 2D representation for output.

made up of duplicates of the image, for each user point added, with the only difference between layers being the position of the user point on that layer.

3. An energy function is then formulated based on the combination of the attraction force (that is computed using distance transform based on the next user point), the edge features between neighboring pixels, and the discontinuity in foreground probability. This is then used to assign weights to the edges in the graph.

4. The segmentation problem is then transformed into searching the shortest path in this layered graph, that is the resulting segmentation is obtained through searching a minimum path in this stack of layers in a manner similar to a 3D object.

Another effect caused by the creation of layers is that order is forced onto the problem. As the edges between layers are unidirectional, the segmentation must proceed from the first layer to the last without revisiting a previous layer. With no sequential order to the points, the problem becomes that of the traveling salesman, and becomes NP-Hard. By using the layered approach, which ensures sequential transition between layers, the segmentation can be carried

out in polynomial time, instead of an NP-hard optimization problem, at the same time achieving global minima.

3.2.1   User Input

The proposed method allows two different types of user input: (a) attraction points to indicate the edge of the desired object and (b) strokes to indicate region of interest. Fig. 3.3 provides an example of segmentation using the proposed method. Conventionally, user input to segmentation is focused on foreground and background specification [21, 25, 121, 24]. For example, in [25], the user interaction consists of dragging a rectangle around the object of interest and in doing so the user specifies a region of background that is modeled in separating the foreground object. Several other methods require user to specify points on the object boundaries instead [122, 11, 12]. Examples of these methods are shown in Fig.3.4. However, more often than not, these boundary based user points are treated as anchor points and the segmentation path has to go through them. This kind of hard constraint is not always desirable. It does not allow imprecise user input, and it can lead to difficulties in combining region based and boundary based approaches as discrepancy between different object descriptions is generally expected. Notably, in [12] the authors introduced soft constraint user point by embedding the user constraint in distance functions. The segmentation result is considered to be the shortest path to loosely connect the user points. However, it is known to be a NP-hard problem. Hence, it is assumed that the user points are placed in a sequential order and such a constraint reduced the computational complexity to polynomial time. This user input constraint can be seen to be generally acceptable as it is intuitive to follow the outline of an object, rather than skipping around. In this work, we follow this approach to treat boundary based user points. However, we also allow user to place region based strokes. These strokes are used to model foreground probability, and the discontinuity in foreground probability indicates the presence of object boundary. We combine these two types of user input with image features in an energy functional which is then optimized using graph partitioning through finding the shortest path from the first to last user points. Moreover, we apply a super-pixel segmentation in order to generate a much coarser, but irregular, multi-layer graph so that the computational cost is drastically reduced. It also provides a regional support at a low level for the shortest path search in the graph.
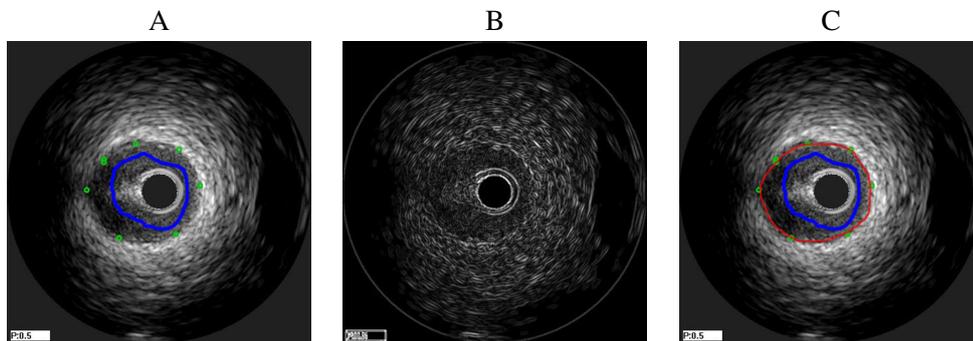
Figure 3.3: Edge based detection in IVUS images. From left to right, (A) shows initial image with user selections added,(B) shows the resultant edge map obtained,and (C) shows the segmentation produced (shown in red), green shows the ground truth, and blue user selections.
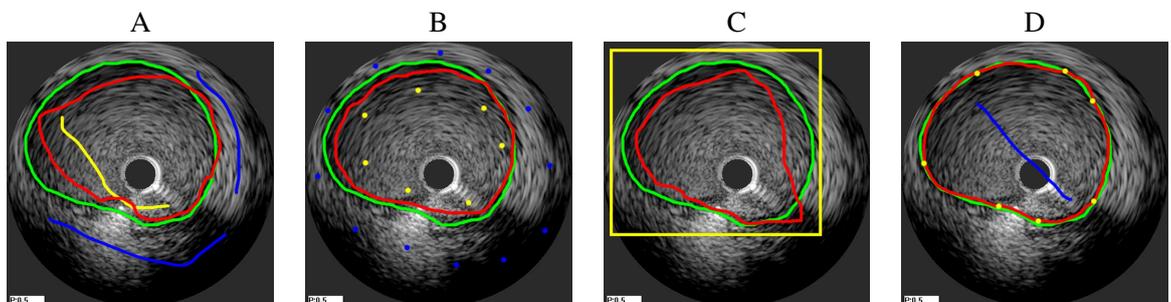
Figure 3.4: Examples of different segmentation methods on an IVUS image. From left: (A) Graph cut [21],(B) Seeded Star Graph Cut [24], (C) GrabCut [25], and (D) proposed method. Red curve shows the segmentation result, yellow for user points and blue for region selection (in the case of the proposed method), yellow and blue points/strokes for foreground/background regions in graph cut and seeded star graph cut, and yellow for the initial window of the Grabcut. Green shows the ground truth from manually labeled image.

3.2.2   Pre-processing

The first stage in the segmentation process is to pre-process the images. When looking at both IVUS and OCT images, there are a lot of artifacts and noise that can hinder a good segmentation. Noise reduction in IVUS is important as many segmentation systems utilize edge based techniques, and there are several methods that can be used [125, 124, 187]

In our method, we implement a Log Gabor filter in order to improve the noise present in the image data and have been shown to improve the quality of images in similar situations [123]. By utilizing a log-Gabor transform function to act as a bandwidth filter, the noise of the

image (which is out of phase) can be removed. Using Gabor wavelets instead of log-Gabor, has problems dealing with certain types of noise, especially those occurring in negative frequencies relative to the desired image.

3.2.3 Super-pixel Segmentation

Efficient search for the shortest path, for instance, using Dijkstra's Algorithm on a multidimensional graph is not a trivial task. Many researchers attempted to speed up the Dijkstra's Algorithm by e.g. using multilevel scaling [188] or restricting the search space [189] by deciding whether or not the edge will be considered during the searching process. One mechanism that can be used to minimize the amount of nodes on the graph is Super-pixel Segmentation. Super-pixel segmentation is a process that groups a set of homogeneous neighboring pixels together to reduce the complexity of solving further image processing such as segmentation [23, 118] and object localization [190]. Super-pixel segmentation algorithms vary from graph based [72, 191] to gradient descent methods [192, 193].

In order to optimism the segmentation, and speed up the segmentation of the images using Dijkstra's Algorithm, a graph pruning method was implemented. Graph pruning was achieved by the utilization of a mean shift method to over-segment the image, and thus create the Super-pixels. This over segmented image is then used to prune the graph, by only considering the boundary of the super-pixel regions as a potential paths that can be used to find the shortest path between two points, the whole process is thus far more efficient. Additionally, this super-pixel segmentation provides low level regional information to the graph search which relies significantly on edge information.

Mean shift algorithm [192] is a non-parametric gradient descent method that iteratively shifts the mean of the region toward the local maxima of the cluster density for a given set of samples. Mean shift method is suitable for clustering data without any assumption of the cluster shape. It has been widely used in many applications, such as segmentation [192] and tracking [194]. Given n data points (pixels) the pixel x_i where $i = 1 \ldots, n$, in the d-dimensional space R^d, the non-parametric probability function is defined by kernel density estimator (KDE) as the following:

$$\hat{f}(x) = \frac{1}{nh^d} \sum_{i=1}^{n} K\left(\frac{x - x_i}{h}\right) \tag{3.1}$$

where h is the bandwidth parameter and K is the radially symmetric kernel such as Gaussian
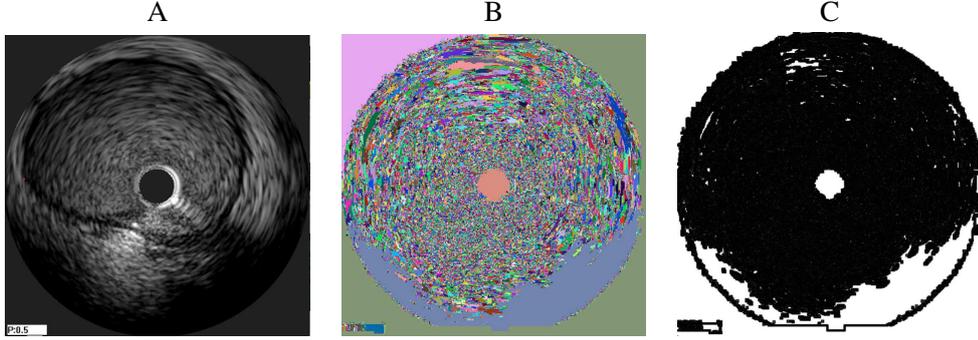
Figure 3.5: The use of super-pixel segmentation to identify graph nodes in a single layer in IVUS image. From left to right, (A) initial image, (B) super-pixel segmentation, (C) representation of utilized graph nodes (black is used in graph, white is not).

kernel.

$$K(x) = (2\pi)^{-d/2} \exp(-\frac{1}{2} \|x\|^2) \tag{3.2}$$

The local maxima of density is located among the zeros of the gradient $\|\nabla f(x)\| \cong 0$. So the mean shift can be derived as the following:

$$m_{h,G(x)}(x) = \frac{\sum_{i=1}^{n} x_i G(\|\frac{x-x_i}{h}\|^2)}{\sum_{i=1}^{n} G(\|\frac{x-x_i}{h}\|^2)} - x \tag{3.3}$$

where

$$G(x) = c_{g,d} g(\|x\|^2) \tag{3.4}$$

With $g(x) = -K\prime(x)$ and $m_{h,G(x)}(x)$ is the difference between the weighted mean, using kernel G, and x, the center of the kernel. The mean shift vector points toward the maximum increase of the density and it converges at a nearby point where the density estimate has zero gradient.

Fig. 3.5 provides an example of the mean shift segmentation. Mean shift is preserving the edge features in the image. The black region, shown in the rightmost of the figure, represents areas on or close to edges in the super-pixel segmentation, and are used to construct the graph as it is discussed in the next section. In order to prevent the segmentation being too jagged in IVUS images, it was necessary to increase the amount of segmentation obtained in this stage.

Cells can be combined if they are all labeled the same by the user, in order to create a larger super-pixel. In this way, redundant edges internal to regions are not included in the graph. We apply a Canny edge detector to the super-pixel images to create a binary image which we can
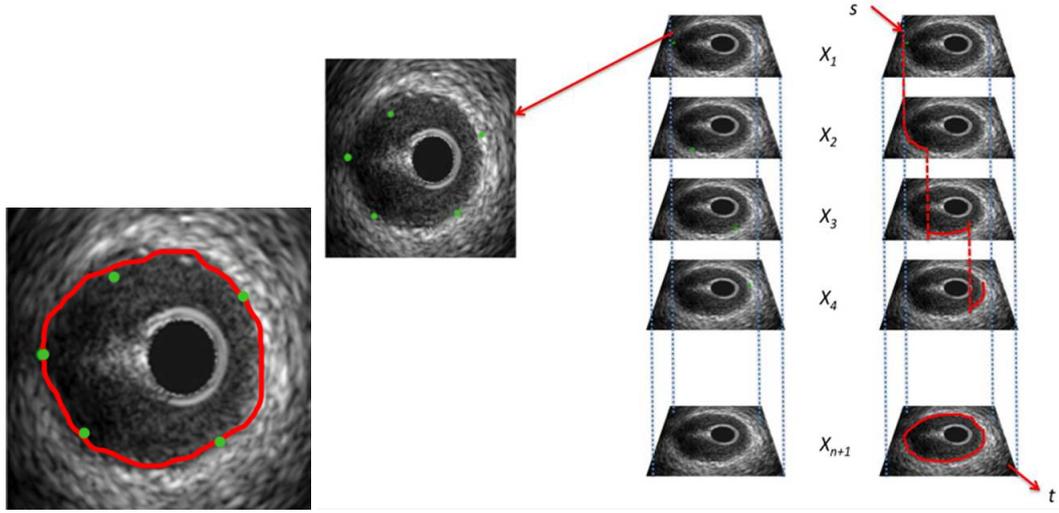
Figure 3.6: Example of 3D graph traversal. The stack of images on the right show how the graph is constructed out of a number of layers corresponding to the number of user points $n+1$. The algorithm finds the shortest path through the layers, solving the minimum cut for the graphc ut with weights derived from the edges, boundaries and distance from user points. The final result of the segmentation is shown on the left.

then use to assign nodes to the graph based on whether they are present on the edges of the super-pixels or not. The Canny edge detector (with a low threshold value) in this case provides an easy way for obtaining the binary of corresponding edges ready for using in the next stage. A Sobel filter, due to its smoothed nature, would give more values to the mask (unless a threshold was set) diminishing the speed increase obtained by the super-pixel segmentation. See Fig. 3.5 for an example of the super-pixel segmentation.

3.2.4 Layered Graph Construction

In order to impose soft constraint for user point, we follow the approach proposed in [12] to construct a layered graph so that given a set of attraction points we fit a curve to follow the edges in the image and pass through the vicinity of the given points. The user points are assumed to be placed in a sequential order, which is acceptable in most applications. The computational complexity, however, is reduced from being NP-hard to polynomial time.

For each user point, $X_i, i \in \{1, 2, ..., k\}$, we create a new layer of directed graph. This is a copy of the image layer, with the same edge based weighting. In that way we have a series of layers equal to the number of user points n, plus an additional layer in order for the weighting of the

last user point (the sink) to be used, as shown in Fig. 3.6. This results in a multi-layer directed graph, $\mathcal{G} = (\mathcal{V}, \mathcal{E})$, where $\mathcal{V}$ is the set of vertices, and $\mathcal{E}$ the set of weighted edges. For each pixel p, there exits an edge e to each of its neighboring pixels on the same layer, providing that they are on the boundaries of the super-pixels. Therefore, a pair of neighboring pixels $(p,q) \in \mathcal{V}$ with a corresponding edge $e = (v_p, v_q)$ also have an edge to the corresponding point on the superseding layer $e = (v_{p_i}, v_{p_{i+1}})$, where i represents the current layer of the image. For each edge, we assign a weight w to build a weighted graph $(\mathcal{V}, \mathcal{E})$. These weights are calculated based on whether the edge is internal to a layer (w_i) or trans-layer (w_x). By creating the graph in this way, an order is established with the user points, yet allowing for a global minimum to be found, rather than a series of pairwise local minima. Due to the size of the graph that would be constructed, the edge mask created by the super-pixel segmentation is used to prune the graph that has been constructed. If nodes are not on the edges, then they are not used by the algorithm. In this way, weights do not have to be calculated for them, and they take no more part in the computation of the result.

Edges of zero weight are added from the start node s to each pixel in the first layer, and from the last layer $k+1$ to the terminal node t. This has the effect of making the first and the last user points elastic and not hard constraints. For example, if the first user point X_1 is not located on an edge, then in the overall minimization it would be of lower cost to enter the first layer at the nearest point to X_1 on a strong edge. In this way, all user points act as soft constraints.

If P is the set of pixels in the image, P_s is therefore the subset of pixels that also fall on the boundaries of our super pixels, and p_i and q_i are pixels in layer i giving v_{p_i} as the vertex p in layer i, we can define the set of nodes $\mathcal{V}$ as

$$\mathcal{V} = \{s,t\} \cup \{p_i \in P_s \wedge 1 \leq i \leq k+1\} \tag{3.5}$$

and thus the set of edges as,

$$E = \begin{cases} (s, v_{p_1}) | p \in P_s & \cup \\ (v_{p_{k+1}}, t) | p \in P_s & \cup \\ (v_{p_i}, v_{q_i}) | (p,q) \in N \wedge 1 \leq i \leq k+1 & \cup \\ (v_{p_i}, v_{p_{i+1}}) | p \in P_s \wedge 1 \leq i \leq k+1. \end{cases} \tag{3.6}$$

The segmentation is thus to find the shortest path from the start point s to the end point t, see Fig. 3.6 across the 3D graph.

The edges on the directed layered graph are categorized as internal edges w_i within individual layers and inter-layer edges w_x. The weighting for these two types of edges is assigned differently. The internal edges are assigned with two types of weights, i.e. boundary based edge weights and region based edge weights. The boundary based edge weights are calculated based on the magnitude of image gradients, created for example with a Sobel filter,, i.e. using an edge detection function $g_e = 1/(1 + \nabla I)$ where I denotes the image or its smoothed version using, for instance, Gaussian filtering. Hence, for any given edge between neighboring pixels (v_p, v_q), we assign a weight (w_e) according to

$$w_e(v_p, v_q) = \frac{1}{2}||p - q||(g_e(p) + g_e(q)).$$ (3.7)

The region based edge weights are computed from foreground probabilities. The user strokes placed in the foreground provide an estimation for foreground intensity distribution, which is then used to evaluate each pixel in the image. The discontinuity in this generated probability map is then used to compute the region based edge weight in the similar fashion to image intensity, i.e.

$$w_f(v_p, v_q) = \frac{1}{2}||p - q||(g_f(p) + g_f(q))$$ (3.8)

where g_f is the edge detection function based on probability values.

By combining in a weight derived from this discontinuity map, we add an extra level of robustness to the method. As regions not selected as foreground will have an increased cost, if there exists strong edges that may cause errors in our segmentation, but are not selected as foreground then the likelihood of the segmentation following these edges is greatly reduced. This is far more apparent when we look at real world images, as the differing color channels in these images adds even more strength to the region based weights.

The internal edge weight is thus the linear combination of the boundary based weight and region based weight:

$$w_i = w_e + w_f$$ (3.9)

The attraction force imposed by user points is materialized through the inter-layer edge weights w_x. We apply distance transform to the user points in each layer of the graph, and the inter-layer edge weight is assigned as $w_x = d(v_{p_i}, v_{p_j})$ where d denotes the distance transform function. This distance weighting produces isolinear bands of weight around the user point, with increasing weight to go through to the next layer as the distance from the user point increases.
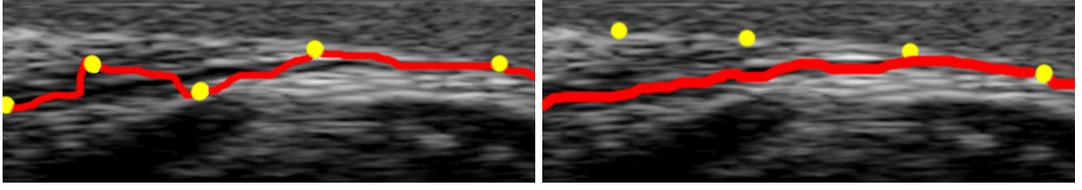
Figure 3.7: Effect of changing α and β. The Image on the left shows the ratio of these two constants skewed towards adding more emphasis on the user points, thus reducing the "elastic" properties. The image on the right shows the other extreme, with the user points being bypassed in favour of the stronger edge.

3.2.5   Energy Minimization

The energy function for any curve C in our method is a combination of three terms, i.e. for any arc C between two points p_i and q_j where the points are

$$C(p,q) = w_x + w_i \tag{3.10}$$

as w_x can be written as

$$\alpha \sum_{i=1}^{k} ||C(s_i) - X_i|| \tag{3.11}$$

and likewise w_i can be written as:

$$\beta \int_0^{L(C)} g(C(s))ds + \int_0^{L(C)} g_f(C(s))ds, \tag{3.12}$$

This is all providing that the points are treated as being in a sequential order, and that the interconnections between layers are uni-directional. The overall energy function can then be expressed as:

$$\mathcal{E}(C, s_1, ..., s_k) = \alpha \sum_{i=1}^{k} ||C(s_i) - X_i|| + \beta \int_0^{L(C)} g(C(s))ds + \int_0^{L(C)} g_f(C(s))ds, \quad s.t. s_i < s_j, \forall i < j. \tag{3.13}$$

where α and β are real constants used to weigh the effects of the edge based and distance based terms. Fig. 3.7 shows how changing the ratio of these constants can be used to put more or less emphasis on the control points (even going so far as to remove the elastic property when the ratio is skewed largely in favour of α.

The first term is used to enforce the soft constraint by the user points, and it penalises the paths further away from the user points. The second term is the boundary based data term that

59

prefers the path passing through strong edges, while the last term is the region based data term which prefers path traveling through abrupt changes in foreground probability. By using the layered graph construction, the minimization of the energy functional is achieved by finding the shortest path from the start point *s* to the end point *t*. The Dijkstra's algorithm is used to calculate the shortest path in the layered directed graph. Note, the inter-layer edges are unidirectional so that the path can not travel back to previously visited layers.

The Dijkstra's algorithm is working on a directed graph $\mathcal{G} = (\mathcal{V}, \mathcal{E})$ to find the shortest path between two defined nodes, the algorithm divide the nodes of the graph into two sets; visited and unvisited nodes. Once the node is marked as visited node, it will not be checked again. The algorithm starts searching from the starting node *s*, assigns an initial tentative distance of zero to the starting node and infinity to all other nodes, and then calculates the tentative distances for all neighboring nodes, these tentative distances are defined as the summation of the edge weight w_i and the current distance of the beginning node of that edge. The edge weight must be non-negative value. The algorithm will mark the node that has the minimum distance as a visited node. The algorithm will repeat the process by calculating the tentative distance for all neighboring nodes for all visited nodes and only mark the node having the minimum distance as a visited node until reaching the terminal node *t*. The running time of Dijkstra's algorithm is $O(|E| + |V|log|V|)$ where *E* is the number of edges and *V* is the number of nodes.

3.2.6 Algorithm Optimisation

Due to the nature of the segmentation, this proved to be a non-trivial task. It is essential to produce a global minimum, rather than a sequence of local *minima* so the whole segmentation had to be considered as one problem. This solution is far more computationally expensive than calculating a series of local *minima*, but produces a more realistic segmentation (avoiding short cuts that would be locally beneficial, but detriment the segmentation as a whole). In order to simplify the graph, we used the methods described previously, which proved acceptable in the data-sets looked at.

3.3 Experimental Results

To show the effectiveness of the proposed method, we test our method for two different medical applications. The two applications use medical data-set of IVUS images that has ground-
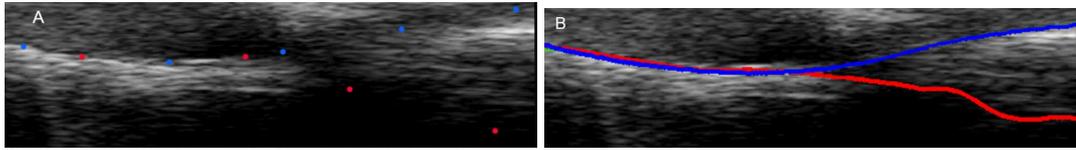
Figure 3.8: Effectiveness in imposing user prior knowledge. As in the natural image segmentation, the user can select different edges by the use of user points. In this case, it can be seen that there are two possibilities for the media-adventitia border in the image. By placing a couple of points, the user can steer the segmentation along the path they desire.

truth available for quantitative comparisons, and a set of OCT images. The segmentation of images in the medical application is very challenging as it generally requires anatomical prior knowledge, as well as other expert knowledge in some cases, in order to sufficiently perform the segmentation task. This makes interactive segmentation the preferred approach to this application. We present comparison to other interactive segmentation techniques. We also show a more generic set of images, to illustrate the versatility of our method, to highlight how it can be used for other (medical) applications.

3.3.1 IVUS Image Segmentation

To study the efficiency and efficacy of the proposed method, we apply our method to a medical image segmentation problem where expert prior knowledge in anatomy is necessary but also often subjective. Here we need to interactively identify the media-adventitia border in IVUS images where imaging artifacts are common place.

There have been many different approaches to the problem of segmenting IVUS images, e.g. [195, 196, 110, 44, 197, 105, 198]. These can be broadly categorized into fully automatic methods, or semi-automatic methods. In [195] the authors used contour detection and tracing with smoothness constraint and circular dynamic programming optimization to segment lumen border. The algorithm assumes homogeneity of the lumen region and high contrast between lumen and artery wall. Katouzian *et al.* [196] applied complex brushlet transform and constructed magnitudes-phase histograms of coefficients that contain distinct peaks corresponding to lumen and non-lumen regions. The lumen region is then segmented based on K-means classification and a parametric deformable model. Homogeneity of the lumen region is critical to the success of the method. Methods based on region growing, e.g. [197], also suffers from such limitations, since artifacts and irregularities are very common in IVUS images. Particularly for

media-adventitia border, the region inside the border is non-uniform as seen in Fig. 3.1. Calcification in arterial wall leads to acoustic shadowing and high reflectance, as well as catheter and guild wire occlusion and artifacts. Stent placed against internal wall also produces strong features and acoustic shadows that break homogeneity. Incorporating user prior knowledge into segmentation hence is often necessary and has been shown to be an effective approach. For instance, Essa *et al.* [110] incorporated a shape prior into graph cut construction to regularize segmentation of media-adventitia border. However, these approaches generally require significant amount of training data and model re-training is often necessary in order to adapt to new data-set. In [44] dynamic programming was used to incorporate edge information with a rudimentary prior, this required manual initialization but set the way for other more advanced techniques for incorporating priors. The work in [198] carried out border detection on the envelope data before the scan conversion. The authors applied spatio-temporal filters to highlight the lumen, based on the assumption that the blood speckles have higher spatial and temporal variations than arterial wall, followed by a graph-searching method similar to [44]. However, image features introduced by acoustic shadow or metallic stent would seriously undermine the assumption.

User initialization is an alternative approach to transfer expert knowledge into segmentation, e.g. [71, 25, 121, 24, 122, 11, 12]. However, most user interactions are limited to either boundary based landmark placement or strokes indicating foreground and background regions. We adapt the approach of combining two different types of user interactions, i.e. boundary based and region based, to segment media-adventitia border in IVUS. The user points are treated as soft constraint, instead of hard constraint in most interactive segmentation methods. We show that this soft user constraint allows effective combination of boundary and region based features. The method is evaluated on an IVUS data-set with manually labeled ground-truth and compared against state-of-the-art techniques. Fig. 3.8 illustrates the benefit of using user interaction to effectively influence segmentation result. Through simple user input, the expert knowledge of the user can be put into place, whilst being augmented by the automatic process. Fig. 3.9 and Fig. 3.10 provide several examples of IVUS images (the ground-truth of media-adventitia layer can be seen in green). Fig. 3.11 shows further examples of IVUS image segmentation using single method approach and our proposed full method.

Star Graph cut [24]	Seeded Star GC [24]	Single Method [12]	Proposed method
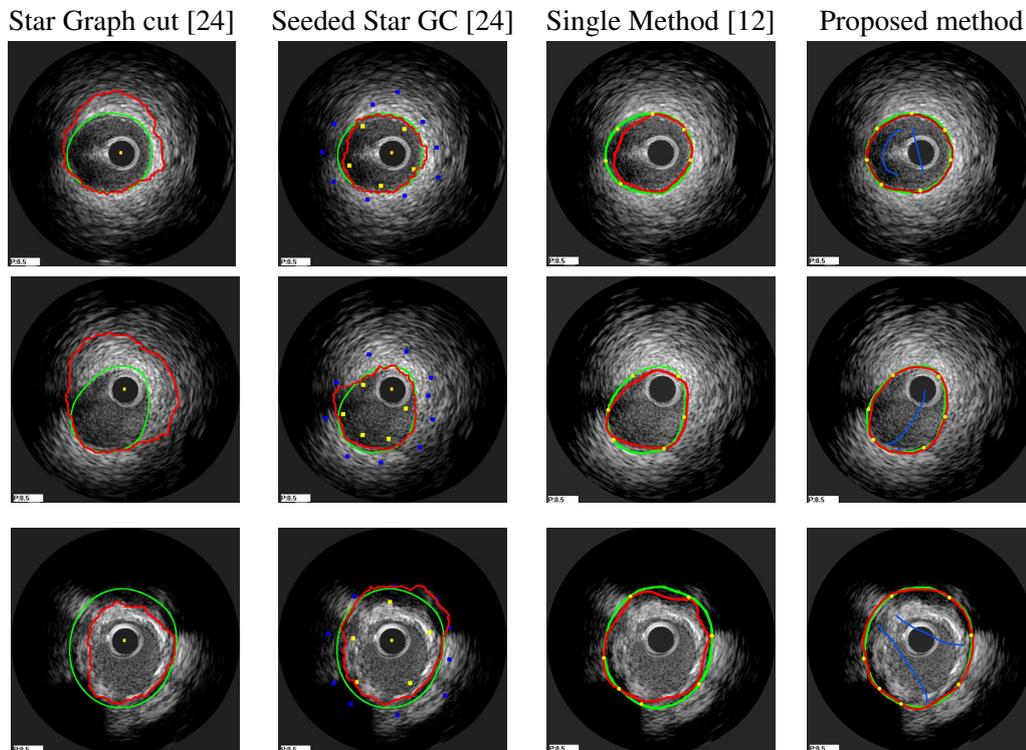
Figure 3.9: Comparison between ground-truth (green) and (from left to right) Star Graph Cut [24], Seeded Star Graph Cut [24], Single Method [12], Proposed Method (red). Note that the user control points used remain the same for both the single and proposed methods, but the seed points are region selection points in the seeded star method, not to be confused with edge based user points in the other methods.

3.3.2 OCT Image Segmentation

We also compared our proposed method to other methods in OCT images. OCT is another catheter based modality used in cardiology. In these images we are segmenting the lumenal border rather than the media-adventitia border which was targeted in IVUS. We chose this as OCT has far lower penetrance than IVUS images, but yields a much higher resolution view of the lumenal border. This makes it favourable for assessing stent placement and other surface lesions. Comparative examples are given in Fig. 3.12, and a further comparison between the single method and the proposed full method is shown in Fig. 3.13.

Star Graph cut [24]	Seeded Star GC [24]	Single Method [12]	Proposed method
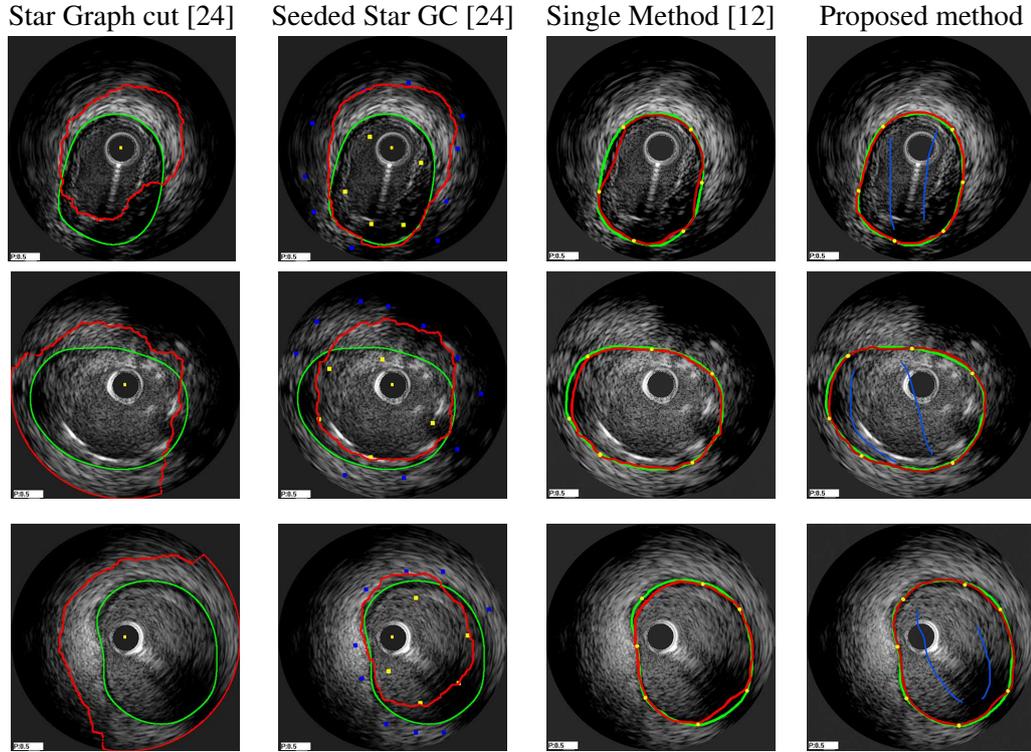
Figure 3.10: Comparison between ground-truth (green) and (from left to right) Star Graph Cut [24], Seeded Star Graph Cut [24], Single Method [12], Proposed Method (red). Note that the user control points used remain the same for both the single and proposed methods, but the seed points are region selection points in the seeded star method, not to be confused with edge based user points in the other methods.

3.3.3 Quantitative Results

In order to evaluate the results, we used a set of 248 IVUS images with ground-truth. They were taken from pull backs on 7 different patients. The ground truth labeling was obtained through manual labeling of the border of interest by an experienced third party. These were then segmented using the proposed method, which was compared to the method using only the edge detection and not the background/foreground weighting (single method) [12] and star graph cut (both with single and multiple seed points) [24]. Grab Cut segmentation was not used for the quantitative analysis, because as can be seen from Fig.3.14 it performs very poorly in this application. The quantitative analysis was also carried out on the results obtained from the OCT data. In this case we were segmenting the lumenal edge, which is quite well defined and regular, so all methods saw an improvement in accuracy. The results were obtained from a

Single method	Proposed method	Single method	Proposed method
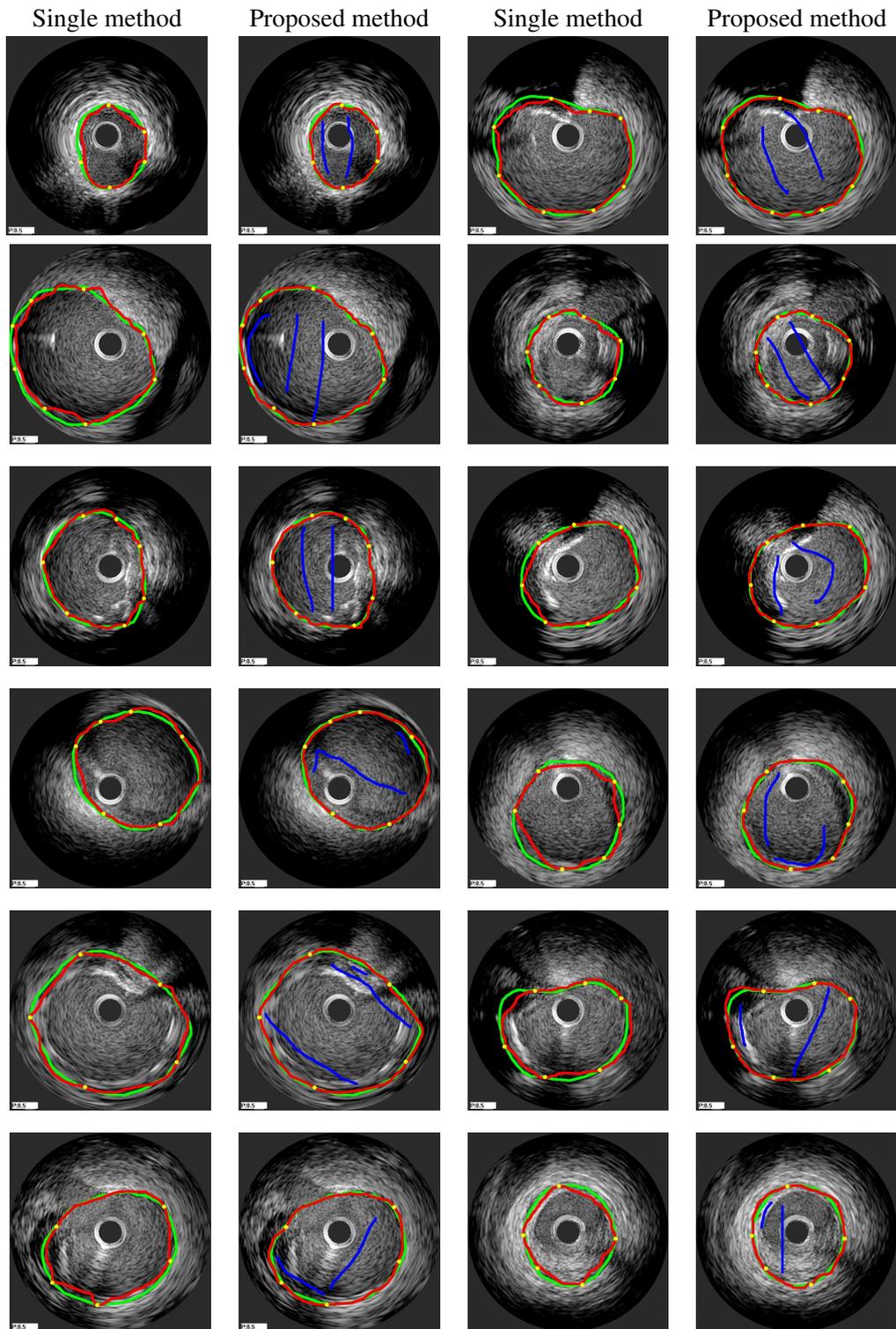
Figure 3.11: Comparison between the Single Method [12] and our proposed Method (red). The ground-truth in shown in green. Note that the user control points used remain the same for both methods.

65

Star Graph cut [24]	Seeded Star [24]	Single Method [12]	Proposed method
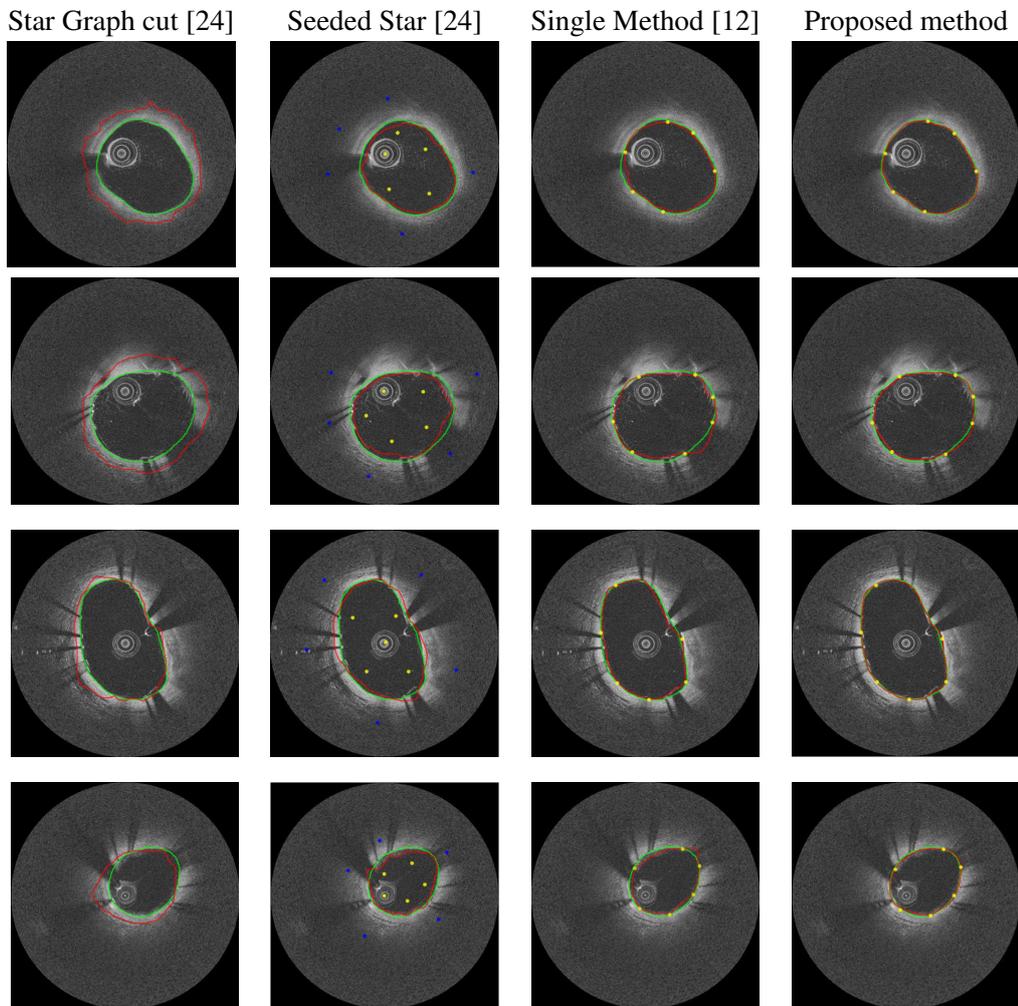
Figure 3.12: Comparison between ground-truth (green) and (from left to right) Star Graph Cut, Seeded Star Graph Cut, Single Method (no regional constraints), and Proposed Method (red) on OCT images to segment the lumen border. Control points remain the same in both the single and poposed method, but the seed points are region selection points in the seeded star method, and are not to be confused with edge based user points in the other methods

similar number of images as before (280) from 7 different pull-backs.

The quantitative comparison is based on a number of metrics, including Hausdorff distance, area overlap ratio, specificity, sensitivity, and accuracy. Table 4.1 shows the quantitative results obtained from the IVUS data, and Table 3.2 shows the OCT data. The star graph-cut method performed reasonably well with both foreground and background labeling. The implicit shape

Single method	Proposed method	Single method	Proposed method
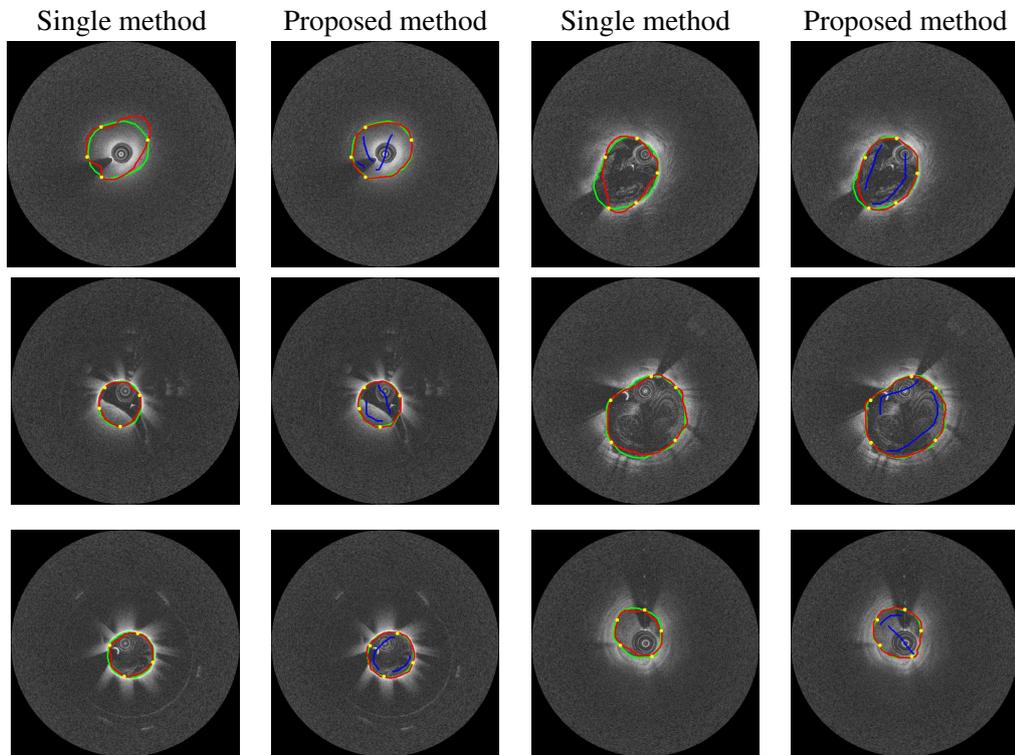
Figure 3.13: Comparison between the single method [12] and our proposed method (red) on OCT images. The ground-truth is shown in green. Note that the user control points used remain the same for both methods.
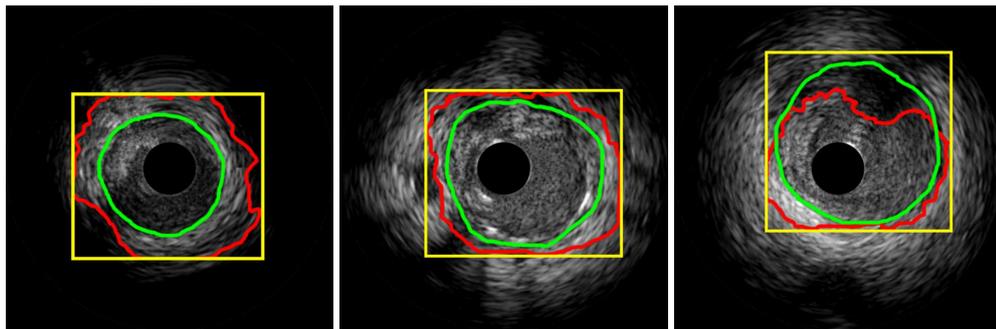
Figure 3.14: Typical Grab Cut Segmentation results (red) on IVUS images. Ground-truth is shown in green. It can be clearly seen that the obtained results are considerably out from the ground-truth.

Table 3.1: Quantitative comparison of the IVUS data-set. HD: Hausdorff Distance (pixels); AOR: Area Overlap Ratio (%); Spec: Specificity (%); Sens: Sensitivity (%), Acc: Accuracy (%). Bold font indicates best performance.

Method		HD	AOR	Spec	Sens	Acc
Star Graph-cut	Mean	60.57	81.22	89.22	89.86	89.29
	STD	15.64	1.00	12.00	1.00	6.52
Star Graph-cut with F/B labeling	Mean	43.81	86.05	90.39	**93.99**	92.17
	STD	23.89	9.00	9.00	5.00	5.65
Single method w/o F/B labeling	Mean	46.28	69.34	84.92	89.43	88.12
	STD	9.73	9.24	5.82	10.53	8.76
Proposed method with F/B labeling	Mean	**33.57**	**89.93**	**94.21**	93.14	**94.41**
	STD	5.35	9.16	3.88	5.37	7.67

Table 3.2: Quantitative comparison of the OCT data-set. HD: Hausdorff Distance (pixels); AOR: Area Overlap Ratio (%); Spec: Specificity (%); Sens: Sensitivity (%), Acc: Accuracy (%). Bold font indicates best performance.

Method		HD	AOR	Spec	Sens	Acc
Star Graph-cut	Mean	21.55	91.75	98.09	96.73	97.41
	STD	16.07	5.36	1.61	3.99	2.80
Single method w/o F/B labeling	mean	21.47	91.66	98.01	97.11	97.56
	STD	14.94	8.21	2.32	4.25	3.28
Proposed method with F/B labeling	Mean	**20.97**	**92.31**	**98.66**	**97.92**	**98.29**
	STD	15.84	4.99	1.76	3.60	2.68

prior in star graph construction proved useful constraint in segmenting media-adventitia border that conforms well to this shape constraint. Comparable performance was achieved for the proposed method without regional support. However, the full proposed method outperformed the rest. Several typical segmentation results are shown in Fig. 3.9.

To study the robustness of the proposed method, we carried out an initialization dependency test. We tested our method with 15 user points as initialization. We then randomly remove one user point each time for testing until we only have 2 points left for initialization. The overall results using 5 different metrics are shown in Fig. 3.15. The proposed method achieved good performance with just six user points. Considering in actual application where user input is far
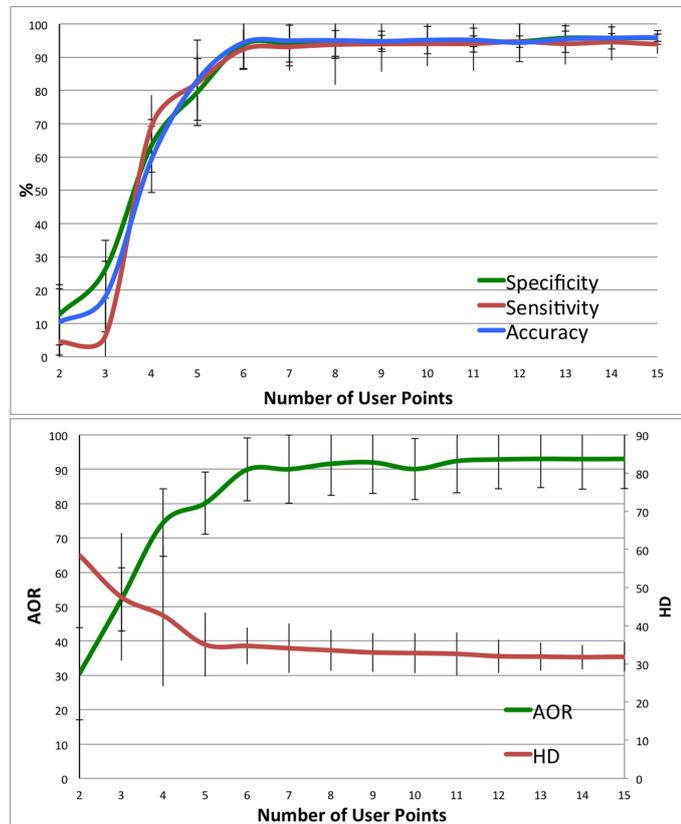
Figure 3.15: Initialization dependency test. This test was carried out using the IVUS data. The number of user points placed on the image was increased, and the effect of this on the observed metrics was recorded. It can be seen that only after a very few number of user points have been added, the accuracy reaches a plateau, which is an indication of good automation.

more experienced than this random process, even less points may be needed.

3.4   Further results

In order to demonstrate the versatility of the proposed method, we carried out segmentation of examples from other medical imaging modalities, as well as generic real world images. We believe that our method could equally be used in many other types of medical (or otherwise) image analysis, as its ability to segment open as well as closed curves effectively gives it a great deal of versatility. By showing the results of segmentation of a series of real world images, we can further show the versatility and robustness of this method.
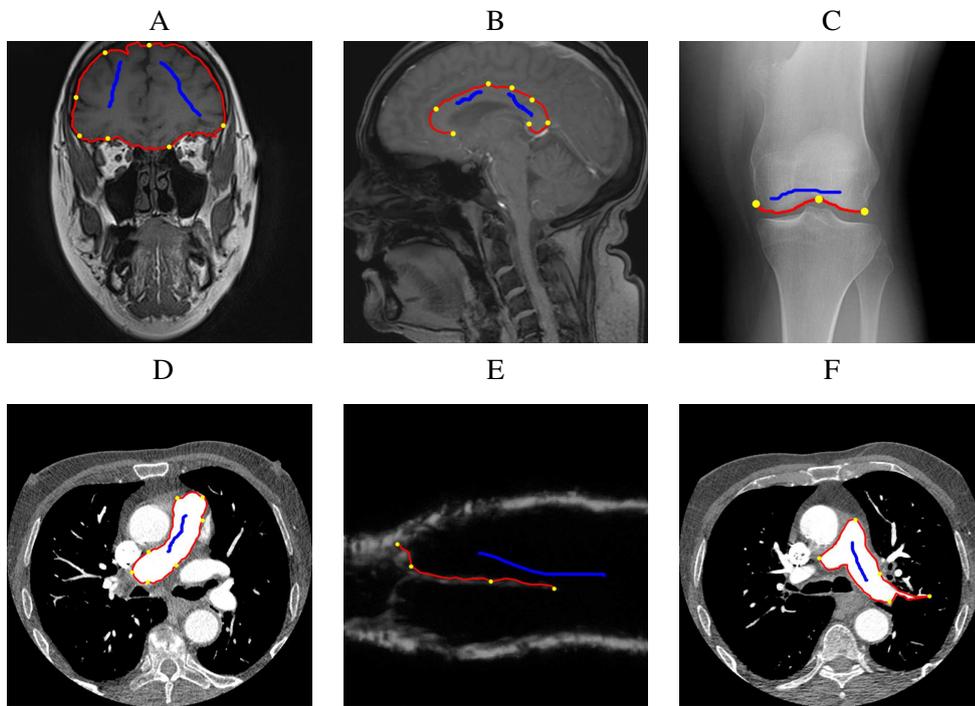
Figure 3.16: Examples of other medical image modalities. The red is the result obtained, the blue lines and the yellow circles the region selection and control points added respectively. (A) Segmentation of the Brain from an MRI, (B) Segmentation of Corpus Callosum from an MRI, (C) Segmentation of cartilage on knee joint from X-ray, (D,F) Segmentation of Aortic arch from CT, (E) Lymph Valve leaflet from Confocal microscopic image.

3.4.1 Other Medical Modalities

Using sample images from other studies, we show examples of how various features can be segmented out of medical images, see Fig. 3.16.

The ability of this method not to be limited to open or closed curve segmentation allows it to be used in many applications. In Fig. 3.16 a selection of different images are shown, with regions being selected, or open surfaces. The method copes well under both circumstances, and can easily be used to segment features of different types.

3.4.2 General Images

The proposed method was also evaluated using the Berkeley Image Database [61]. This data-set contains images of various types. The methods were used to perform a selection/segmentation

based on features in the image that would be a realistic segmentation to be carried out (for example, object selection, horizon selection etc.) The results from the proposed method were then compared to other available methods, namely $s - t$ graph cut [21], seeded star graph cut [24], GrabCut [25], and layered graph search with only point based interaction [12]. A selection of open and closed curve segmentations were used to demonstrate and compare the results.

The proposed method showed a very favorable segmentation performance compared to the methods we tested it against. The combination of a background/foreground separation, combined with the edge based approach gave the method a very robust segmentation, being able to segment an object of interest from an image where other (single methodology based) techniques found difficult to handle, for example if colours were closely related to background, or if there were many conflicting edges. This method utilizes super-pixels to speed up the segmentation in the same manner as with the medical images. However, do to the nature of real world images, the increase in speed is more significant (as there are more distinct regions that can be segmented out using the pre-segmentation step as shown in Fig. 3.19).

The advantage in being able to perform with open or closed curves is again shown in some of the images (Fig. Fig. 3.17), for example dividing the image on the horizon or segmenting figures that extend to the edge of the image.

Fig. 3.20 shows comparative results segmenting animal images from complex backgrounds and Fig. 3.21 provides several comparative results in segmenting images of humans from complex backgrounds. In both these sets, the addition of both edge and region based selections helps segment the complex image. The benefits of combining the two modalities can be scene even more in complicated natural images with patterns and textures (for example, in Fig. /ref-fig:camo where the lizard has a striking pattern, and is set against the rocky texture).

Fig. 3.22 demonstrates the advantages of the inclusion of regional data into the algorithm, in comparison to [12]. In some cases, where there are edges other than those required, without the regional selection, the segmentation can lose accuracy. By selecting the region specificity, in most cases these edges can be ignored without the requirement for more user points, which would increase the complexity of the graph.
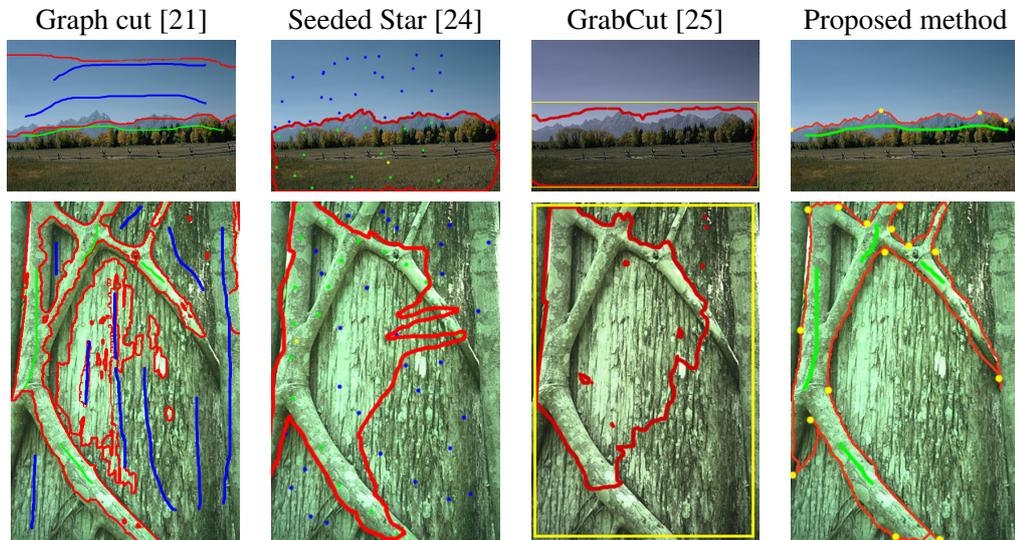
Figure 3.17: Examples of other real world images with an open segmentation. From left: Graph cut [21], Seeded Star Graph Cut [24], GrabCut [25], and proposed method. Red curve shows the segmentation result, blue for the background strokes, green for foreground strokes, and yellow for star point and the initial window of the Grabcut. User points in the proposed method should not be confused with the seed points in the seeded star method, as these are region selection points. The chosen images represent an open segmentation (the horizon above the mountain range) and a difficult segmentation (overlapping trees, with similar texture and large numbers of false edges).

Figure 3.18: Comparison Showing the benefits of the combined modality in complicated texture images. From left: Seeded Star Graph Cut [24], Single Method [12], and proposed method. Red curve shows the segmentation result, blue for the background strokes, green for foreground strokes, and yellow for star point. User points are the same between the single and proposed method, but the seed points are region selection points in the seeded star method, not to be confused with edge based user points in the other methods.
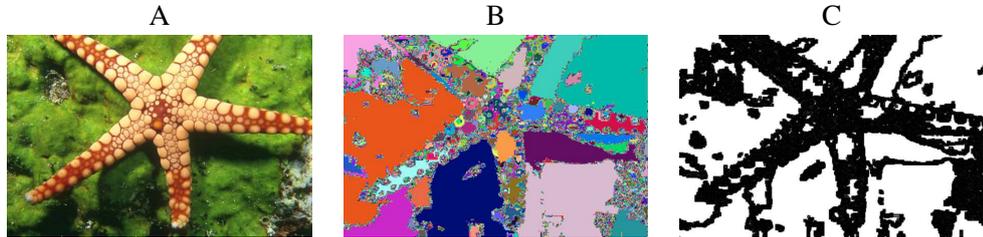
Figure 3.19: The use of super-pixel segmentation of real world images, to identify graph nodes. From left to right, (A) initial image, (B) super-pixel segmentation,(C) representation showing the nodes used in the graph (black) and those pruned (white).

Figure 3.20: Segmenting animals from complex scenes. From left: Graph cut [21], Seeded Star Graph Cut [24], GrabCut [25], and proposed method. Red curve shows the segmentation result, blue for the background strokes, green for foreground strokes, and yellow for star point and the initial window of the Grabcut.
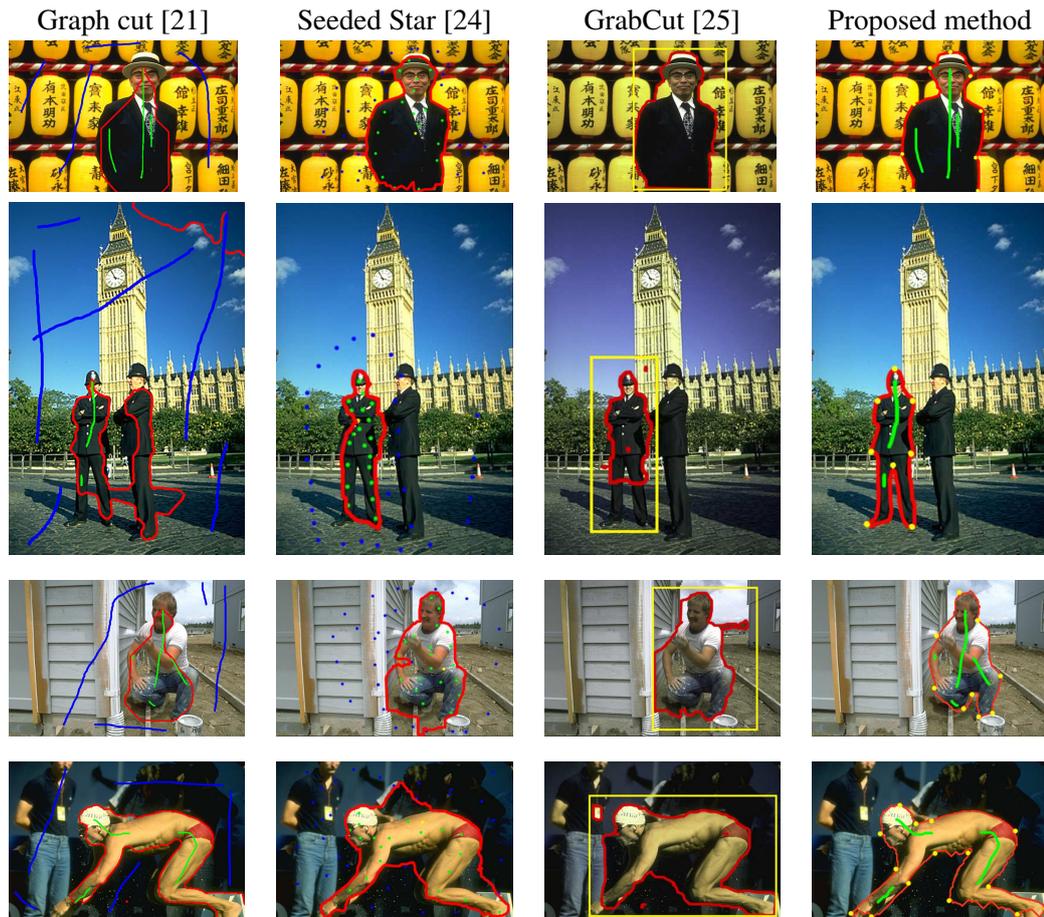
Figure 3.21: Segmenting human from complex scenes. From left: Graph cut [21], Seeded Star Graph Cut [24], GrabCut [25], and proposed method. Red curve shows the segmentation result, blue for the background strokes, green for foreground strokes, and yellow for star point and the initial window of the Grabcut.

Figure 3.22: Comparison between single method [12] and the proposed combined approach. The red curve shows the segmentation result, the yellow the user points (the same between both methods) and blue to region selection. Note the improved segmentation of the face (ignoring the strong false edge of helmet strap) in (A), and the difficult shoulder region in (C).

3.5 Conclusion

We presented an interactive segmentation technique which combines boundary based and region based object representations. We used this method to segment two sets of medical images (IVUS and OCT). We adopted a layered graph representation to simplify computation, and a super-pixel method to improve segmentation speed and efficiency. The proposed method was compared against a number of recent methods, and the standard graph cut techniques, showing improved versatility and better results. Where other methods had difficulty with certain image types, the combined approach was able to segment the desired information. We also show our method being used to segment different medical images, using open and closed objects, as well as generic real world images. This we believe shows how versatile the method is, and how easily it could be used for other applications. The method allows segmentation of both open and closed objects, so could be utilized not only in the segmentation of shapes such as vessel walls, organs etc. by to highlight linear features. We show an example of this, segmenting the end cartilage at knee joint (Fig. 3.16 (C)), but due to the nature of the method, it could be used to segment features such as fractures on bones, lesions and other such features that do not lend themselves easily to closed curve segmentation methods.

Chapter 4

3D Segmentation and Reconstruction of Vessel Borders

Contents

4.1   Introduction

In this chapter, we are concerned with providing a reliable segmentation method for detecting the inner and outer wall boundary in lymphe vessels. We will study images obtained in a slice-by-slice sequence through the vessel using confocal microscopy. The segmentation will be used to build a 3D structure representing the walls of the valve region of the target lymph vessels. This is achieved by the use of techniques involving optimal surface segmentation (OSS), and hidden Markov models (HMM) to segment the vessel walls individually. We will investigate different methods and compare the results both quantitatively and qualitatively. We will then demonstrate a method to simultaneously segment both boundaries using a novel s-Excess graph minimization solution incorporating additional arc weights for boundary thickness, and therefore allow constraints to be placed governing this. These constraint arcs

prevents overlapping of the segmentation results, and also further prevents the boundary result being "drawn away" by the valve region. Results of this method will be compared to that of the single segmentation.

In this chapter we will be investigating confocal images of lymphatic vessels. The images used show a section of the lymph containing the valve structure. As has previously been described in 2.4, lymph vessels are thin walled low pressure structures that rely on valves for unidirectional flow. It is the hope that by detailed segmentation and reconstruction of these regions it will be possible to obtain baseline data that can be compared with pathological states. This could then be used to help understand the underlying cause, which would help focus treatment and improve quality of life for sufferers.

Figure 4.2 shows an example image of a lymph vessel obtained using a confocal microscope. 2D segmentation is often carried out on confocal images, such as [199], but in our method we propose using object tracking to provide a method to segment the 3D volume. Object tracking is traditionally used in a variety of different applications[176, 200, 201, 202, 203] and now it is also becoming a useful tool in the medical field [204, 205, 206]. In object tracking, the "object" can be represented in various ways (points, geometric shape, and contours for example). Some, such as geometric shapes, are more suitable for representing rigid objects; whereas tracking the object contour can be used to segment a complex and nonrigid object.

4.1.1 3D Segmentation

In medical imaging, identifying 3D surfaces is of utmost importance. It is often the case that this is done by using a 2D method, as a great deal of work has been carried out in this area [207, 208, 45, 65, 44, 209] but when these methods are extended to segment a 3D volume, usually by looking at a series of slices, contextual information between the layers that make up the volume is often lost. There have been attempts to extend these methods into 3D [210, 211] but these have often proved to be computationally expensive. Another problem with utilizing 2D methods is that they can produce local minima. One method for 3D segmentation with a global minimum is Optimal Surface Segmentation(OSS) [212]. OSS provides a polynomial time method for simultaneously providing a global segmentation of a 3D volume with minimal or no user intervention, and in our method forms the basis of determining the initial segmentation, used to initialize the hidden Markov model (HMM).

4.1.2 Vessel Enhancing Diffusion

Vessel Enhancing Diffusion (or VED) [213] is a method to process vessel like structures to improve the image. VED has been shown to improve segmentation results of vessel structures [214, 213]. VED works within the scale space theory framework, using the initial image as the initial condition. By using a function of the Hessian, it is possible to directionally blur some parts of the image whilst preserving others. The Hessian eigensystem, $\mathcal{H}$, is used as it has a direct geometrical interpretation. This allows a "vesselness" filter to be created, and therefore the diffusion to be steered. Frangi [26] postulated the use of the Hessian eigensystem for this task, enhancing the vessel by searching for geometric structures that can be considered "tubular".

VED works by first analyzing the local characteristics of a particular image $\mathcal{I}$. By considering the Taylor expansion of this in the neighborhood of a point x_o:

$$\mathcal{I}(x_o + \delta x_o, s) \approx \mathcal{I}(x_o, s) + \delta x_o^T \nabla_{o,s} + \delta x_o^T \mathcal{H}_{o,s} \delta X_o \tag{4.1}$$

Where From (4.1) we can approximate the value of the image, with $\nabla_{o,s}$ representing the gradient vector at x_o in scale s and $\mathcal{H}_{o,s}$ representing the Hessian matrix with the same parameters. From the concepts of scale space theory, differentiation of this can be defined from the derivatives of the Gaussian:

$$\frac{\partial}{\partial x} \mathcal{I}(x, s) = s^\gamma \mathcal{I}(x) \times \frac{\partial}{\partial x} G(x, s) \tag{4.2}$$

whilst defining the $\mathcal{D}$-dimensional Gaussian as:

$$G(x, s) = \frac{1}{\sqrt{(2\pi s^2)}^D} e^{-\frac{||x||^2}{2s^2}} \tag{4.3}$$

The γ term is presented in the work by [155], defining the collection of normalized derivatives obtained. Taking the second derivative of the Gaussian kernel we can generate a probe kernel to measure changes in contrast between regions inside and outside the scale range $\pm s$ in various directions.

The final term in equation (4.1) is used to give the second order directional derivative.
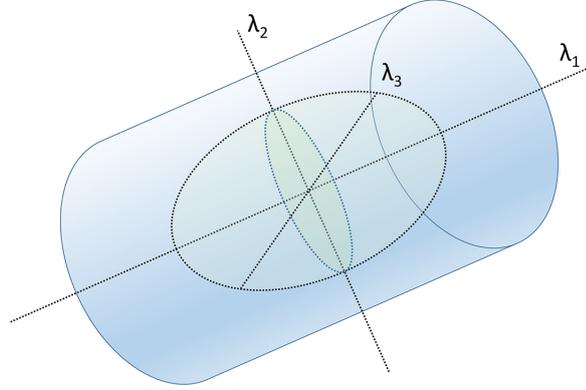
Figure 4.1: Representation of the second order ellipsoids. Adapted from [26]

$$\delta x_o^T \mathcal{H}_{o,s} \delta x_o = (\frac{\partial}{\partial \delta x_o})(\frac{\partial}{\partial \delta x_o})\mathcal{I}(x_o, s) \tag{4.4}$$

By utilizing this eigenvalue analysis of the Hessian, it is possible to extract the principle directions of the local second order structure. This gives us the direction of the smallest curvature, which corresponds to along the vessel. In this way, the method removes the necessity to apply several filters in multiple orientations to the image, dramatically reducing the computational complexity of the solution. From this, in the case of a bright vessel on a dark background (such as is the case in our images) it follows that the ordering of the eigenvalues $|\lambda_1| \leq |\lambda_2| \leq |\lambda_3|$, gives the direction along the vessel $vess_1$ when $|\lambda_1| \approx 0$ and $|\lambda_1| \leq |\lambda_2| \approx |\lambda_3|$ see Fig. 4.1.

$$Vess_o(s) = \begin{cases} 0 & if\, \lambda_2 > 0\, or\, \lambda_3 > 0 \\ (1 - e^{-\frac{\mathcal{A}^2}{2\alpha^2}}).e^{-\frac{\mathcal{B}^2}{2\beta^2}}.(1 - e^{-\frac{\mathcal{S}^2}{2\lambda^2}}) & otherwise \end{cases} \tag{4.5}$$

where:

$$\mathcal{A} = \frac{|\lambda_2|}{|\lambda_3|} \tag{4.6}$$

$$\mathcal{B} = \frac{|\lambda_1|}{\sqrt{|\lambda_2 \lambda_3|}} \tag{4.7}$$

$$\mathcal{S} = \sqrt{\lambda_1^2 + \lambda_2^2 + \lambda_3^2} \tag{4.8}$$

The combination gives us the following formulation (Eq. (4.5)) for the measure of vesselness.
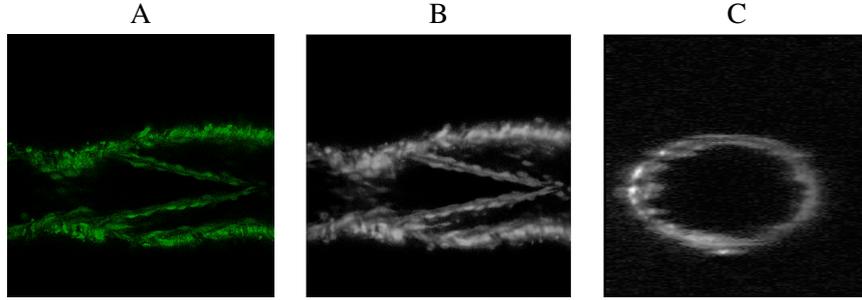
Figure 4.2: (A) shows original image, (B) shows the image after VED has been applied, and (C) shows the image after transformation. It should be noticed that the quality of the image is improved from (A) to (B), with less gaps in the visible image, although there are still some gaps present int the image.

4.2 Proposed Method - Single Border Segmentation

In our proposed method, we aim to segment both borders of the vessel wall individually. In order to do this, we first apply preprocessing steps to the image. These involve applying Vessel Enhancing Diffusion (VED) to the image to reduce the noise and help lessen the detrimental effect of the occluded areas. The images were then transformed to cross sections, aligned and scaled to uniform dimensions to aid the training. The stages of pre-processing are shown in Figure 4.2. Once the images were prepared, OSS was carried out, to be used as the initial segmentation for the HMM segmentation stage.

4.2.1 Graph Construction

The volumetric image we wish to segment, now comprises of a series of slices through the lymph vessel. In order to find the optimal surface, we transform these from Cartesian to Polar coordinates. Each slice representing the $(\mathbf{x}, \mathbf{z})$ plane, and position of that slice in the stack gives the $\mathbf{y}$ axis, as if looking at a topographical landscape feature. Our image can therefore be represented as a 3D matrix $\mathcal{I}_{3D}(x, y, z)$. The size in any given dimension can be represented as X, Y and Z. The surface can thusly be defined:

$$\mathcal{I} : (x,y) \rightarrow \mathcal{I}(x,y), where :$$

$$x \in \mathbf{x} = \{0,...,X-1\},$$

$$y \in \mathbf{y} = \{0,...,Y-1\}, and \tag{4.9}$$

$$\mathcal{I}(x,y) \in \mathbf{z} = \{0,...,Z-1\}$$

In this way, any given surface $\mathcal{I}$ intersects with exactly one voxel of each *column* parallel to the $\mathbf{z}$-axis. We can therefore construct a node-weighted graph $\mathcal{G} = (\mathcal{V}, \mathcal{E})$ can be constructed for $\mathcal{I}$. In the graph $\mathcal{G}$ each voxel v is connected to column-wise with its bottom neighbor, with its neighboring voxels in the subsequent layer (with Δ deflection), and with neighboring columns (with δ deflection) with ∞ cost; the final voxel in each column has a bidirectional arc to its neighbor.

4.2.2   Cost Term

For every node $\mathcal{V}(x,y,z) \in \mathcal{V}$ in the graph represents one voxel in $\mathcal{I}(x,y,z) \in \mathcal{I}_{3D}$ with a given weight $w(x,y,z)$, representing the probability of that pixel being selected. This weight, w, can be derived from a steerable edge based filter applied to the polar transformed image, which can be seen in Fig. 4.3 and Fig.4.4. The steerable filter is a linear combination of differentially orientated instances of a base filter. A set of n order derivatives of Gaussian filters $G_n(x,y)$ in different orientations are used to highlight edge features along a border. These can be defined as follows:

$$G_n^\theta(x,y) = \sum_{j=1}^{M} k_j(\theta) G_n^\theta(x,y) \tag{4.10}$$

where $\mathcal{G}_n^\theta(x,y)$ is the rotated version of $\mathcal{G}_n(x,y)$ at θ orientation, and $k_j, 1 \leq j \leq M$ are interpolation functions. Due to the derivatives in the direction being invariant, regardless of rotation, steerable filters are effective at highlighting orientated structures, in this case the edges, than other filter types, especially in situations such as in the lymph images where there is a lot of noise [215]. The cost of any voxel v can be given as $w_v = g(v)$ where g is the cost to assign that pixel to object or background nased on the steerable filter. This allows us to formulate the problem as a Min Cut/Max Flow problem, cutting from source s to sink t. The total energy cost $\mathcal{E}$ for every voxel in the $s - t$ cut can therefore be represented by:

$$\mathcal{E} = \sum_{v \in V} w(v) \tag{4.11}$$
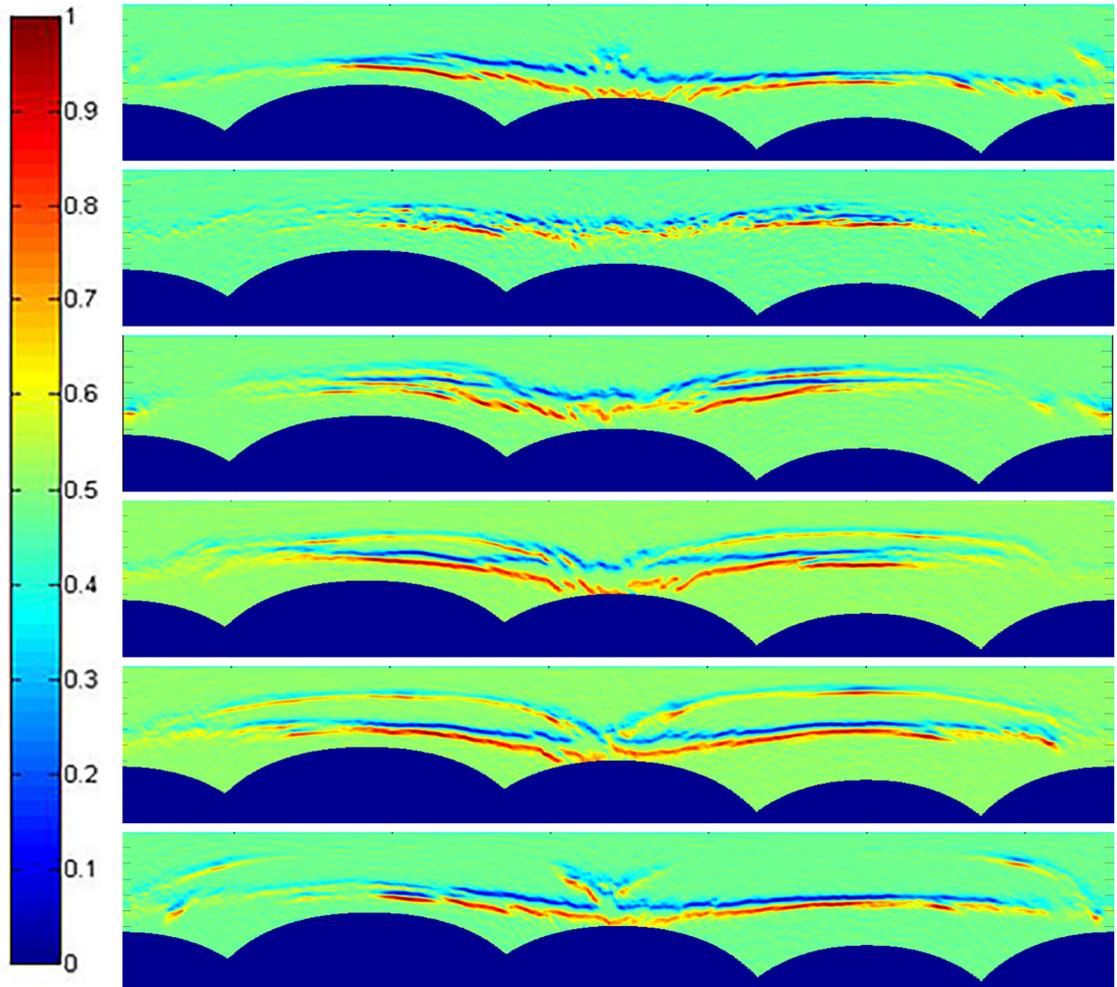
Figure 4.3: Figure shows a series of pseudo-color images illustrating the steerable filter showing the inner wall boundary. To the left is a scale bar, illustrating the cost, and to the right of that are six different examples. Note the inner wall is the upper surface in the image, and the valve can be seen as the feint top-most object.
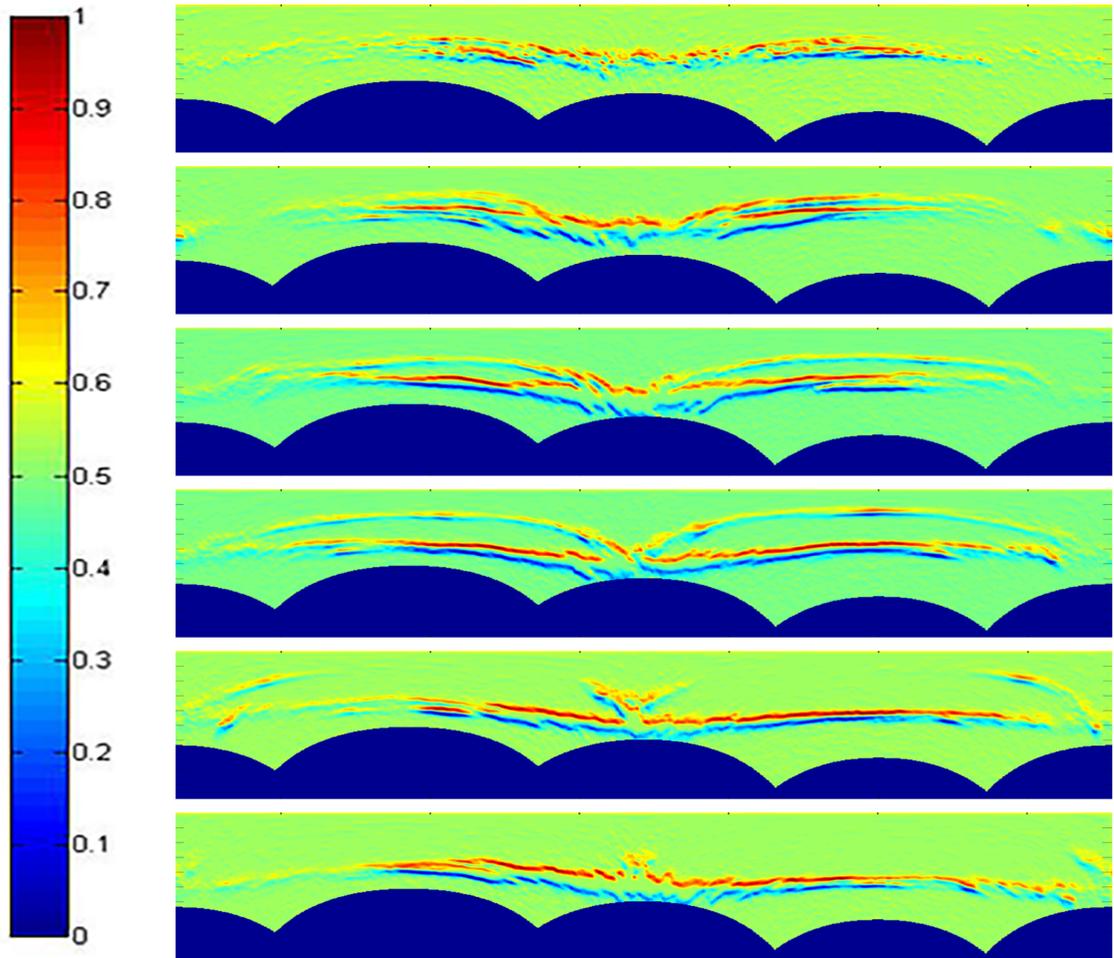
Figure 4.4: Figure shows a series of pseudo-color images illustrating the steerable filter showing the outer wall boundary. To the left is a scale bar, illustrating the cost, and to the right of that are six different examples. The outer wall is the lowermost border in the images.
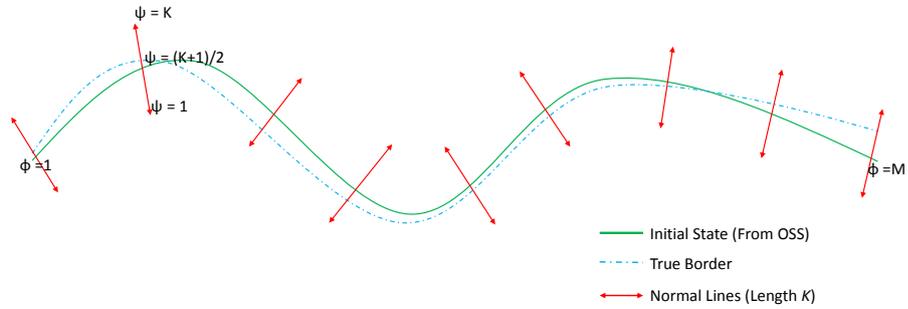
Figure 4.5: Schematic representation of the use of RBF centers to construct the HMM using the OSS results as the initial state

4.2.3 HMM Segmentation

The results from the OSS (shown in Fig. 4.6 are used to set the initial state of our HMM. We trained the HMM with 1024 image slices from 2 confocal samples, using the unraveled images that have been transformed into polar coordinates for the voxels in our image. We use a user selected "center" point to perform the transformation, this is stored in order to return to cartesian after the boundary has been found. It is computationally very expensive to track all the border points in the polar coordinates, but in our case, this is unnecessary as a result of the polar transformation (creating a "curve" shape for our boundary). We use an RBF to approximate the border of interest, with the hidden states of the HMM referring to the RBF centers. The border was evenly sampled into M points and from each of these a line segment is extended either side, perpendicular to the border's tangent at that point, with line segments each having K points, with the index of the RBF centers denoted $\phi = 1, ..., M$ and the index along each of these normal lines being denotes as $\psi = 1, ..., K$ where K is an odd integer. Our initial RBF centers are derived from the result of the OSS, and are located at the centre of the normal line $\psi = (K+1)/2$. The steerable filter is used to determine the edge, in this case the vessel wall, and the emission probability is computed using Gaussian distributions calculated from the image observation. Our transmission probability is learned from the training set. See Fig. 4.5 for a schematic of this.

85

In our proposed HMM, we denote all possible sequences of hidden states as $\mathcal{Q} = \{q\}$ where $q = \{q_1, ..., q_\phi, ..., q_M\}$ is one of the possible state sequences (corresponding to possible RBF center locations) and q_ϕ is the state being on the normal at ϕ. The observations O of the HMM are extracted from the normal lines as such that $O = \{o_1, ..., o_\phi, ..., o_M\}$, and the HMM is specified by the probability measures $\lambda = (A, B, \pi)$. Let $O_\phi = \{o_{\phi,1}, ..., o_{\phi,\psi}, ..., o_{\phi,K}\}$ be the set of features along the normal ϕ and $o_{\phi,\psi}$ be a feature extracted from point ψ on the line, thusly $P(o_{\phi,\psi} \mid FG)$ and $P(o_{\phi,\psi} \mid BG)$ are the probabilities of the feature being foreground or background respectively. The state-emission probability can therefore be defined as:

$$P(O_\phi \mid q_\phi) \propto P(o_{\phi,\psi} \mid FG) \prod_{\psi \neq q_\phi} P(o_{\phi,\psi} \mid BG) \tag{4.12}$$

We then use the Viterbi algorithm [216], which is a modification of the Baum-Welch algorithm. The Baum-Welch algorithm uses Expectation-Maximization method to compute the maximum likelihood in the HMM the probability of moving from a state i at normal ϕ to new state j at normal $\phi + 1$, where $1 \leq \phi \leq M$ and $1 \leq i, j \leq K$ between states q with two normals ϕ and $\phi + 1$ as:

$$\xi_\phi(i, j) = P(q_\phi = i, q_{\phi+1} = j \mid O, \lambda) \tag{4.13}$$

In the Viterbi algorithm, the sequence of states $q*$ can be efficiently found given the image observation O_t and the HMM model λ:

$$q* = \underset{q \in Q}{\mathrm{argmax}} P(q \mid O_t, \lambda). \tag{4.14}$$

Fig. 4.6 and Fig. 4.7 show examples of the normal lines being applied to the initial data for the inner and outer edges respectively.

4.3 Results for Single Wall Segmentation

The results were drawn from 3,072 slices from 6 different experiments, separate from those used in the training set. Fig. 4.8 and Fig. 4.9 show the results obtained for segmentation of the inner and outer walls respectively, before conversion back from polar to Cartesian coordinates. The results show the improvement of the HMM method (blue) over the OSS alone (red). The results for the outer wall are significantly better than those for the inner. In both methods (though less so in the proposed method), this is because the valve extends from the wall, into
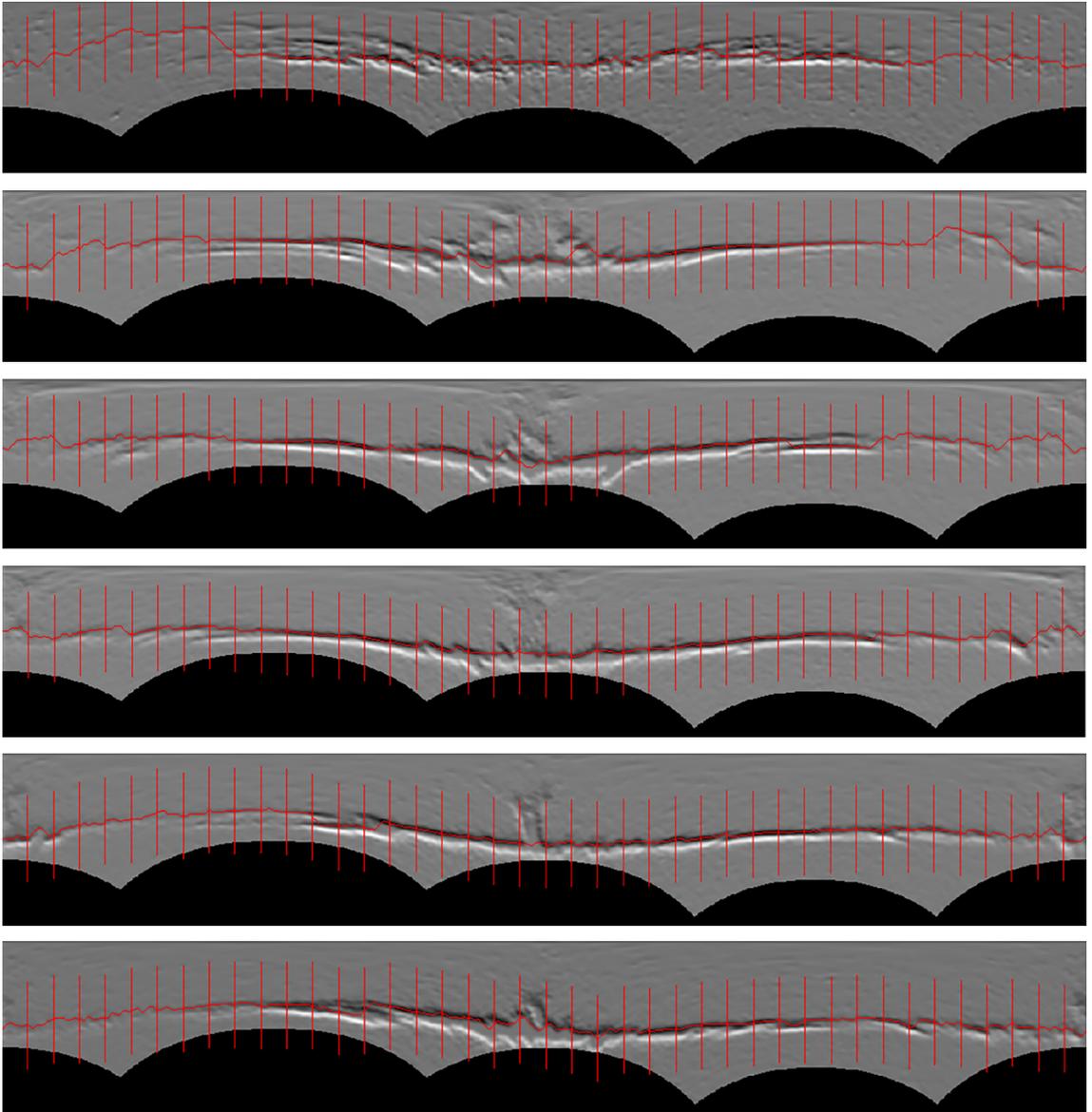
Figure 4.6: Figure shows the position of the normal lines relative to the initial state for the inner boundary wall.
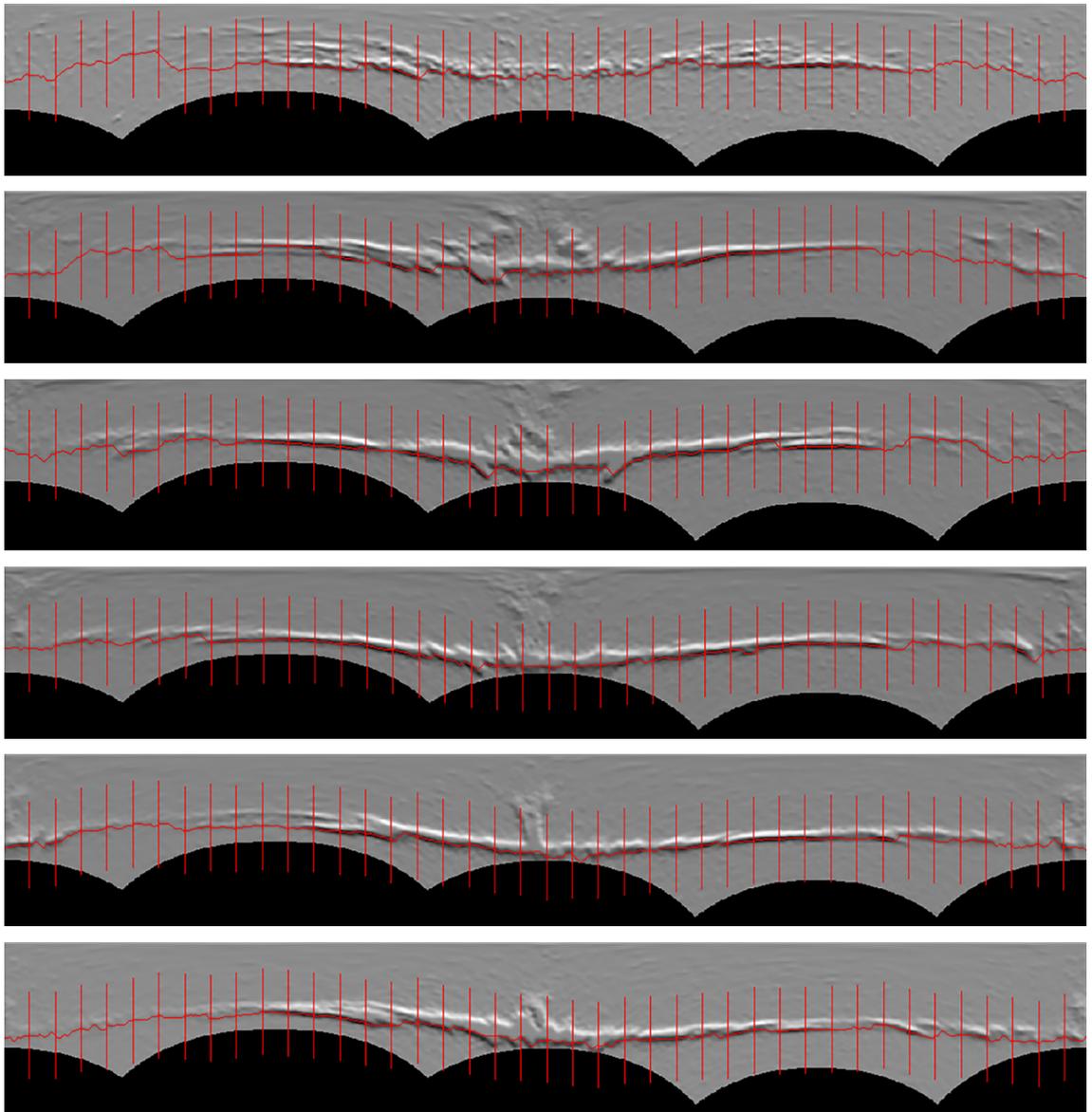
Figure 4.7: Figure shows the position of the normal lines relative to the initial state for the outer boundary wall.
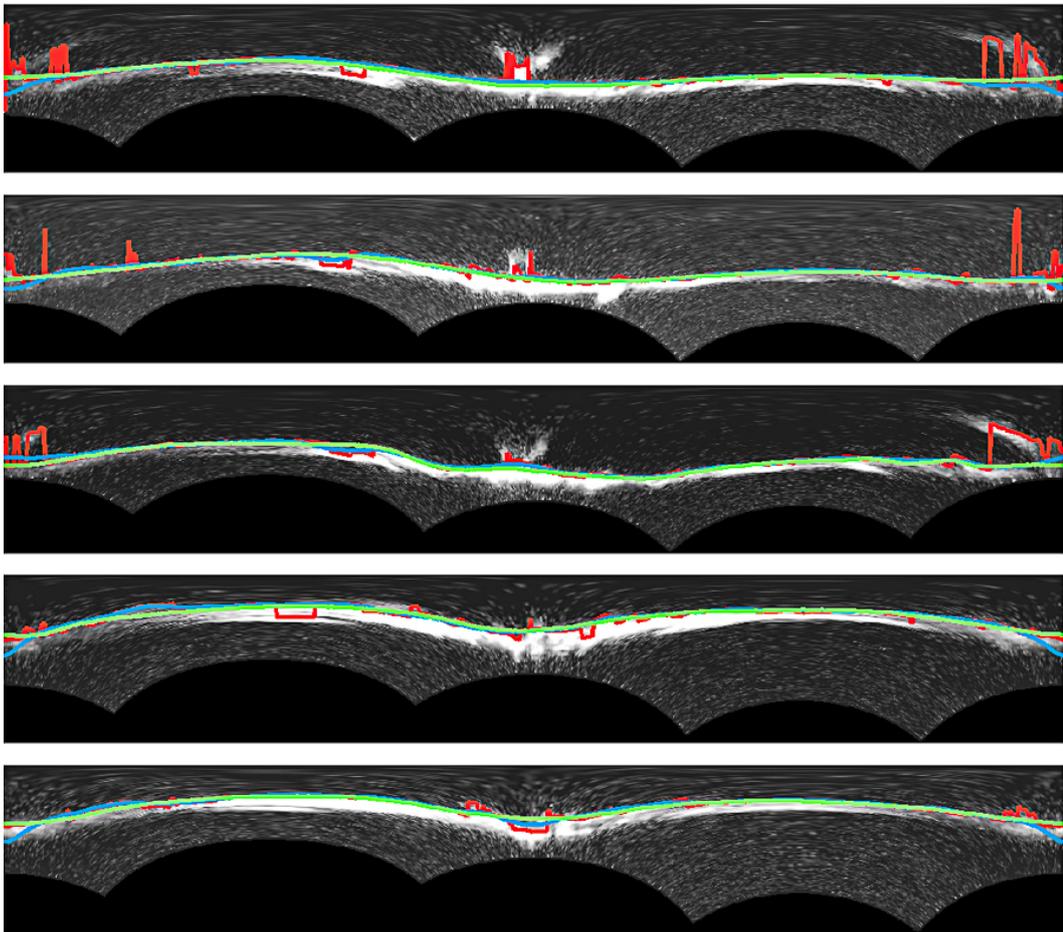
Figure 4.8: Results for the inner wall of the lymph vessel. Light blue is the proposed method, red OSS only and green the ground truth

the lumen, this makes it hard to even manually label the slices where the valve originates. Our proposed method shows a significant improvement in these regions, as well as those with very poor contrast or missing areas. because the training helps the segmentation to cope with interference and gaps in the edge.

Table 4.1 provides a quantitative comparison between the proposed method and the results obtained using OSS alone. The proposed method clearly benefited from HMM and produced consistently better results.

In Fig. 4.10 and Fig. 4.11, we show some typical results of segmentation of both inner and outer walls of the vessel using the proposed method. It can be seen that by combining optimal
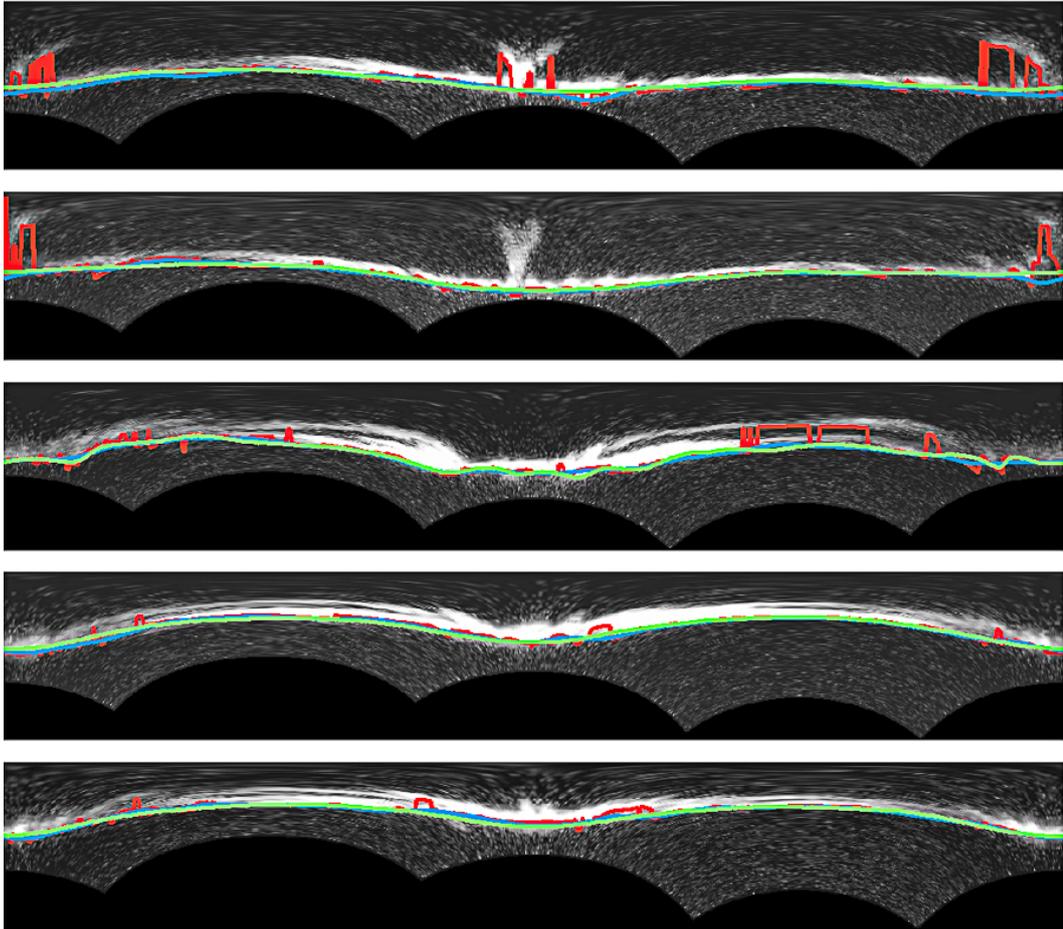
Figure 4.9: Results for the outer wall of the lymph vessel. Light blue is the proposed method, red OSS only and green the ground truth

surface segmentation with HMM, a coherent and smooth segmentation of both boundaries is achieved in the presence of noise and frequent weak edges. The segmentation is not confused by the valve regions, however the two walls, with no arcs between them do come very close, and in some cases can cross over (as shown later in Fig. 4.15). This is undesirable, even though the quantitative results are good.

The end result is a reconstructed vessel shape. This is shown in Fig. 4.12. It can be seen that the segmentation method gives a good rendition of the vessel shape from the confocal slices. There are some areas though where the segmentation does not match the desired (and biologically possible) ground truth. In examples with little to no definition for large areas of
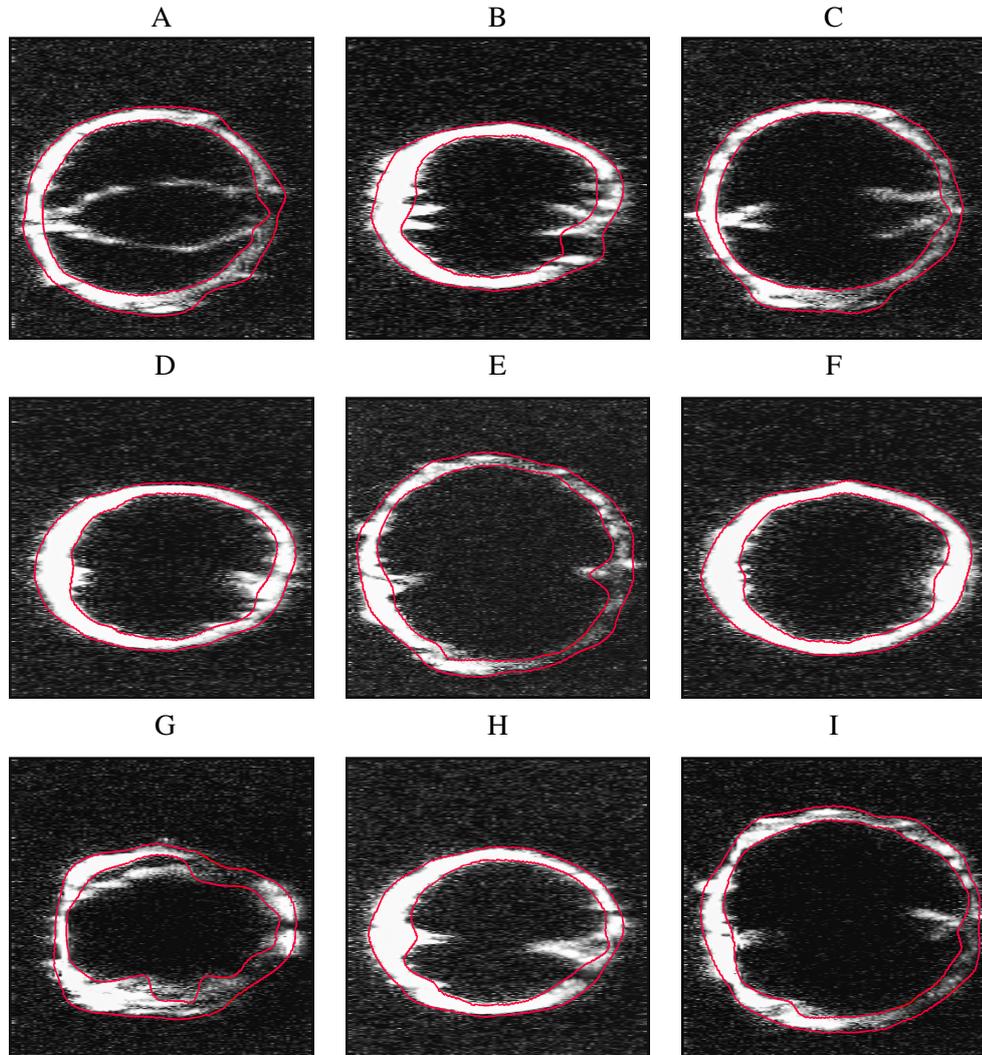
Figure 4.10: Results showing the segmented walls (red) on the wrapped images. Note that despite the strong features resulting from the valve/wall interface, the segmentation preferentially tracks the wall in most cases especially (A), (B), and (C). Note that in (G) it is also not confused by the valve being close to the wall.
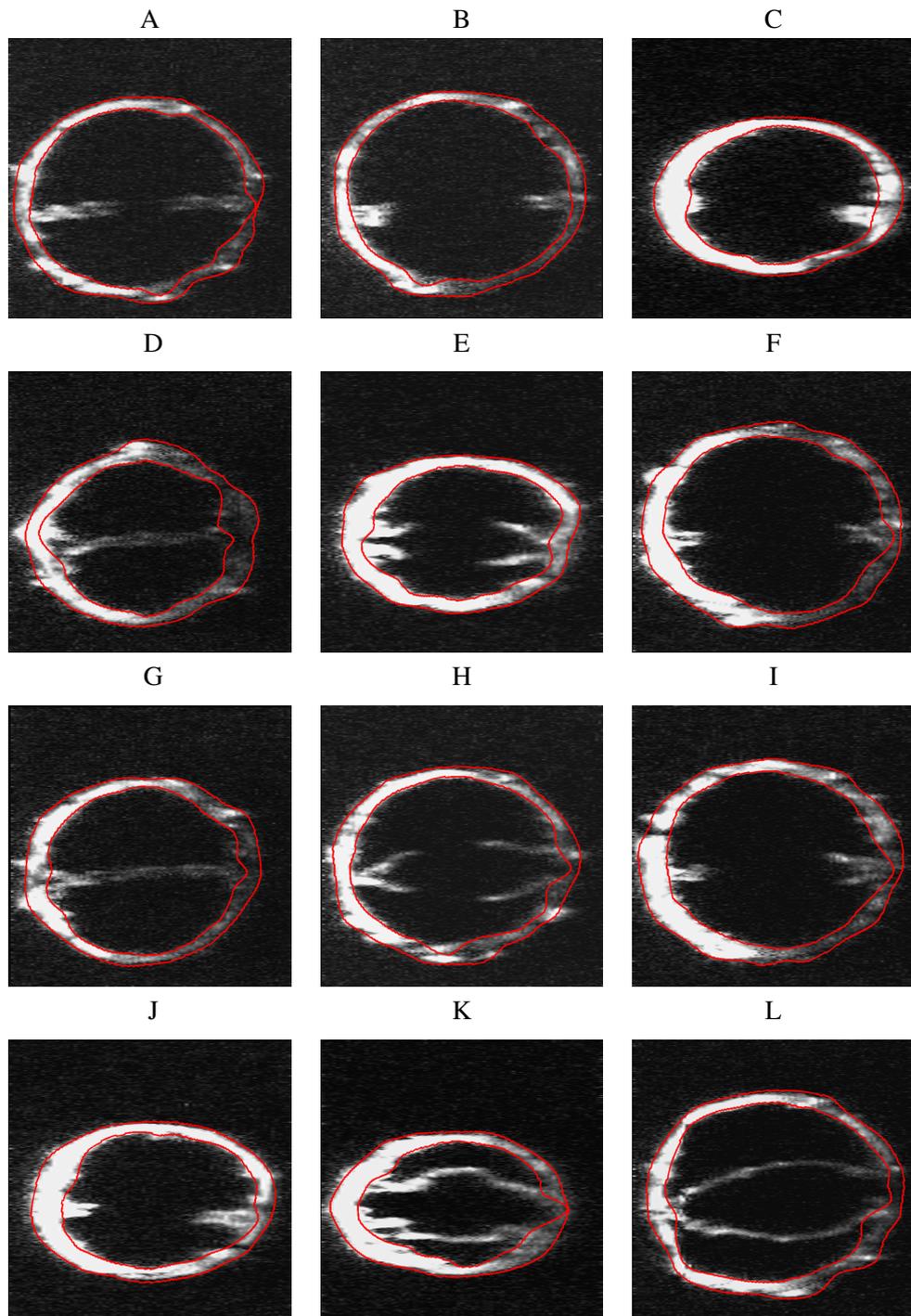
Figure 4.11: More results showing the segmented walls (red) on the wrapped images. Note that the segmentation follows the wall instead of getting confused by the valve features ((A), (B), and (C) for example), however, where image quality is poor (gaps and lack of features, such as (J)) then some confusion occurs.

Table 4.1: Quantitative comparison of the Lymph data-set. HD: Hausdorff Distance (pixels); AMD: Absolute Mean Difference (pixels) AO: Area Overlap(%); Spec: Specificity (%); Sens: Sensitivity (%). Bold font indicates best performance.

Method		HD	AMD	Spec	Sens	AO
Outer Wall -OSS	Mean	51.0330	7.0631	97.34	91.15	90.06
	STD	22.59	3.55	0.62	5.56	5.63
Outer Wall -Proposed method	Mean	**23.31**	**4.67**	**99.16**	**94.80**	**93.29**
	STD	2.88	10.14	0.69	4.6	4.81
Inner Wall -OSS	Mean	55.52	7.06	96.18	92.73	91.71
	STD	3.17	13.57	0.81	4.28	4.07
Inner Wall -Proposed method	Mean	**13.72**	**3.31**	**98.49**	**98.00**	**96.11**
	STD	5.35	9.16	3.88	5.37	7.67

the surface, it sometime happens that the two segmented borders merge. This cannot happen *in vivo* and so our segmentation needs to be expanded to prevent this eventuality. In order to do this, we will re-evaluate the methods used for segmentation, in order to allow for control arcs to be added governing the distance between the two borders.

4.4   Simultaneous Segmentation of Borders

The logical next stage of this work was to implement a method to segment both borders simultaneously. In order to achieve this, we transform the segmentation problem one of minimization of s-excess graph. Each node in the graph corresponds to one state, and the weight for each node is defined using its emission probability, and the inter-relation between neighboring nodes is defined using the transition probability. Using this formulation, an optimal solution can be found in polynomial time using the s-t cut algorithm.

4.4.1   Minimum s-Excess Graph Construction and Optimisation

The minimum s-Excess graph is a relaxed variation of the minimum closure graph [217]. In our simultaneous border segmentation method, each hidden state on the normal line corresponds to a node in the graph, and the cost of which is inversely proportional to its emission probability. The transition probability is used to define the inter-columns arc cost. The minimization of this s-excess graph can be effectively solved using graph cut in polynomial time.

Figure 4.12: Results showing the reconstruction of the vessel from the segmented walls. Inner wall is represented in yellow and outer wall in red. Note that the segmentation provides good results for most of the structure but in a region towards the lower portion, there is an anomaly. This is caused by insufficient feature data in that region, causing boundaries to overlap.

Solving the minimization of closure graph and s-Excess problems has been applied to image segmentation problems [218, 212, 219, 217]. In Song *et al* [218] the authors utilise prior information, in the form of prior shapes, through encoding them as a set of convex functions. These are defined between every pair of adjacent columns in the image. We utilise a similar, column based approach, however we formulate the problem as a tracking one. In our formulation, we track the problem across consecutive frames, defining the pair-wise cost based on the transition probability, which is learned from our training data (the same set of training data is used in these experiments as in the previous ones), and treating the problem as a stochastic process.

As described by Dorit [217], the s-Excess graph is a relaxation of the closure set problem. A closed set can be defined as a subset of a given graph, where all successors of any node in the set are also taken into the set. In the s-excess variation, the successors may not be contained in the set, but will have a cost equal to the edge cost heading to such successors.

Given a directed graph $\mathcal{G}(V, E)$, each node $v \in V$ is assigned a certain weight $w(v)$ and each edge $e \in E$ will have a positive cost. The aim of the s-excess problem is therefore to obtain a subset of the graph nodes $S \subset V$ where the total cost of the nodes and the cost of separating them from the rest of the graph, $S' = (V - S)$ is minimised. The HMM, is formulated as before, using M RBF centers ($m = 1, ..., M$), evenly spread across the surface line (obtained from the initial state). Each of these having a normal line ($k = 1, ..., K$) as described above (see 4.2.3 and Fig. 4.5).

$$\mathcal{E} = \sum_{v \in S} w(v) + \sum_{\substack{(u,v) \in E \\ u \in S, v \in S'}} c(u, v) \qquad (4.15)$$

For each of the borders of interest $\mathcal{S}$ in our image, we create a graph $G_{\mathcal{S}}$ of $M \times K$ nodes, each node corresponding to a hidden state, and each normal line K representing a column chain. In our graph construction we have three distinct types of arc present connecting our nodes. These are intra-chain (connecting the nodes within a chain), inter-chain (connecting neighboring chains), and intra-border used to define a minimum and maximum distance between the two borders). Intra-chain arcs occur along each chain $Ch(m, k)$ in our image. For every node $v(m, k)$ in our image (where $k > 1$) has a directed arc to the next node in the chain $v(m, k - 1)$ with an assigned weight of $+\infty$. This ensures that the desired border will only insect with each chain (representing the normal line) once only. Inter-chain arcs are defined for any given pair of chains $Ch(m_1, k_1)$ and $Ch(m_2, k_2)$. We establish a set of directed arcs to link every node $v(m_1, k_1)$ (on $Ch(m_1, k_1)$) with nodes $v(m_2, k_2')$ in the adjacent chain $Ch(m_2, k_2)$, where $1 \leq k_2' \leq k_1$. Likewise, we connect each node $v(m_2, k_2)$ on $Ch(m_2, k_2)$ to $v(m_1, k_1')$ on $Ch(m_1, k_1)$, where $1 \leq k_1' \leq k_2$. As we have represented each hidden state with a node on the graph, the costs for the arcs between these can be defined by the HMM transition matrix $A(k_1, k_2)$.

The last row of each graph need to be connected in order to for the basis of a closed graph. As the images we use are unraveled into polar coordinates, we also need to ensure the first and last chains are connected to each other via the same method as the inter-chain arcs.

95

We use the inter-border arcs to define a range for the thickness of the border, and to ensure the borders never cross each other. These constraints are defined so that:

$$\underline{\Delta} \leq \mathcal{S}_1 - \mathcal{S}_2 \leq \overline{\Delta}. \tag{4.16}$$

For any given node $v_1(m,\hat{k})$ in $Ch_1(m,k) \in G_1$ there is a direct arc defined connecting $v_1(m,\hat{k})$ with $v_2(m,\hat{k}-\overline{\Delta})$, where $\hat{k} \geq \overline{\Delta}$ and $v_2 \in Ch_2(m,k)$. $\hat{k}$ corresponds to the index in the image domain $X \times Y$ of k in the graph domain. Likewise nodes $v_2(m,\hat{k})$ in $Ch_2(m,k) \in G_2$ are connected to $v_1(m,\hat{k}+\underline{\Delta})$ where $\hat{k} < Y - \underline{\Delta}$ and $v_1 \in Ch_1(m,k)$. The cost for these arcs is set to $+\infty$.

The cost for each node is calculated from the emission probability at that node. This is done according to:

$$C(m,k) = -\log(P(o_{m,k}|q_{m,k})). \tag{4.17}$$

This cost has an inverse correlation with the likelihood that our border of interest passes through the node (m,k). Thus the weight of any given node $w(m,k)$ on our directed graph can be defined as:

$$w(m,k) = C(m,k) - C(m,k-1). \tag{4.18}$$

The exception to this is the bottom of the chain, i.e.

$$w(m,1) = C(m,1). \tag{4.19}$$

Solving this minimum s-excess problem can be seen as an equivalent to solving a standard $s-t$ cut algorithm [220, 217]. We therefore use the standard $s-t$ cut algorithm [221] to find the minimum closed set in polynomial time, with a cost of the cut representing the total number of edge costs separating the graph into the source (i.e. the minimum s-excess graph) and the sink sets.

4.4.2 Minimum s-Excess Segmentation Results

A sample of our results obtained by utilizing the s-excess method and adding inter-border arcs to fix minimum and maximum thickness are shown in Fig. 4.13 and Fig. 4.14, with quantitive results shown in Table 4.2 (with the results from the previous section method included for

Table 4.2: Quantitative comparison of the Lymph data-set for dual border segmentation. HD: Hausdorff Distance (pixels); AMD: Absolute Mean Difference (pixels); Spec: Specificity (%); Sens: Sensitivity (%). Bold font indicates best performance.

Method		HD	AMD	Spec	Sens
Inner Wall -OSS	Mean	55.52	7.06	96.18	92.73
	STD	3.17	13.57	0.81	4.28
Inner Wall -Viterbi method	Mean	13.72	3.31	98.49	**98.00**
	STD	5.35	9.16	3.88	5.37
Inner Wall -Single s-Excess	Mean	15.6	4.9	**99.6**	93.6
	STD	10.0	3.2	0.6	4.9
Inner Wall -Double s-Excess	Mean	**9.8**	**3.1**	99.2	96.9
	STD	4.3	1.9	0.8	3.1
Outer Wall -OSS	Mean	51.0330	7.0631	97.34	91.15
	STD	22.59	3.55	0.62	5.56
Outer Wall -Viterbi method	Mean	23.31	4.67	99.16	94.80
	STD	2.88	10.14	0.69	4.6
Outer Wall -Single s-Excess	Mean	8.1	2.4	**99.5**	97.8
	STD	3.7	0.8	0.5	1.3
Outer Wall -Double s-Excess	Mean	**7.4**	**2.0**	99.1	**98.7**
	STD	3.1	0.8	0.6	1.1

ease of comparison). It can be seen that we obtain comparative results using the s-excess graph method, which is improved with the dual method segmentation. For the most part, these results are not significantly improved over the method already in place, however they do present an improvement in certain circumstances, namely very poor data sets. In some cases, when the borders are segmented individually, in images with insuficient image intensity or missing data over a significant proportion of the image, it is possible for both borders to merge or overlap (see Fig. 4.15). The reconstructed vessel is shown in Fig. 4.16.

4.5 Conclusions

Our results show that our proposed method is a reliable approach to automatically segmenting both inner and outer surfaces of the walls of the lymph vessel. By combining OSS and HMM, we are able to find a global minimum to the segmentation problem in polynomial time without
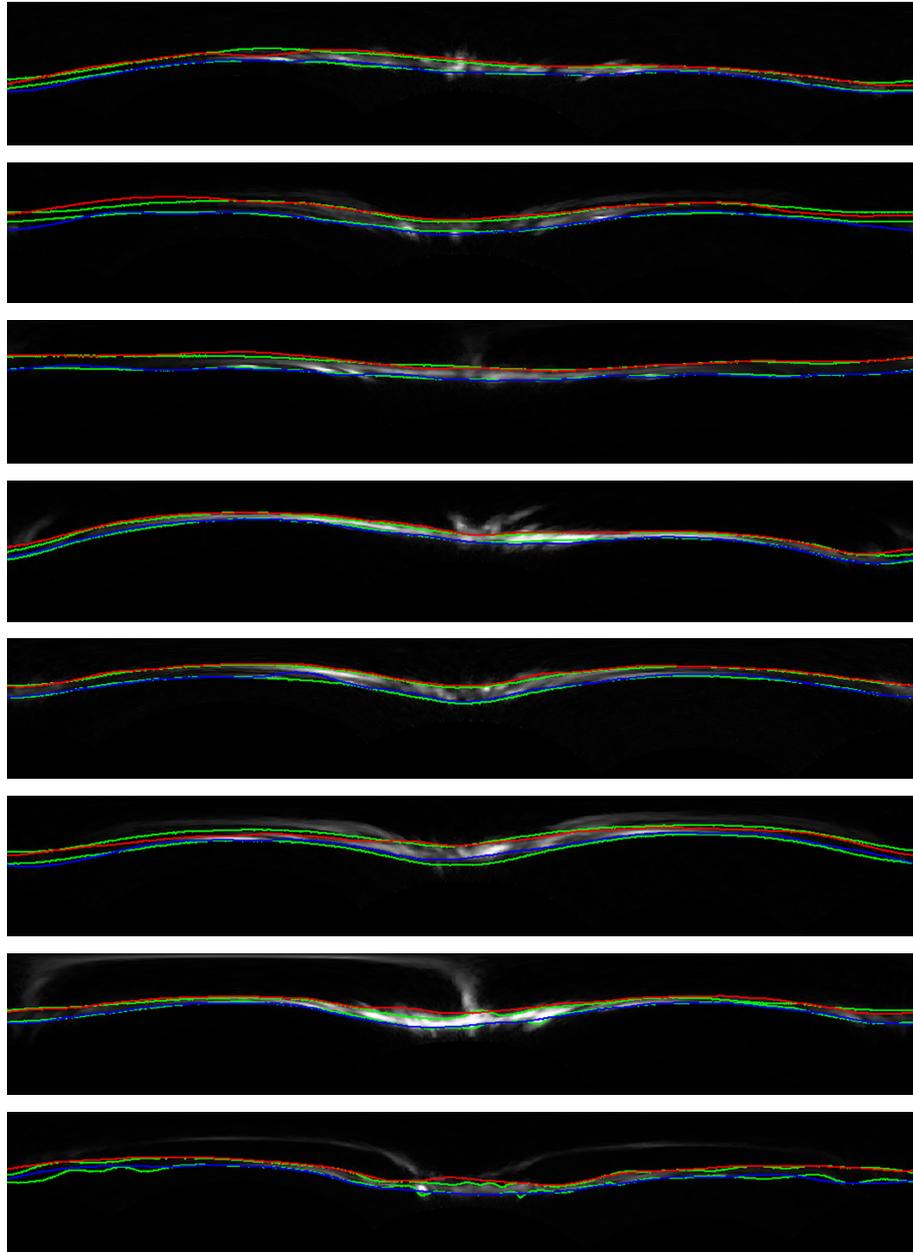
Figure 4.13: Results showing the segmented walls (red & blue) and the manually labeled ground truth(green) for a selection of different lymph vessels.
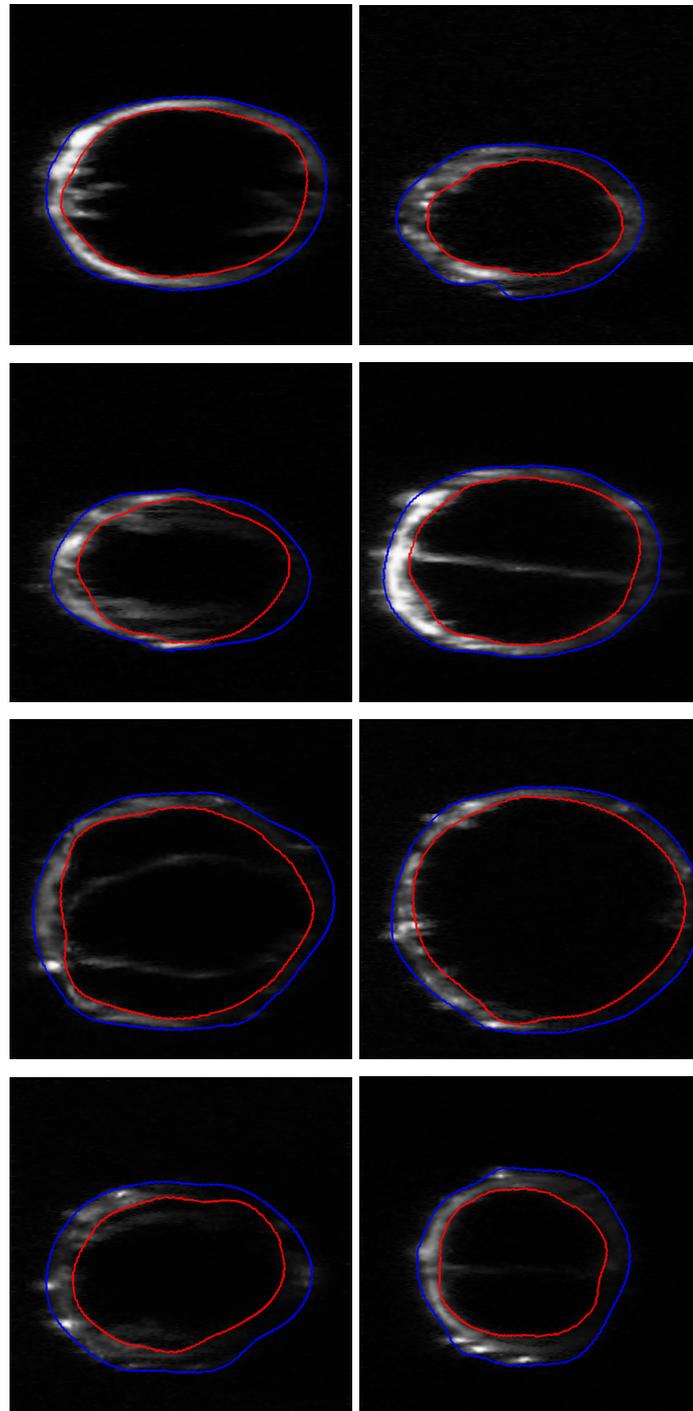
Figure 4.14: Results showing the segmented walls (red & blue) in the wrapped images corresponding to those in Fig.4.13 for a selection of different lymph vessels.

Single Border   Simultaneous Dual Border
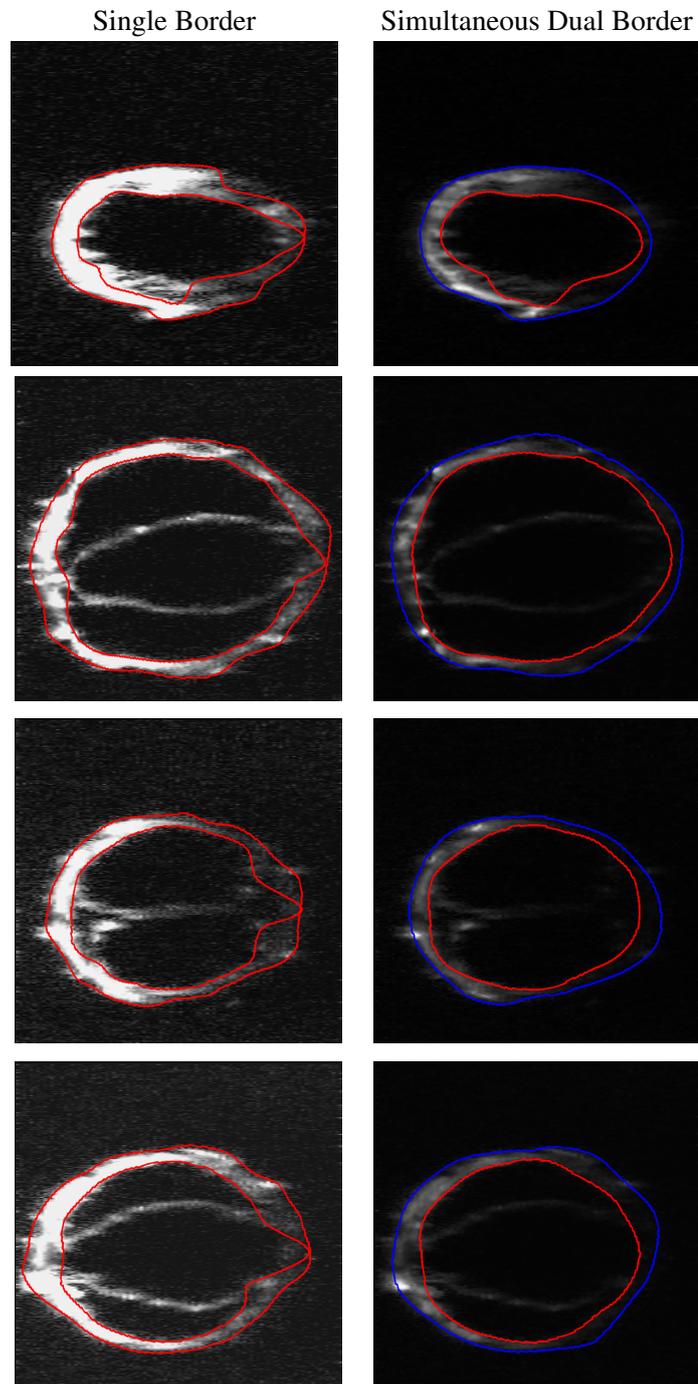
Figure 4.15: Failed segmentations obtained from single border segmentation, and the results shown for those images with dual border segmentation. Note how by using the simultaneous segmentation of both borders, this problem can be avoided.
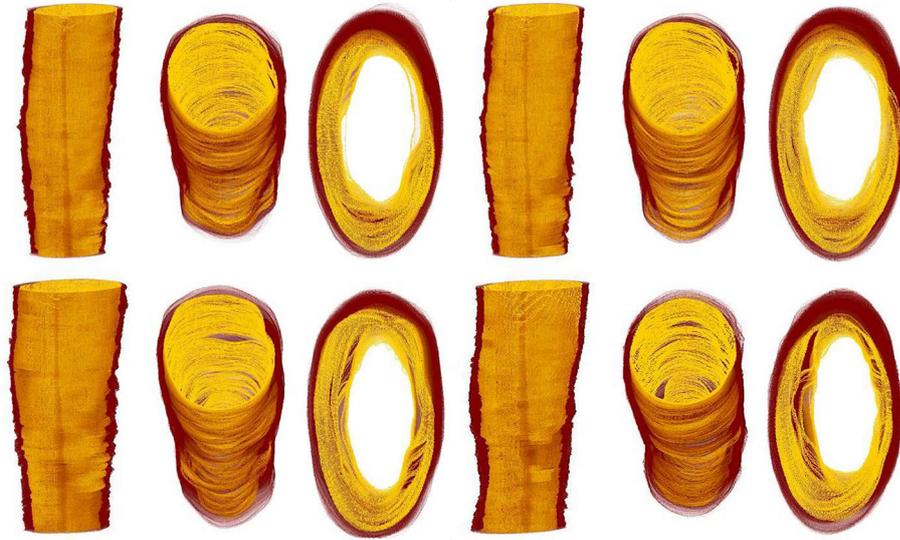
Figure 4.16: Results showing several examples of the reconstruction of the vessel from the segmented walls using dual segmentation. Yellow represents the inner wall, and red the outer wall. Note the problems caused by insufficient image features are now resolved.

user intervention despite the low quality, and diffuse nature of the confocal images taken from the lymph vessels. Also, by adapting our method to the s-excess method, and including arcs to simultaneously segment both borders we get a result that improved qualitatively although overall not qualitatively. The improvement for the dual border segmentation lies in the few erroneous cases where the image quality is very poor. It doesn't achieve significantly better results overall, as it is often the case that the border thickness can change dramatically. There are pronounced thickening in the regions of the valve anchor points, and the border becomes very thin in regions. In further work, in order to show a significant improvement overall in the segmentation by utilizing dual border segmentation, with inter-border arcs, some method would need to be in established to allow for the scaling of the border minimum and maximum thicknesses on an individual basis for each image.

Chapter 5

3D Valve Reconstruction

Contents

5.1   Introduction

After reconstructing the vessel walls, the next logical stage is to segment the valve in 3D. This poses a problem, as although (in most cases) finding the tip of the valve is straightforward, the hinge region presents a significantly greater difficulty. Likewise, regions in the "middle" of the valve are clear enough, the areas of interface with the wall present a similar problem as the hinge region. Fig. 5.1 clearly shows some of the difficulties involved in identification of the lymph valve.

When working in 3D it is important to look at surfaces rather than direct shortest paths [222, 223, 224, 225]. It is a well know phenomenon that although the minimal surface between two closed shapes separated by height is a catenoid, the shortest path between any two points *A* and *B* on those surfaces is a straight line (This is without taking into account any external weighting). This can be seen clearly in 5.2 where the shortest path between *A* and *B* does not fit onto the minimal surface between their respective shapes. This makes it difficult to expand our method directly into 3D, as although we may find the shortest path, their is no guarantee
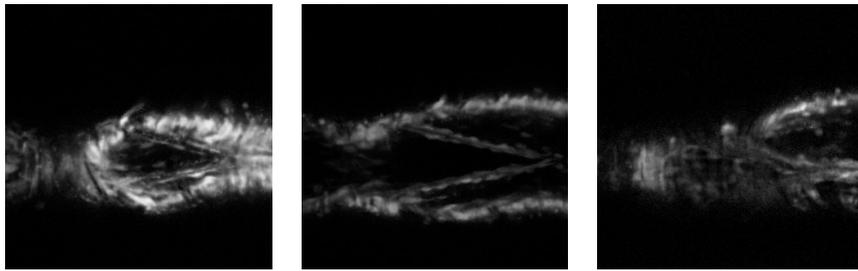
Figure 5.1: Images showing the valve region of the lymph vessels prior to segmentation. Image on the left is from the start region, middle image is centrally situated in the series, and that on the right is from the terminal region of the series. Note the difficulty in discerning valve boundaries at the start and end of the sequence.
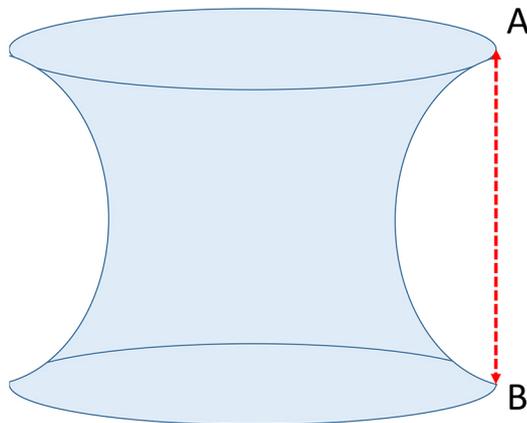
Figure 5.2: Demonstration of how shortest path does not necessarily follow the minimal surface for 3D objects. Adapted from [27]

that it will lie on any derived minimal surface. When looking at 3D minimal surfaces, similar constraints are needed in order to provide a (non null) result. Namely that the surface encloses a particular region of space, and that it is bounded by a series of points. These constraints are similar to those found in 2D, being those of a closed object being separated from the background (for example in a min-cut/max-flow type segmentation), or having start and end points (such as working with Dijkstra's algorithm), respectively. In our segmentation, we will satisfy these constraints by finding the boundary of the desired object first, which will then constrain the surface segmentation.

There is a great deal of interest in methods to find a minimal surface in 3D, Appleton [226]

suggested, for example, a method of solving a continuous max-flow algorithm, whereas other methods have been put forward using geometric constraints [23], regional properties [227], and shape priors [228] to give but a few examples. Unlike in 2D segmentation, minimal surfaces must always be closed objects. They can be thought of like blowing a soap bubble, with the ring used to blow the bubble as the boundary constraining it, and the bubble itself as the surface. By using an adaptation of our 2D method, we can provide a boundary to meet the 2nd constraint criteria required for minimal surface segmentation. This will be combined with the graph construction to provide segmentation of the surface as a whole.

5.2 Proposed Method

5.2.1 User input

Currently we use input from the user to assist in labeling the root and tip of the valve. This is done using an adaptation of the imprecise user input which was used in the 2D segmentation method. User points are placed corresponding to the tip and the hinge points on the valve itself. These user points are used to find the valve boundary, which will be used to find the surface of the valve. The segmentation forms a closed curve starting and finishing in the same point, circumscribing the boundary of the valve.

5.2.2 Graph Construction

In order to segment the 3D structure of the valve, we must first construct the problem in the form of a graph minimization problem. in order to do this, we implement an adaptation of our previous graph structure.

In this graph, the 3D image structure $\mathcal{I}_{3D}$ is a representation made up from multiple image layers $\mathcal{I}$ constructed from the sequential slices of the confocal series. The number of layers used is $2h$ where h is the number of slices in the confocal image series. The graph structure is made up of the slices s from s_1 to s_n, then the layers are replicated in inverse order (adding slices s_n to s_1), to construct a cube of twice the height of the original image stack. We construct a graph $\mathcal{G} = (V, E)$, as before, where V is the set of vertices, and E the set of weighted edges. For each voxel v, there exits an edge e to each of its neighboring pixels on the same layer and to its neighbor in the subsequent layer. Therefore, a pair of neighboring voxels $(p, q) \in V$ with a corresponding edge $e = (v_p, v_q)$ also have an edge to the corresponding point on the

superseding layer $e = (v_{p_l}, v_{p_{l+1}})$, where l represents the current layer of the image. For each edge, we assign a weight w to build a weighted graph (V, E). These weights are calculated based on whether the edge is internal to a layer (w_i) or trans-layer (w_x). In order to be able to solve this problem in polynomial time, we enforce an order (as previously for the 2D method) moving through the image from l_1 to l_{2n} where n is the depth of the image cube, and layers l_1 to l_n represent moving through the images using the tip terminal point as a guide, then layers l_{n+1} to l_{2n} are returning using the hinge terminal point. This is done by ensuring that the inter-layer arcs are unidirectional. We once again use the user points as elastic soft constraints to help guide the segmentation.

User points are placed for both the ends of the valve (the tip and the hinge), and the source s is the tip point on layer 1 and sink t is set to the same point(as we need to create the full closed outline of the valve) but on layer l_{2n}, we also place user points on the ends of the valve for each layer to act as guide in the segmentation.

Once again, like in the 2D method, edges of zero weight are not added from the start node s to each pixel in the first layer, and from the last layer $2n + 1$ to the terminal node t. Again making sure the first and the last user points elastic and not hard constraints, and all user points are treated equally.

If P is the set of pixels in the image, P_s is therefore the subset of pixels that also fall on the boundaries of our super pixels, and p_i and q_i are pixels in layer i giving v_{p_i} as the vertex p in layer i, we can define the set of nodes V as

$$V = \{s, t\} \cup \{p_i \in P_s \wedge 1 \leq i \leq k + 1\} \tag{5.1}$$

and thusly the set of edges as,

$$E = \begin{cases} (s, v_{p_1}) | p \in P_s & \cup \\ (v_{p_{k+1}}, t) | p \in P_s & \cup \\ (v_{p_i}, v_{q_i}) | (p, q) \in N \wedge 1 \leq i \leq k + 1 & \cup \\ (v_{p_i}, v_{p_{i+1}}) | p \in P_s \wedge 1 \leq i \leq k + 1. \end{cases} \tag{5.2}$$

5.2.3 Valve Boundary Detection

The first stage of our valve leaflet segmentation is to segment the boundary. This is done by using a modified version of our 2D code described previously. Using the constructed graph

$\mathcal{G}$ and manually labeled points for the apex and root of the valve, we assign weights to the edges in a similar manner as before. The edges on the directed layered graph are categorized as internal edges w_i within individual layers and inter-layer edges w_x. The weighting for these two types of edges is assigned differently. The internal edges are assigned weights a weight based on edge features, i.e. boundary based edge weights similar to the 2D method are used, but not region based edge weights. The boundary based edge weights are calculated based on the magnitude of image gradients, created for example with a Sobel filter, i.e. using an edge detection function $g_e = 1/(1+\nabla I)$ where I denotes the image layer. Hence, for any given edge between neighboring pixels (v_p, v_q), we assign a weight (w_e) according to

$$w_i((v_p, v_q)) := \frac{1}{2}||p-q||(g_e(p) + g_e(q)). \tag{5.3}$$

The attraction force imposed by user points is materialized through the inter-layer edge weights w_x. We apply distance transform to the user points in each layer of the graph, and the inter-layer edge weight is assigned as $w_x = d(v_{p_i}, v_{p_j})$ where d denotes the distance transform function. For layers l_1 to l_n we use the user points corresponding to the tip, and layers l_{n+1} to l_{2n} use the user points derived from the hinges. In this way, distance weighting produces iso-linear bands of weight around each user point, with increasing weight to go through to the next layer as the distance from the user point increases, favoring transition between layers as close as possible to the user point without straying too far from hard edges. In this way, finding the boundary of the valve becomes an energy minimization problem similar to our previous 2D work.

The energy function for any curve C in our method is a combination of two terms, i.e. for any arc C between two points p_i and q_j where the points are

$$C(p,q) = w_x + w_i \tag{5.4}$$

as w_x can be written as

$$\alpha \sum_{i=1}^{k} ||C(s_i) - X_i|| \tag{5.5}$$

and likewise w_i can be written as:

$$\beta \int_0^{L(C)} g(C(s))ds, \tag{5.6}$$

This is all providing that the points are treated as being in a sequential order, and that the interconnections between layers are uni-directional. The overall energy function can then be

expressed as:

$$\mathcal{E}(C, s_1, ..., s_k) = \alpha \sum_{i=1}^{k} ||C(s_i) - X_i|| + \beta \int_0^{L(C)} g(C(s)) ds \quad s.t. s_i < s_j, \forall i < j. \tag{5.7}$$

where α and β are real constants used to weigh the effects of the edge based and distance based terms, the effects of changing these can be seen in Fig. 3.7 in a previous chapter.

The first term in our cost equation is used to enforce the soft constraints placed by the user as a guideline to the terminal ends of the valve, and it penalizes the paths further away from these user points, helping the user control the segmentation. The second term is the boundary based data term that prefers the path passing through strong edges, the images are preprocessed to improve these images as described above. By using the layered graph construction, the minimization of the energy function is achieved by finding the shortest path from the start point s to the end point t through the 3D cube.

As the graph will be very large, and therefore computationally expensive, the graph was constructed in segments as needed to prevent it from becoming too big to compute. By using Dijkstra's algorithm, as before, this allowed the points on the graph to be loaded in as needed, we operated on 10 layers at a time, as this provided a sufficient reduction in the size of graph being worked on in memory. To further reduce the computational overheads, the image was automatically cropped to a tight box around the region of the valve, by using the manually input points to give a rough boundary, which was expanded in each direction to ensure the valve fitted within these confines in its entirety. Once again note, the inter-layer edges are unidirectional so that the path can not travel back to previously visited layers, to avoid making the segmentation problem NP hard.

The results of this 3D segmentation, gave the boundary outline for the valve leaflet (see Fig. 5.3).

5.2.4 Valve Surface Segmentation

Once we obtained our boundary, the next stage was to calculate the point cloud for points on the surface of the valve. For this, the image stack was comprised of layers l_1 to l_n where n is the number of slices in the series. Note this is a smaller graph than was used for the border, as there was no need to have the $2n$ layers to ensure order in the user points. This was done using the voxel edge derived intensities for any given voxel v in the image stack, these are based
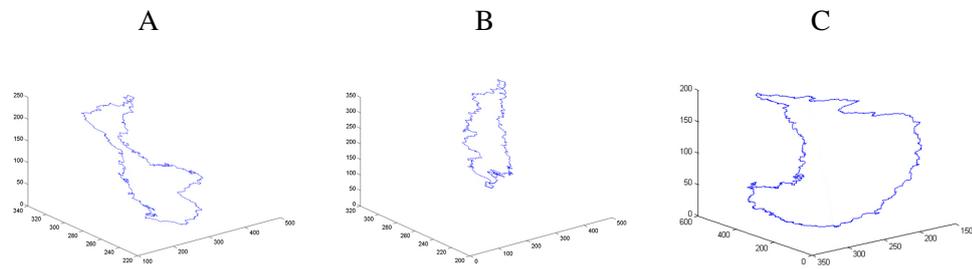
Figure 5.3: 3D Segmentation showing the boundary of the valve leaflets obtained. Note in regions where the features were difficult to label or absent (such as (A)) then the boundary is difficult to find and not smooth.
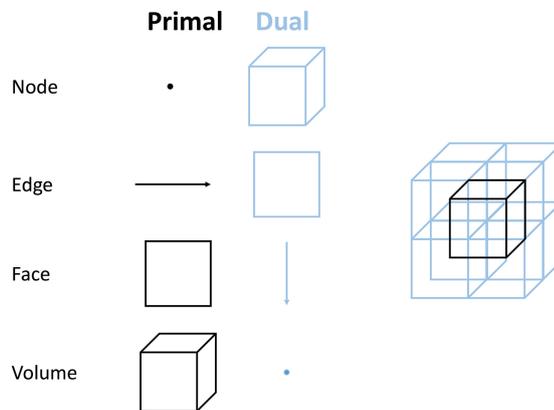
Figure 5.4: Schematic showing the relationship between primal and dual graphs in 3D Adapted from [27]. Every node in the primal graph is represented as a cube in the dual. Every edge in the primal becomes a facet. every face and edge and finally every volume a node. In this way primal edge weights correspond to dual facet weights and *vice versa*.

on the edge map created using a Sobel filer on the image (pre-processed with a log Gabor filter). A minimal surface segmentation performed using these weights, based on the method demonstrated in Grady 2010 [27] with adapted cost functions and weighting, and modified to return a point cloud rather than faces.

The first stage is to construct a lattice framework to represent the 3D image. We first expand our original graph construction into a dual graph. From out planar primal graph, we define a dual graph by replacing each node with a facet, can connecting two nodes if their respective facets share an edge. This is shown in Fig. 5.4.

We can therefore define our lattice using the same connectivity as we used in our previous 2D graph, namely with nodes being connected to their 8 neighbors on their layer, and immediate neighbor nodes on the layer above and below themselves. The lattice can be represented by set $P = (V, E, F, C)$ where the vertices $v \in V$, edges $e \in E \subseteq V \times V$, facets $f \in F \subseteq E \times E \times E \times E$ and cubes $c \in C \subseteq F \times F \times F \times F \times F \times F$, if we work with a 6 connected neighborhood. For any given edge e_i we assign a weight w_i, with all weights being positive.

The minimum surface weight problem can therefore be defined as:

$$\min_z Q(z) = \sum_i w_i z_i, subject to Bz = r, \tag{5.8}$$

where z is a positive vector indicating whether the facet is present in the minimal-weight surface. w_i is the weight of the facet, which corresponds to the weight of the edge in the 2D graph, and is defined as:

$$w_i = \alpha \sum_{i=1}^{k} ||C(s_i) - X_i|| + \beta \int_0^{L(C)} g(C(s)) ds \quad s.t. s_i < s_j, \forall i < j. \tag{5.9}$$

and B is the incidence matrix boundary operator and r is a signed vector indicative of a closed contour. Once the problem is formulated, it can be resolve by using a Minimum-cost Circulation Flow Network (MCFN) based on work by Bitter *et al* [229]. This can be formed in terms of the variable f thusly:

$$\max_{f'} z_0^T f', s.t. C^T f' = 0, f' \leq \tilde{f} = w. \tag{5.10}$$

which requires the finding of the maximum divergence-free flow, passing through an initial surface z_0, which has the capacities given by the weights in the graph.

Once the MCFN has been solved, the results show facets that are to be included in the final solution. It is then a trivial task to deconstruct the dual lattice back to its primal roots and generate a node representing the center of the volume indicated by the facet. These nodes will then be used to generate the final result by having a 3D RBF interpolation applied to them, to smooth outliers and provide a smooth surface which represents the valve itself.

5.3 Results

Our results were obtained from a data-set of five confocal series, from different lymph valves. These individual data-sets (those used previously for the vessel wall segmentation) each comprised of around 400 consecutive images of the lymph valve. These were used to construct the point cloud and surfaces shown. The results from the minimal surface segmentation are shown in Fig. 5.5 and Fig. 5.6, with the surfaces shown in Fig. 5.7 and Fig. 5.8. These point clouds represent voxels on the surface of the valve. Finding the surface for the valve is very problematic, as it is very feint, and often merges into the wall, or exits the side of the frame, the effect of this can be seen in the alternate views shown in Fig. 5.5. In order to obtain a coherent surface over these point clouds it is necessary to perform smoothing and RBF interpolation on the clouds. The surface resulting from this is shown in Fig. 5.6, with a color map applied to show the bands obtained from the RBF centers. The RBF centers for interpolation were taken at regular intervals (10 slices) through the image, as this provided an adequate smoothing to produce a surface, whilst keeping the computational overheads small so the operation is fast, and the resultant image manageable.

As can be seen from the data, the valve surface segmentation still has some uneven regions. With a larger data set, in my belief it would be possible to greatly improve on these results by introducing a shape prior in order to guide the surface segmentation. Fig. 5.9 shows some of the problems faced by the segmentation, although both these images show a valve that can be clearly seen (unlike the start and end regions shown in Fig. 5.1). The shape of the valve changes considerably as you move through the slices in the set, with some severe direction changes in some cases. Also, due to the nature of confocal images, the fluorescence of the image is uneven. This was significantly easier to deal with on the vessel wall segmentation, as the overall shape was regular and constraints could be used.

5.4 Conclusion

The proposed method gives a reasonable segmentation of the lymph valve. It is limited by several factors however. The first problem is in boundary segmentation, and is the large amount of user input that is required. This problem is mainly due to the nature of the images which make even manual segmentation tricky, especially in the early and late stages. In some cases, this proves almost impossible without pre-processing, as the valve was too feint to be seen
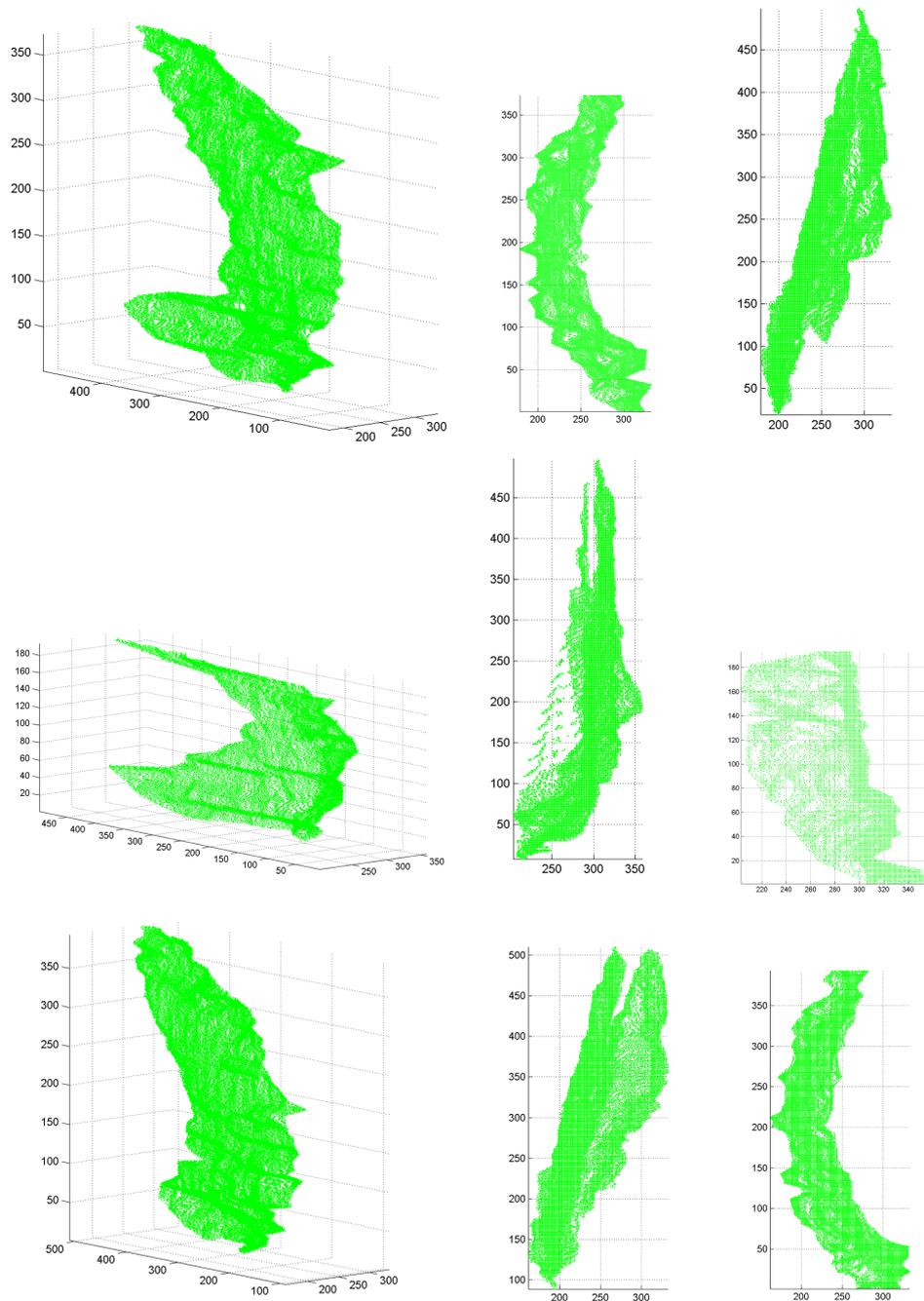
Figure 5.5: 3D Segmentation results, showing the point clouds obtained from the surface segmentation. From left to right they are: an off center view displaying the valve structure, X-Y, and X-Z planes, for each data-set. Irregularities in the point clouds are caused by insufficient features, or artefact on the original images. This makes the segmentation a difficult process, as in some cases, the artifact is a much stronger "feature" than the desired target.
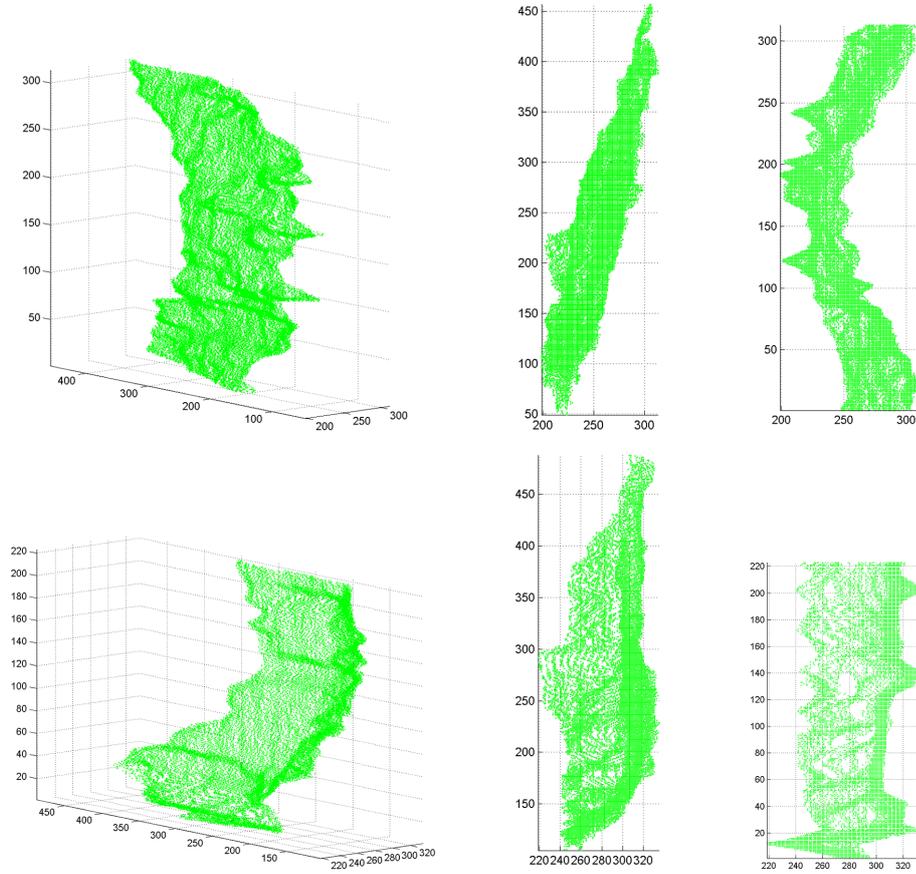
Figure 5.6: 3D Segmentation results, showing the point clouds obtained from the surface segmentation. From left to right they are: an off center view displaying the valve structure, X-Y, and X-Z planes, for each data-set.

on the screen. The proposed method for boundary segmentation does show the versatility in our 2D method, as it could easily be modified to a 3D role (in the case here of finding the boundary). The proposed method builds on the work in [27] by expanding the cost function quite considerably, and modification to the graph construction to allow for 3D segmentation. The surface segmentation also proved very problematic. The poor quality of the images, couple with the changing shape and irregularity of the valve made segmentation difficulty. The results obtained show an acceptable segmentation of such a tricky object, and in my opinion for a good starting point to expand on this work. In order to inform the segmentation, other methods could be applied to strengthen the results. Shape prior would make a very good addition to this method, as it could be combined with the cost terms in our graph construction to penalize
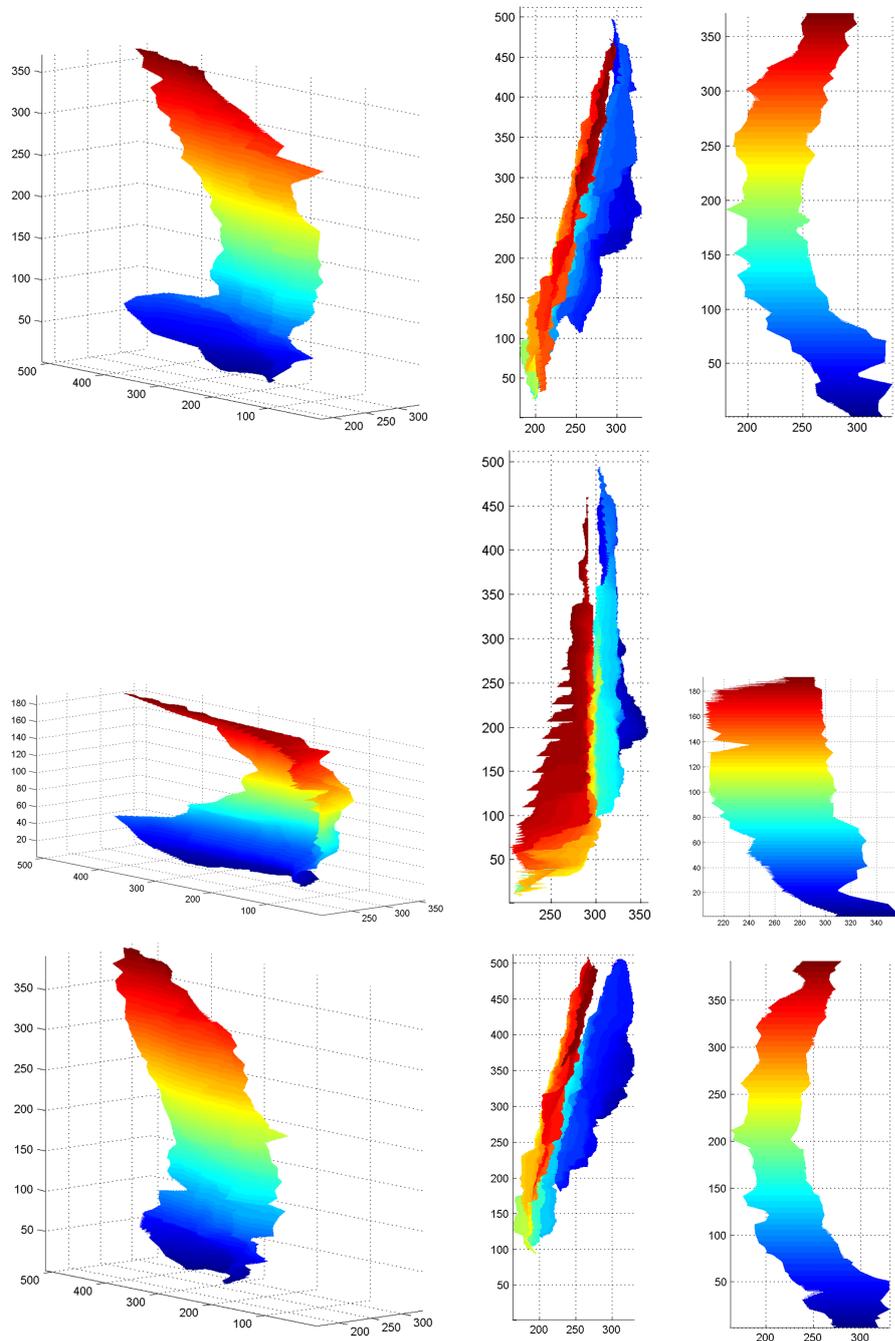
Figure 5.7: 3D Segmentation results, showing the surface mapped over the point clouds. Colored bands represent the regions used for the RBF interpolation. From left to right they are: an off center view displaying the valve structure, X-Y, and X-Z planes, for each data-set. It can be seen that the surface represents the valve for the majority of the surface, but due to issues with insufficient features, and artifacts (especially around the hinge area and interface with vessel wall) there are areas where the segmentation fails.
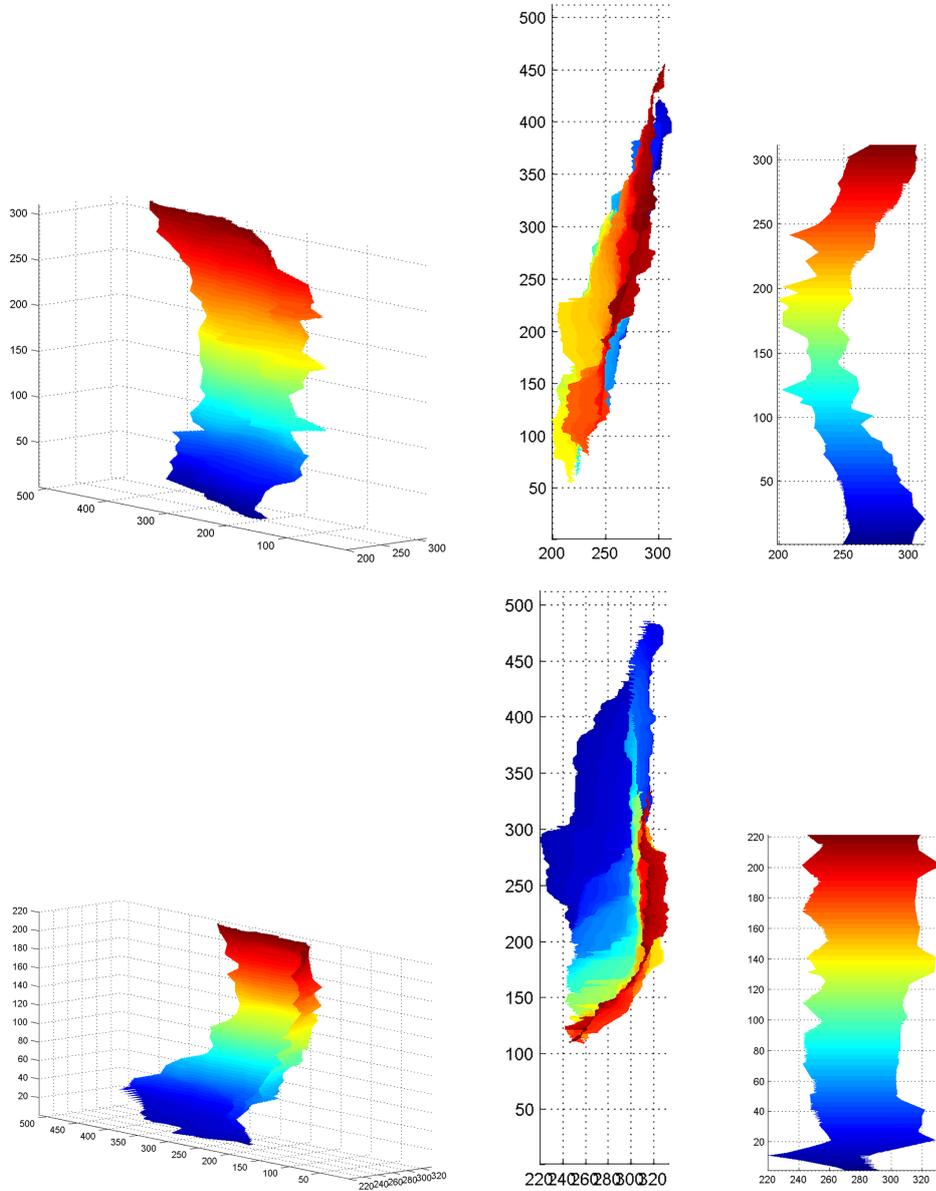
Figure 5.8: 3D Segmentation results, showing the surface mapped over the point clouds. Colored bands represent the regions used for the RBF interpolation. From left to right they are: an off center view displaying the valve structure, X-Y, and X-Z planes, for each data-set. It can be seen that the surface represents the valve for the majority of the surface, but due to issues with insufficient features, and artifacts (especially around the hinge area and interface with vessel wall) there are areas where the segmentation fails.

114
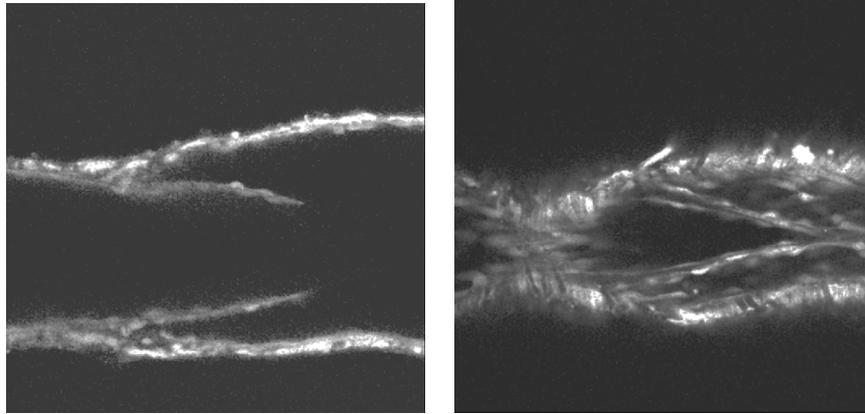
Figure 5.9: Processed data showing the valve structure in a single data set. Notice how the shape and quality of the image changes from the slice on the periphery of the valve (right image) compared to a slice from the mid region (on the left)

the segmentation from straying from an accepted shape. However, in order to achieve this, a significantly larger data-set would be require to provide training and test data. Even utilizing shape prior, the regions near the interface between valve and vessel wall may still prove very problematic. As can be seen in Fig. 5.1, it is almost impossible to discern where the valve starts and finishes in these regions, and even in the selected regions, where the valve can be seen, it differs greatly in shape as you move through the slices Fig. 5.9.

Chapter 6

Conclusions and Future Work

Contents

6.1   Conclusions

In this work we proposed a reliable and robust segmentation method for medical imaging, that provided accurate segmentation even in noisy images with artifacts present. This was mainly adapted towards the requirements for IVUS and OCT segmentation, but was also shown to be strong at many different types of both open and closed segmentations. This was successfully expanded into 3D to segment the boundary of the lymph valve. We expanded and added to our work to perform automatic segmentation and reconstruction of lymph vessel walls in 3D, and segment out the valve as a 3D surface.

The main contributions are summarized as follows:

1. Combined Region/Edge Based Segmentation, with minimal elastic user input. This robust method was developed for use in catheter based medical imaging systems, where it was tested and compared favorably to state-of-the-art methods. It was also shown to provide high quality segmentation in both other medical imaging situations and real world images. The nature of its approach allowing open and closed segmentation with a great deal of accuracy in many situations.

2. Graph Optimization and Pruning. By uptilting a pre-processing over segmentation using mean shift, we divided the image into a number of super-pixels. These were used to prune the graph, removing nodes that were not on the edge, and/or in the same region, to improve the speed and functionality of the algorithm.

3. We provided an automatic segmentation method in which to reconstruct lymphatic vessel valve regions. This method utilizes OSS and HMM to automatically detect both vessel walls in lymph vessels, in order to reconstruct the vessel in 3D. By using a coarse OSS segmentation as the seed input for our HMM segmentation, which uses a series of RBF centers to shift the seed segmentation, we have an efficient and accurate segmentation. This segmentation is performed in polar coordinate images, with samples taken evenly along the segmentation line.

4. Pre-processing and formatting of confocal microscopic images. In order to improve the quality of the lymph vessel images prior to segmentation, we pre-process them using a VED filter to improve the image quality, then process to improve contrast and to create a cross-sectional shape. This increased the visibility of poorly defined edges, and was applied in some cases to help confirm manual labeling (as image contrast could be very poor).

5. Using s-Excess graph to simultaneously segment both borders. Using a modification of our HMM method, we simultaneously segmented both borders using an s-excess graph minimization algorithm. This includes weights for inter-border arcs, so control over the thickness of the wall can be maintained. This provides a solution to some of the error cases in HMM segmentation alone (as there are many images which have broken, and incomplete borders), whilst maintaining the same overall accuracy levels.

6. Semi-automatic segmentation of lymph valve border. Expanding on our 2D semi-interactive segmentation we segment the boundary of the lymph vessel in 3D. By constructing the graph in a similar manner to earlier, we can segment the boundary of the lymph vessel in 3D. However, as this is working with a much larger graph, we need to minimize the amount of nodes that are worked on. We do this by pruning nodes too far from a cube created with minimum and maximum user values. Also, we utilize one of the features of Dijkstra's algorithm, and only create nodes for layers as they are needed in order to diminish the memory overhead of the graph.

7. Segmentation of the lymph valve. Using the border we segmented, we can then use a minimal surface segmentation to find the border in 3D. This is then smoothed using a series of RBFs in order to provide the final result.

6.2 Further Work

There are several areas where we believe this work can be built upon. Our plans for further development are to aim to add more automation to the lymph segmentation process. At its current stage, it uses manual labeling to inform the segmentation of the boundary of the lymph valve. This is quite a tricky and time consuming process, due to the number of images and the quality and lack of clarity exhibited in some of them. Once the process has become more automated, the next task is to co-localism the valve structure onto the 3D vessel reconstruction for a complete representation of the structure. I believe the best approach (with the larger data-set now available) would be to use a machine learning system (such as Random Forest) with a manually labeled set of hinge and tip points and a set of prior shapes for lymph valve shapes. I do not believe that the use of one feature alone would be strong enough, as (especially for the hinge) they are very tricky to label. With the added information of a valve shape prior (which could be obtained by manually labeling or the proposed 2D segmentation) it would probably be sufficient to train an algorithm with a suitably large training set.

The surface segmentation of the valve itself would benefit greatly from some extra constraints and features included in the cost function. With a larger data-set, it should be possible to add some shape prior constraint to the cost function. This would considerably improve the quality of the results, in my opinion, making them more robust. In order to achieve this it would require manually labeling several valve series, which is a time consuming task. In this work, we have looked at finding a single surface that matches the valve. Improvements may be obtained by treating the valve as a solid closed object with constraints as to its thickness. This should help avoid some of the problems we have with incomplete valve image data, where the single surface is drawn to an artefact region as this is brighter than the desired surface. If the segmentation was to be a closed object, then this could be prevented.

At the time of this work, we had a relatively limited data set (a large number of individual images, but only 8 complete sets). We now have access to a larger data set (another 15 sets) so the first stage would be to add more training data to the HMM, and expand on that. The

plan is with an improved data set, the dual segmentation of internal and external boundaries could be further improved. At its current stage, it has no significant improvement overall than the single method proposed, but it does have the advantage that the boundaries never meet or cross. This is essential if the model is to be useful in the long term, and is the greatest weakness of the single boundary method. With an increased data set, the goal is to make this inter boundary thickness another learned feature, with the only manually encoded constraint being that boundary thickness must be greater than zero.

Another planned expansion to the work is to modify the code for the lymph segmentation to apply it in the cardiovascular images. This is a non-trivial task as both IVUS and OCT have strong features that would help this, but also inherent weaknesses that will make the task tricky. OCT for example, has a clearly defined luminal boarder, abut the media-adventitia border is a much weaker feature. The converse is true in IVUS images. We hope to expand on our 2D method to include segmentations of either the media-adventitia border in OCT, or the lumenal border in IVUS.This will eventually lead to the final goal, which is to be able to combine this with other modalities (especially angiography) to be able to provide an accurate, and topographically correct 3D reconstruction of a vessel.

Appendix A

List of Publications

In addition to the publications listed below, a journal paper is under review.

1. J.-L. Jones, E. Essa X. Xie, Automatic Segmentation of Lymph Vessel Wall using Optimal Surface Graph Cut and Hidden Markov Models, IEEE Engineering in Medicine and Biology Conference(EMBC) 2015 (accepted).

2. E. Essa, X. Xie, and J.-L. Jones, Minimum s-Excess Graph for Segmenting and Tracking Multiple Borders with HMM, Int'l Conf. Medical Image Computing and Computer Assisted Intervention (MICCAI), October 2015. (accepted).

3. E. Essa, X. Xie, and J.-L. Jones, Graph Based Lymphatic Vessel Wall Localization and Tracking, Graph-Based Representations in Pattern Recognition, pp. 345-354, May 2015.

4. J.-L. Jones, X. Xie, and E. Essa, Combining Region-based and Imprecise Boundary-based Cues for Interactive Medical Image Segmentation, International Journal for Numerical Methods in Biomedical Engineering, volume 30, issue 12, pages 1649-1666, December, 2014.

5. J.-L. Jones, E. Essa, X. Xie and J. Cotton, Interactive segmentation of lumen border in OCT, In Proceedings of International Conference on Computational and Mathematical Biomedical Engineering (CMBE), December 2013.

6. J.-L. Jones, X. Xie, and E. Essa, Image Segmentation using Combined User Interactions, In Proceedings of the Computational Visual Media Conference, September 2013.

7. J.-L. Jones, E. Essa, X. Xie, and D. Smith, Interactive Segmentation of Media-Adventitia Border in IVUS, In Proceedings of 15th International Conference on Computer Analysis of Images and Patterns (CAIP), pages 466-474, August 2013.

Bibliography

[1] N. Townsend, J. Williams, P. Bhatnagar, K. Wickramasinghe, and M. Rayner, "Cardio-vascular disease statistics 2014," *British Heart Foundation Annual Report*, 2014.

[2] E. Borenstein and S. Ullman, "Class-specific, top-down segmentation," in *Proceedings of the 7th European Conference on Computer Vision-Part II*, ECCV '02, (London, UK, UK), pp. 109–124, Springer-Verlag, 2002.

[3] "Anatomy of the heart." `https://en.wikipedia.org/wiki/Heart_rate#/media/File:Wiki_Heart_Antomy_Ties_van_Brussel.jpg`. Accessed: 2015-06-22.

[4] "Anatomy of an artery." `https://en.wikipedia.org/wiki/Artery#/media/File:Blausen_0055_ArteryWallStructure.png`. Accessed: 2015-06-22.

[5] "Progression of atherosclerosis." `https://en.wikipedia.org/wiki/Atherosclerosis#/media/File:Endo_dysfunction_Athero.PNG`. Accessed: 2015-06-22.

[6] "Blausen 0623 lymphatic system female." `https://commons.wikimedia.org/wiki/File:Blausen_0623_LymphaticSystem_Female.png#/media/File:Blausen_0623_LymphaticSystem_Female.png`. Accessed: 2015-07-15.

[7] "Electromagnetic spectrum - introduction." Imagine.gsfc.nasa.gov, 2015.

[8] Bleiglass, "Angiography ha1." https://commons.wikimedia.org/wiki/File:Ha1.jpg/media/File:Ha1.jpg.

[9] "Confocal microscopy." `https://en.wikipedia.org/wiki/Confocal_microscopy#/media/File:Confocalprinciple_in_English.svg`. Accessed: 2015-07-15.

[10] E. Essa, X. Xie, I. Sazonov, and P. Nithiarasu, "Automatic IVUS media-adventitia border extraction using double interface graph cut segmentation," in *International Conference on Image Processing*, pp. 69–72, 2011.

[11] A. X. Falcão, J. K. Udupa, S. Samarasekera, S. Sharma, B. E. Hirsch, and R. de A. Lotufo, "User-steered image segmentation paradigms: Live wire and live lane," *Graphical Models and Image Processing*, vol. 60, no. 4, pp. 233 – 260, 1998.

[12] T. Windheuser, T. Schoenemann, and D. Cremers, "Beyond connecting the dots: A polynomial-time algorithm for segmentation and boundary estimation with imprecise user input," in *IEEE International Conference on Computer Vision*, pp. 717–722, 2009.

[13] X. Li, X. Wang, and Y. Dai, "Robust global minimization of active contour model for multi-object medical image segmentation," in *Instrumentation and Measurement Technology Conference (I2MTC) Proceedings, 2014 IEEE International*, pp. 1443–1448, 2014.

[14] L. Cohen and I. Cohen, "Finite-element methods for active contour models and balloons for 2-D and 3-D images," *IEEE Transactions on Pattern Analysis and Machine Intelligence*, vol. 15, no. 11, pp. 1131–1147, 1993.

[15] V. Caselles, R. Kimmel, and G. Sapiro, "Geodesic active contour," *International Journal of Computer Vision*, vol. 22, no. 1, pp. 61–79, 1997.

[16] C. Xu and J. Prince, "Generalized gradient vector flow external forces for active contours," *Signal Processing*, vol. 71, no. 2, pp. 131–139, 1998.

[17] N. Paragios, O. Mellina-Gottardo, and V. Ramesh, "Gradient vector flow geometric active contours," *IEEE Transactions on Pattern Analysis and Machine Intelligence*, vol. 26, no. 3, pp. 402–407, 2004.

[18] A. Jalba, M. Wilkinson, and J. Roerdink, "CPM: A deformable model for shape recovery and segmentation based on charged particles," *IEEE Transactions on Pattern Analysis and Machine Intelligence*, vol. 26, no. 10, pp. 1320–1335, 2004.

[19] X. Xie and M. Mirmehdi, "Mac: Magnetostatic active contour mode," in *IEEE Transactions on Pattern Analysis and Machine Intelligence*, pp. 632–646, 2008.

123

[20] E. N. Mortensen and W. A. Barrett, "Interactive segmentation with intelligent scissors," *Graphical Models and Image Processing*, vol. 60, no. 5, pp. 349–384, 1998.

[21] Y. Boykov and M.-P. Jolly, "Interactive graph cuts for optimal boundary & region segmentation of objects in n-d images," in *IEEE International Conference on Computer Vision*, vol. 1, pp. 105–112, 2001.

[22] H. Zhang, E. Essa, and X. Xie, "Graph based segmentation with minimal user interaction," in *Proceedings of IEEE International Conference on Image Processing*, pp. 4074–4078, 2011.

[23] Y. Li, J. Sun, C.-K. Tang, and H.-Y. Shum, "Lazy snapping," *ACM Transactions on Graphics*, vol. 23, no. 3, pp. 303–308, 2004.

[24] O. Veksler, "Star shape prior for graph-cut image segmentation," in *IEEE European Conference on Computer Vision*, pp. 454–467, 2008.

[25] C. Rother, V. Kolmogorov, and A. Blake, "Grabcut: interactive foreground extraction using iterated graph cuts," *ACM Transactions on Graphics*, vol. 23, no. 3, pp. 309–314, 2004.

[26] A. F. Frangi, W. J. Niessen, K. L. Vincken, and M. A. Viergever, "Multiscale vessel enhancement filtering," in *International Conference on Medical Image Computing and Computer-Assisted Intervention* (W. M. Wells, A. Colchester, and S. Delp, eds.), vol. 1496, pp. 130–137, Springer Berlin Heidelberg, 1998.

[27] L. Grady, "Minimal surfaces extend shortest path segmentation methods to 3d," *IEEE Transations on Pattern Analysis and Machine Intelligence*, vol. 32, pp. 321–334, Feb 2010.

[28] M. Dou, Y. Shi, J. Frahm, H. Fuchs, B. Mauchly, and M. Marathe, "Room-sized informal telepresence system," in *Virtual Reality Short Papers and Posters (VRW), 2012 IEEE*, pp. 15–18, March 2012.

[29] A. Sofou, G. Evangelopoulos, and P. Maragos, "Soil image segmentation and texture analysis: a computer vision approach," *Geoscience and Remote Sensing Letters, IEEE*, vol. 2, pp. 394–398, Oct 2005.

[30] D. Barik and M. Mondal, "Object identification for computer vision using image segmentation," in *Education Technology and Computer (ICETC), 2010 2nd International Conference on*, vol. 2, pp. V2–170–V2–172, June 2010.

[31] J. Gonzalez, I. S. Lim, P. Fua, and D. Thalmann, "Robust tracking and segmentation of human motion in an image sequence," in *Acoustics, Speech, and Signal Processing, 2003. Proceedings. (ICASSP '03). 2003 IEEE International Conference on*, vol. 3, pp. III–29–32 vol.3, April 2003.

[32] L. Legrand, C. Bordier, A. Lalande, P. Walker, F. Brunotte, and C. Quantin, "Magnetic resonance image segmentation and heart motion tracking with an active mesh based system," in *Computers in Cardiology, 2002*, pp. 177–180, Sept 2002.

[33] C. del Blanco, F. Jaureguizar, L. Salgado, and N. Garcia, "Target detection through robust motion segmentation and tracking restrictions in aerial flir images," in *International Conference on Image Processing*, vol. 5, pp. V – 445–V – 448, Sept 2007.

[34] J. Rebut, A. Bensrhair, and G. Toulminet, "Image segmentation and pattern recognition for road marking analysis," in *Industrial Electronics, 2004 IEEE International Symposium on*, vol. 1, pp. 727–732 vol. 1, May 2004.

[35] J. Jiang, H. Wei, and Q. Qi, "Medical image segmentation based on biomimetic pattern recognition," in *Software Engineering, 2009. WCSE '09. WRI World Congress on*, vol. 2, pp. 375–379, May 2009.

[36] K. Strzecha, "Image segmentation algorithm based on statistical pattern recognition methods," in *CAD Systems in Microelectronics, 2001. CADSM 2001. Proceedings of the 6th International Conference. The Experience of Designing and Application of*, pp. 200–201, Feb 2001.

[37] X. Gongwen, Z. Zhijun, Y. Weihua, and X. Li'Na, "On medical image segmentation based on wavelet transform," in *Intelligent Systems Design and Engineering Applications (ISDEA), 2014 Fifth International Conference on*, pp. 671–674, June 2014.

[38] R. Ramya and K. Jayanthi, "Automatic image segmentation by graph cuts for bio-medical applications," in *Advances in Engineering, Science and Management (ICAESM), 2012 International Conference on*, pp. 392–395, March 2012.

[39] J. Zhu-Jacquot and R. Zabih, "Graph cuts segmentation with statistical shape priors for medical images," in *Signal-Image Technologies and Internet-Based System, 2007. SITIS '07. Third International IEEE Conference on*, pp. 631–635, Dec 2007.

[40] N. Dai, Y. Zhang, D. Xu, L. Hou, Y. Wei, W. Li, B. Fan, and Y. Xu, "Diagnostic performance of noninvasive cardiac imaging modalities to detect obstructive coronary artery disease," *International Journal of Cardiology*, vol. 168, no. 5, pp. 5057 – 5059, 2013.

[41] N. S. Khoo, E. B. Tham, and P. F. Kantor, "Newer imaging modalities in the assessment of heart function in single ventricle hearts," *Canadian Journal of Cardiology*, vol. 29, no. 7, pp. 886 – 889, 2013.

[42] K. Hirata, "Image modalities to assess cardiac tumors: Echocardiography, multidetector CT, and MR imaging," *Journal of Cardiology Cases*, vol. 8, no. 2, pp. e91 – e92, 2013.

[43] D. e. a. Mozaffarian, "Heart disease and stroke statistics2015 update: A report from the american heart association," *Circulation*, 2014.

[44] M. Sonka, X. Zhang, M. Siebes, M. S. Bissing, S. C. DeJong, S. M. Collins, and C. R. McKay, "Segmentation of intravascular ultrasound images: A knowledge-based approach," *T-MI*, vol. 14, no. 4, pp. 719–732, 1995.

[45] E. Essa, X. Xie, I. Sazonov, P. Nithiarasu, and D. Smith, "Shape prior model for media-adventitia border segmentation in IVUS using graph cut," in *MICCAI Medical Computer Vision Workshop*, 2012.

[46] G. Unal, S. Bucher, S. Carlier, G. Slabaugh, T. Fang, and K. Tanaka, "Shape-driven segmentation of the arterial wall in intravascular ultrasound images," *Information Technology in Biomedicine, IEEE Transactions on*, vol. 12, pp. 335–347, May 2008.

[47] N. Baka, C. Metz, C. Schultz, R.-J. van Geuns, W. Niessen, and T. van Walsum, "Oriented gaussian mixture models for nonrigid 2d/3d coronary artery registration," *Medical Imaging, IEEE Transactions on*, vol. 33, pp. 1023–1034, May 2014.

[48] C. Gatta, O. Pujol, O. Leor, J. Ferre, and P. Radeva, "Fast rigid registration of vascular structures in ivus sequences," *Information Technology in Biomedicine, IEEE Transactions on*, vol. 13, pp. 1006–1011, Nov 2009.

[49] C. Blondel, G. Malandain, R. Vaillant, and N. Ayache, "Reconstruction of coronary arteries from a single rotational x-ray projection sequence," *Medical Imaging, IEEE Transactions on*, vol. 25, pp. 653–663, May 2006.

[50] J. Yang, Y. Wang, Y. Liu, S. Tang, and W. Chen, "Novel approach for 3-d reconstruction of coronary arteries from two uncalibrated angiographic images," *Image Processing, IEEE Transactions on*, vol. 18, pp. 1563–1572, July 2009.

[51] K. Drechsler and C. Laura, "A novel multiscale integration approach for vessel enhancement," in *Computer-Based Medical Systems (CBMS), 2010 IEEE 23rd International Symposium on*, pp. 92–97, Oct 2010.

[52] F. Shi and J. Yang, "Multiscale vesselness based bilateral filter for blood vessel enhancement," *Electronics Letters*, vol. 45, pp. 1152–1154, November 2009.

[53] H. Sackey, H. Johansson, K. Sandelin, G. Liljegren, G. MacLean, J. Frisell, and Y. Brandberg, "Self-perceived, but not objective lymphoedema is associated with decreased long-term health-related quality of life after breast cancer surgery," *European Journal of Surgical Oncology (EJSO)*, vol. 41, no. 4, pp. 577 – 584, 2015.

[54] S. Bains, A. Stanton, V. Cintolesi, J. Ballinger, S. Allen, C. Zammit, J. Levick, P. Mortimer, A. Peters, and A. Purushotham, "A constitutional predisposition to breast cancer-related lymphoedema and effect of axillary lymph node surgery on forearm muscle lymph flow," *The Breast*, vol. 24, no. 1, pp. 68 – 74, 2015.

[55] D. Jones and W. Min, "An overview of lymphatic vessels and their emerging role in cardiovascular disease," *Journal of Cardiovascular Disease Research*, vol. 2, no. 3, pp. 141 – 152, 2011.

[56] S. Bhatia, *Biomaterials for Clinical Applications*. SpringerLink : Bücher, Springer New York, 2010.

[57] B. A. de Valois, T. E. Young, and E. Melsome, "Assessing the feasibility of using acupuncture and moxibustion to improve quality of life for cancer survivors with upper body lymphoedema," *European Journal of Oncology Nursing*, vol. 16, no. 3, pp. 301 – 309, 2012.

[58] M. Gennaro, M. Maccauro, C. Sigari, P. Casalini, L. Bedodi, A. Conti, A. Caraceni, and E. Bombardieri, "Selective axillary dissection after axillary reverse mapping to prevent breast-cancer-related lymphoedema," *European Journal of Surgical Oncology (EJSO)*, vol. 39, no. 12, pp. 1341 – 1345, 2013.

[59] R. Wijesinghe and A. Wickremasinghe, "Quality of life in filarial lymphoedema patients in colombo, sri lanka," *Transactions of the Royal Society of Tropical Medicine and Hygiene*, vol. 104, no. 3, pp. 219 – 224, 2010.

[60] R. M. F. de Moura, H. de Alencar Gomes, S. L. A. da Silva, R. R. Britto, and R. C. Dias, "Analysis of the physical and functional parameters of older adults with chronic venous disease," *Archives of Gerontology and Geriatrics*, vol. 55, no. 3, pp. 696 – 701, 2012.

[61] D. Martin, C. Fowlkes, D. Tal, and J. Malik, "A database of human segmented natural images and its application to evaluating segmentation algorithms and measuring ecological statistics," in *Proc. 8th Int'l Conf. Computer Vision*, vol. 2, pp. 416–423, July 2001.

[62] F. Zhao and X. Xie, "An overview of interactive medical image segmentation," in *Annals of the BMVA 2013(7)*, pp. 1–22, 2013.

[63] G. Huang and C.-M. Pun, "Interactive segmentation based on initial segmentation and region merging," in *Computer Graphics, Imaging and Visualization (CGIV), 2013 10th International Conference*, pp. 52–55, Aug 2013.

[64] J. Deng, X. Xie, R. Alcock, and C. Roobottom, "3d interactive coronary artery segmentation using random forests and markov random field optimization," in *International Conference on Image Processing*, pp. 942–946, Oct 2014.

[65] A. Falcao, J. Udupa, and F. Miyazawa, "An ultra-fast user-steered image segmentation paradigm: Live wire on the fly," in *IEEE Trans. Med. Imag., vol. 19, Jan.*, 2000.

[66] V. Lempitsky, P. Kohli, C. Rother, and T. Sharp, "Image segmentation with a bounding box prior," in *IEEE International Conference on Computer Vision*, 2009.

[67] Z. Cui, H. Zhang, and W. Zuo, "Interactive tongue body segmentation," in *Medical Biometrics, 2014 International Conference on*, pp. 26–31, May 2014.

[68] N. T. N. Anh, J. Cai, J. Zhang, and J. Zheng, "Constrained active contours for boundary refinement in interactive image segmentation," in *Circuits and Systems (ISCAS), 2012 IEEE International Symposium on*, pp. 870–873, May 2012.

[69] P. Elliott, J. Knapman, and W. Schlegel, "Interactive image segmentation for radiation treatment planning," *IBM Systems Journal*, vol. 31, no. 4, pp. 620–634, 1992.

[70] A. Saffari, C. Leistner, J. Santner, M. Godec, and H. Bischof, "On-line random forests," in *Computer Vision Workshops (ICCV Workshops), 2009 IEEE 12th International Conference on*, pp. 1393–1400, Sept 2009.

[71] Y. Boykov and M.-P. Jolly, "Interactive organ segmentation using graph cuts," in *International Conference on Medical Image Computing and Computer-Assisted Intervention*, pp. 276–286, 2000.

[72] J. Shi and J. Malik, "Normalized cuts and image segmentation," *IEEE Transactions on Pattern Analysis and Machine Intelligence*, vol. 22, no. 8, pp. 888–905, 2000.

[73] S. Menet, P. Saint-Marc, and G. Medioni, "Active contour models: overview, implementation and applications," in *Systems, Man and Cybernetics, 1990. Conference Proceedings., IEEE International Conference on*, pp. 194–199, Nov 1990.

[74] M. Kass, A. Witkin, and D. Terzopoulos, "Snakes: Active contour models," *International Journal of Computer Vision*, vol. 1, no. 4, 1988.

[75] N. Sharma and L. M. Aggarwal, "Automated medical image segmentation techniques,"

[76] F. Conversano, E. Casciaro, R. Franchini, S. Casciaro, and A. Lay-Ekuakille, "Fully automatic 3d segmentation measurements of human liver vessels from contrast-enhanced ct," in *Medical Measurements and Applications (MeMeA), 2014 IEEE International Symposium on*, pp. 1–5, June 2014.

[77] N. Ramesh, J.-H. Yoo, and I. Sethi, "Thresholding based on histogram approximation," *Vision, Image and Signal Processing, IEE Proceedings -*, vol. 142, pp. 271–279, Oct 1995.

[78] P. Papachristou, M. Petrou, and J. Kittler, "Edge postprocessing using probabilistic relaxation," *Systems, Man, and Cybernetics, Part B: Cybernetics, IEEE Transactions on*, vol. 30, pp. 383–402, Jun 2000.

[79] E. Hancock and J. Kittler, "Edge-labeling using dictionary-based relaxation," *Pattern Analysis and Machine Intelligence, IEEE Transactions on*, vol. 12, pp. 165–181, Feb 1990.

[80] Y.-T. Liow, "A contour tracing algorithm that preserves common boundaries between regions," *CVGIP: Image Understanding*, vol. 53, no. 3, pp. 313 – 321, 1991.

[81] S. Nandagopalan, B. Adiga, C. Dhanalakshmi, and N. Deepak, "Automatic segmentation and ventricular border detection of 2d echocardiographic images combining k-means clustering and active contour model," in *Computer and Network Technology (ICCNT), 2010 Second International Conference on*, pp. 447–451, April 2010.

[82] J. Dijkstra, G. Koning, J. Tuinenburg, P. Oemrawsingh, and J. Reiber, "Automatic border detection in intravascular iltrasound images for quantitative measurements of the vessel, lumen and stent parameters," in *Computers in Cardiology 2001*, pp. 25–28, 2001.

[83] S. Zhang and H. Jing, "Fast log-gabor-based nonlocal means image denoising methods," in *International Conference on Image Processing*, pp. 2724–2728, Oct 2014.

[84] Z. Shi and J. Hu, "An adaptive switching median filter with anisotropic linking pcnn noise detection for salt and pepper noise reduction," in *Nature and Biologically Inspired Computing (NaBIC), 2010 Second World Congress on*, pp. 233–238, Dec 2010.

[85] C. Tatanun, P. Ritthipravat, T. Bhongmakapat, and L. Tuntiyatorn, "Automatic segmentation of nasopharyngeal carcinoma from ct images: Region growing based technique," in *Signal Processing Systems (ICSPS), 2010 2nd International Conference on*, vol. 2, pp. V2–537–V2–541, July 2010.

[86] L. Zha, Z. Liu, S. Luo, and L. Shen, "A novel region merging based image segmentation approach for automatic object extraction," in *Circuits and Systems (ISCAS), 2013 IEEE International Symposium on*, pp. 970–973, May 2013.

[87] W. Xiong, S. Ong, and J. H. Lim, "A recursive and model-constrained region splitting algorithm for cell clump decomposition," in *Pattern Recognition (ICPR), 2010 20th International Conference on*, pp. 4416–4419, Aug 2010.

[88] S. Vigus, D. Bull, and C. Canagarajah, "Video object tracking using region split and merge and a kalman filter tracking algorithm," in *Image Processing, 2001. Proceedings. 2001 International Conference on*, vol. 1, pp. 650–653 vol.1, 2001.

[89] R. Haralick, "Statistical and structural approaches to texture," *Proceedings of the IEEE*, vol. 67, pp. 786–804, May 1979.

[90] C. Scharfenberger, A. Wong, and D. Clausi, "Structure-guided statistical textural distinctiveness for salient region detection in natural images," *Image Processing, IEEE Transactions on*, vol. 24, pp. 457–470, Jan 2015.

[91] H. Park, G. Martin, and A. Bhalerao, "Structural texture segmentation using affine symmetry," in *International Conference on Image Processing*, vol. 2, pp. 49–52, Sept 2007.

[92] P. Choorat, W. Chiracharit, and K. Chamnongthai, "A single tooth segmentation using structural orientations and statistical textures," in *Biomedical Engineering International Conference (BMEiCON), 2011*, pp. 294–297, Jan 2011.

[93] X. Liu and D. Wang, "Image and texture segmentation using local spectral histograms," *Image Processing, IEEE Transactions on*, vol. 15, pp. 3066–3077, Oct 2006.

[94] L. Zhang and Q. Ji, "A bayesian network model for automatic and interactive image segmentation," *Image Processing, IEEE Transactions on*, vol. 20, pp. 2582–2593, Sept 2011.

[95] M. Kim and Y.-S. Ho, "Semi-automatic segmentation by a double labeling method," in *TENCON 99. Proceedings of the IEEE Region 10 Conference*, vol. 1, pp. 746–749 vol.1, 1999.

[96] X. Zhang, B. Wang, M. Wang, and B. Liu, "An integration of top-down and bottom-up visual attention for categorization of natural scene images," in *Machine Learning and Cybernetics (ICMLC), 2010 International Conference on*, vol. 2, pp. 692–697, July 2010.

[97] E. d. S. Filho, M. Yoshizawa, A. Tanaka, Y. Saijo, and T. Iwamoto, "Moment-based texture segmentation of luminal contour in intravascular ultrasound images," *Journal of Medical Ultrasonics*, vol. 32, no. 3, pp. 91–99, 2005.

131

[98]   A. Vard, K. Jamshidi, and N. Movahhedinia, "An automated approach for segmentation of intravascular ultrasound images based on parametric active contour models," *Australasian Physical & Engineering Sciences in Medicine*, vol. 35, no. 2, pp. 135–150, 2012.

[99]   M. Papadogiorgaki, V. Mezaris, Y. S. Chatzizisis, G. D. Giannoglou, and I. Kompatsiaris, "Image analysis techniques for automated ivus contour detection.," *Ultrasound Med Biol*, vol. Sep;34(9), 2008.

[100] E. Borenstein and S. Ullman, "Combined top-down/bottom-up segmentation," *Pattern Analysis and Machine Intelligence, IEEE Transactions on*, vol. 30, pp. 2109–2125, Dec 2008.

[101] A. Wahle, H. Oswald, G.-A. Schulze, J. Beier, and E. Fleck, "3-d reconstruction, modelling and viewing of coronary vessels," in *Computer Assisted Radiology / Computergesttzte Radiologie* (H. Lemke, M. Rhodes, C. Jaffe, and R. Felix, eds.), pp. 669–676, Springer Berlin Heidelberg, 1991.

[102] H. Khaleel, R. Rahmat, D. Zamrin, R. Mahmod, and N. Mustapha, "3d surface reconstruction of coronary artery trees for vessel location and detection," *Arabian Journal for Science and Engineering*, vol. 39, no. 3, pp. 1749–1773, 2014.

[103] C. V. Bourantas, I. C. Kourtis, M. E. Plissiti, D. I. Fotiadis, C. S. Katsouras, M. I. Papafaklis, and L. K. Michalis, "A method for 3D reconstruction of coronary arteries using biplane angiography and intravascular ultrasound images," *Comput Med Imaging Graph*, pp. 597–606, 2005.

[104] L. Sherwood, "Human physiology: From cells to systems," 2012.

[105] A. Katouzian, E. D. Angelini, S. G. Carlier, J. S. Suri, N. Navab, and A. F. Laine, "A state-of-the-art review on segmentation algorithms in intravascular ultrasound (IVUS) images," *IEEE Trans. Info. Tech. in Biomed.*, vol. 16, no. 5, pp. 823–834, 2012.

[106] S. Y. Lee and M. K. Hong, "Stent evaluation with optical coherence tomography," *Yonsei Med J.*, pp. 1075–83, 2013.

[107] D. Huang, E. Swanson, C. P. Lin, J. S. Schuman, W. G. Stinson, W. Chang, and et al, "Optical coherence tomography," *Science*, pp. 1178–81, 1991.

[108] M. C. Moraes and S. S. Furuie, "An automatic media-adventitia border segmentation approach for ivus images," in *Computing in Cardiology*, pp. 389–392, 2010.

[109] L. Atahnasiou, C. Bourantas, G. Rigas, and T. Exarchos, "Fully automated calcium detection using optical coherence tomography," in *Engineering in Medicine and Biology Society (EMBC), 2013 35th Annual International Conference of the IEEE*, pp. 1430–1433, 2013.

[110] E. Essa, X. Xie, I. Sazonov, P. Nithiarasu, and D. Smith, "Shape prior model for media-adventitia border segmentation in ivus using graph cut," *LNCS, Medical Computer Vision. Recognition Techniques and Applications in Medical Imaging*, vol. 7766, pp. 114–123, 2013.

[111] K.-P. Tung, W.-Z. Shi, D. S. R., and E. E., "Automatical vessel wall detection in intravascular coronary oct," in *Biomedical Imaging: From Nano to Macro, 2011 IEEE International Symposium on*, pp. 610–613, 2011.

[112] J. Pawley, "Handbook of biological confocal microscopy," 2008.

[113] I. Riomoros, M. Guijarro, G. Pajares, P. Herrera, X. Burgos-Artizzu, and A. Ribeiro, "Automatic image segmentation of greenness in crop fields," in *Soft Computing and Pattern Recognition (SoCPaR), 2010 International Conference of*, pp. 462–467, Dec 2010.

[114] G. Baugh and A. Kokaram, "Feature-based object modelling for visual surveillance," in *International Conference on Image Processing*, pp. 1352–1355, Oct 2008.

[115] D. Lesage, E. D. Angelini, I. Bloch, and G. Funka-Lea, "A review of 3d vessel lumen segmentation techniques: Models, features and extraction schemes," *Medical Image Analysis*, vol. 13, no. 6, pp. 819 – 845, 2009.

[116] C. Kirbas and F. Quek, "Vessel extraction techniques and algorithms: a survey," in *Bioinformatics and Bioengineering, 2003. Proceedings. Third IEEE Symposium on*, pp. 238–245, March 2003.

[117] J. Vandenberg, G. Liersch, H. Hanna, and J. Cameron, "Fully automated media and lumen boundary detection in intravascular ultrasound images," in *Image Analysis and*

Interpretation, 1996., Proceedings of the IEEE Southwest Symposium on, pp. 71–75, Apr 1996.

[118] L. J. Reese, "Intelligent paint: Region-based interactive image segmentation," *Masters Thesis, Department of Computer Science, Brigham Young University*, 1999.

[119] K. Humnabadkar, S. Singh, D. Ghosh, and P. Bora, "Unsupervised active contour model for biological image segmentation and analysis," in *Instrumentation and Measurement Technology Conference (I2MTC) Proceedings, 2014 IEEE International*, pp. 1443–1448, 2014.

[120] X. Xie and M. Mirmehdi, "Magnetostatic field for the active contour model: A study in convergence," in *Proceedings of the 17th British Machine Vision Conference*, pp. 127–136, 2008.

[121] A. K. Sinop and L. Grady, "A seeded image segmentation framework unifying graph cuts and random walker which yields a new algorithm," in *IEEE International Conference on Computer Vision*, pp. 1–8, 2007.

[122] L. Cohen and R. Kimmel, "Global minimum for active contour models: A minimal path approach," *IJCV*, vol. 24, no. 1, pp. 57–78, 1997.

[123] M. Mulet-Parada and J. A. Noble, "2D + T acoustic boundary detection in echocardiography," *MIA*, vol. 4, no. 1, pp. 21–30, 2000.

[124] F. Rizi and S. Setarehdan, "Noise reduction in intravascular ultrasound images using curvelet transform and adaptive complex diffusion filter: A comparative study," in *Electrical Engineering (ICEE), 2012 20th Iranian Conference on*, pp. 1549–1553, May 2012.

[125] H. Lazrag and M. Naceur, "Wavelet filters analysis for speckle reduction in intravascular ultrasound images," in *Sciences of Electronics, Technologies of Information and Telecommunications (SETIT), 2012 6th International Conference on*, pp. 375–379, March 2012.

[126] W. Yang, J. Cai, J. Zheng, and J. Luo, "User-friendly interactive image segmentation through unified combinatorial user inputs," *Image Processing, IEEE Transactions on*, vol. 19, pp. 2470–2479, Sept 2010.

[127] D. Freedman and T. Zhang, "Interactive graph cut based segmentation with shape priors," in *CVPR*, pp. 755–762, 2005.

[128] J. Malcolm, Y. Rathi, and A. Tannenbaum, "Graph cut segmentation with nonlinear shape priors," in *International Conference on Image Processing*, pp. 365–368, 2007.

[129] N. Vu and B. S. Manjunath, "Shape prior segmentation of multiple objects with graph cuts," in *CVPR*, pp. 1–8, 2008.

[130] V. Gulshan, C. Rother, A. Criminisi, A. Blake, and A. Zisserman, "Geodesic star convexity for interactive image segmentation," in *CVPR*, pp. 3129–3136, 2010.

[131] O. Duchenne, J.-Y. Audibert, R. Keriven, J. Ponce, and F. Segonne, "Segmentation by transduction," in *CVPR*, pp. 1–8, 2008.

[132] S. Fischer, G. Cristobal, and R. Redondo, "Sparse overcomplete gabor wavelet representation based on local competitions," *Image Processing, IEEE Transactions on*, vol. 15, pp. 265–272, Feb 2006.

[133] J. Arrospide and L. Salgado, "Log-gabor filters for image-based vehicle verification," *Image Processing, IEEE Transactions on*, vol. 22, pp. 2286–2295, June 2013.

[134] H. David and T. Athira, "Improving the performance of vehicle detection and verification by log gabor filter optimization," in *Advances in Computing and Communications (ICACC), 2014 Fourth International Conference on*, pp. 50–55, Aug 2014.

[135] S. Mohsin, M. Javed, and A. Anjum, "Face recognition using bank of gabor filters," in *Emerging Technologies, 2006. ICET '06. International Conference on*, pp. 144–150, Nov 2006.

[136] N. Rose, "Facial expression classification using gabor and log-gabor filters," in *Automatic Face and Gesture Recognition, 2006. FGR 2006. 7th International Conference on*, pp. 346–350, April 2006.

[137] V. Struc, R. Gajsek, and N. Paves?ic, "Principal gabor filters for face recognition," in *Biometrics: Theory, Applications, and Systems, 2009. BTAS '09. IEEE 3rd International Conference on*, pp. 1–6, Sept 2009.

[138] P. Yao, J. Li, X. Ye, Z. Zhuang, and B. Li, "Iris recognition algorithm using modified log-gabor filters," in *Pattern Recognition, 2006. ICPR 2006. 18th International Conference on*, vol. 4, pp. 461–464, 2006.

[139] R. Nemati and M. Javed, "Fingerprint verification using filter-bank of gabor and log gabor filters," in *Systems, Signals and Image Processing, 2008. IWSSIP 2008. 15th International Conference on*, pp. 363–366, June 2008.

[140] S. Mahmoud, "Recognition of arabic (indian) check digits using spatial gabor filters," in *GCC Conference Exhibition, 2009 5th IEEE*, pp. 1–5, March 2009.

[141] J. Fang, K. Xiao, C. Wang, and M. Mo, "Binarized gabor filters based illumination invariant chinese character recognition," in *Mechatronics and Automation, 2009. ICMA 2009. International Conference on*, pp. 4976–4980, Aug 2009.

[142] D. J. Field, "Relations between the statistics of natural images and the response properties of cortical cells," *J. Opt. Soc. Am. A*, vol. 4, pp. 2379–2394, 1987.

[143] J. G. Daugman, "Uncertainty relation for resolution in space, spatial frequency, and orientation optimized by two-dimensional visual cortical filters," *J. Opt. Soc. Am. A*, vol. 7, pp. 1160–9, 1985.

[144] L. Jiangping and W. Yuke, "A shortest path algorithm of image segmentation based on fuzzy-rough grid," in *Computational Intelligence and Software Engineering, 2009. CiSE 2009. International Conference on*, pp. 1–4, Dec 2009.

[145] L. Chen, Y. Ju, S. Ding, and X. Liu, "Topological vascular tree segmentation for retinal images using shortest path connection," in *International Conference on Image Processing*, pp. 2137–2140, Sept 2011.

[146] G. Ulaganathan, A. Banumathi, J. Amutha, and A. Jeevani Selvabala, "Dental cyst delineation using live wire algorithm," in *Machine Vision and Image Processing (MVIP), 2012 International Conference on*, pp. 129–132, Dec 2012.

[147] M. Xu, J. Wang, and Z. Yu, "Image edge enhancement and segmentation via randomized shortest paths," in *Biomedical Engineering and Informatics (BMEI), 2012 5th International Conference on*, pp. 290–294, Oct 2012.

[148] E. W. Dijkstra, "A note on two problems in connexion with graphs," *Numerische Mathematik*, vol. 1, pp. 269–271, 1959.

[149] M. Fredman and R. Tarjan, "Fibonacci heaps and their uses in improved network optimization algorithms," *2013 IEEE 54th Annual Symposium on Foundations of Computer Science*, vol. 0, pp. 338–346, 1984.

[150] S. Wang, "A review of gradient-based and edge-based feature extraction methods for object detection," in *Computer and Information Technology (CIT), 2011 IEEE 11th International Conference on*, pp. 277–282, Aug 2011.

[151] K. Somkantha, N. Theera-Umpon, and S. Auephanwiriyakul, "Boundary detection in medical images using edge following algorithm based on intensity gradient and texture gradient features," *Biomedical Engineering, IEEE Transactions on*, vol. 58, pp. 567–573, March 2011.

[152] Z. Yu-qian, G. Wei-hua, C. Zhen-cheng, T. Jing-tian, and L. Ling-yun, "Medical images edge detection based on mathematical morphology," in *Engineering in Medicine and Biology Society, 2005. IEEE-EMBS 2005. 27th Annual International Conference of the*, pp. 6492–6495, Jan 2005.

[153] M. Kunt, "Edge detection : A tuttorial review," in *Acoustics, Speech, and Signal Processing, IEEE International Conference on ICASSP '82.*, vol. 7, pp. 1172–1175, May 1982.

[154] W. Gao, X. Zhang, L. Yang, and H. Liu, "An improved sobel edge detection," in *Computer Science and Information Technology (ICCSIT), 2010 3rd IEEE International Conference on*, vol. 5, pp. 67–71, July 2010.

[155] T. Lindeberg, "Edge detection and ridge detection with automatic scale selection," in *Computer Vision and Pattern Recognition, 1996. Proceedings CVPR '96, 1996 IEEE Computer Society Conference on*, pp. 465–470, Jun 1996.

[156] W. Zhang and F. Bergholm, "Multi-scale blur estimation and edge type classification for scene analysis," *International Journal of Computer Vision*, vol. 24, pp. 219 – 250.

[157] G. Rezai-rad and M. Aghababaie, "Comparison of susan and sobel edge detection in mri images for feature extraction," in *Information and Communication Technologies, 2006. ICTTA '06. 2nd*, vol. 1, pp. 1103–1107, 2006.

[158] Z. Jin-Yu, C. Yan, and H. Xian-xiang, "Edge detection of images based on improved sobel operator and genetic algorithms," in *Image Analysis and Signal Processing, 2009. IASP 2009. International Conference on*, pp. 31–35, April 2009.

[159] C. Pradabpet, N. Ravinu, S. Chivapreecha, B. Knobnob, and K. Dejhan, "An efficient filter structure for multiplierless sobel edge detection," in *Innovative Technologies in Intelligent Systems and Industrial Applications, 2009. CITISIA 2009*, pp. 40–44, July 2009.

[160] J. Canny, "A computational approach to edge detection," *Pattern Analysis and Machine Intelligence, IEEE Transactions on*, vol. IEEE Transactions on Pattern Analysis and Machine Intelligence, pp. 679–698, Nov 1986.

[161] A. Koschan and M. Abidi, "Detection and classification of edges in color images," *Signal Processing Magazine, IEEE*, vol. 22, pp. 64–73, Jan 2005.

[162] Z. Huan, L. Xiuhuan, and Y. Lilei, "Shot boundary detection based on mutual information and canny edge detector," in *Computer Science and Software Engineering, 2008 International Conference on*, vol. 2, pp. 1124–1128, Dec 2008.

[163] V. Mall, A. Roy, S. Mitra, and S. Shukla, "Detection of structural tampering in a digital image using canny edge detector," in *Informatics, Electronics Vision (ICIEV), 2013 International Conference on*, pp. 1–7, May 2013.

[164] Z. Hocenski, S. Vasilic, and V. Hocenski, "Improved canny edge detector in ceramic tiles defect detection," in *IEEE Industrial Electronics, IECON 2006 - 32nd Annual Conference on*, pp. 3328–3331, Nov 2006.

[165] R. Sidhu, "Improved canny edge detector in various color spaces," in *Reliability, Infocom Technologies and Optimization (ICRITO) (Trends and Future Directions), 2014 3rd International Conference on*, pp. 1–6, Oct 2014.

[166] C. H. Chen and A. Gangidi, "Automatic segmentation of intravascular ultrasound images based on temporal texture analysis," in *Computing in Cardiology Conference (CinC), 2014*, pp. 957–960, Sept 2014.

[167] H. Yu, T.-Y. Lee, I.-C. Yeh, X. Yang, W. Li, and J. Zhang, "An rbf-based reparameterization method for constrained texture mapping," *Visualization and Computer Graphics, IEEE Transactions on*, vol. 18, pp. 1115–1124, July 2012.

[168] D. Kai Tik Chow and T. Lee, "Image approximation and smoothing by support vector regression," in *Neural Networks, 2001. Proceedings. IJCNN '01. International Joint Conference on*, vol. 4, pp. 2427–2432, 2001.

[169] H. Y. Wang, Q. B. Zheng, and Z. Q. Xu, "An improved rbf deforming algorithm in 3d face morphable model," in *Information Science and Engineering (ICISE), 2010 2nd International Conference on*, pp. 989–992, Dec 2010.

[170] X. Wu, M. Yu, and W. Q. Xia, "Implicit fitting and smoothing using radial basis functions with partition of unity," in *Computer Aided Design and Computer Graphics, 2005. Ninth International Conference on*, p. 10, Dec 2005.

[171] M. Grum and A. Bors, "3-d scene modelling from multiple images using radial basis function networks," in *Machine Learning for Signal Processing, 2007 IEEE Workshop on*, pp. 105–110, Aug 2007.

[172] W. Fuller, "Introduction to probability theory and its applications," vol. Vol II (2nd edition), pp. 9–20, 1971.

[173] R. L., "A tutorial on hidden markov models and selected applications in speech recognition," in *Proceedings of the IEEE 77(2)*, pp. 257–286, 1989.

[174] J. B.-H., "On the hidden markov model and dynamic time warping for speech recognition a unified view," pp. 1213–1243, 1984.

[175] A. Lacey, J. Deng, and X. Xie, "Protein classification using hidden markov models and randomised decision trees," in *Proc. BMEI*, pp. 659–664, 20124.

[176] S. Mansor and J. Noble, "Local wall motion classifcation of stress echocardiography using a hidden markov model approach," in *ISBI*, 2008.

[177] Y. Chen, Y. Rui, and T. Huang, "JPDAF based HMM for real-time contour tracking," in *CVPR*, 2001.

[178] Y. Chen, Y. Rui, and T. Huang, "Multicue HMM-UKF for real-time contour tracking," in *IEEE Transactions on Pattern Analysis and Machine Intelligence*, vol. 28(9), pp. 1525–1529, 2006.

[179] S. AlZubi, N. Islam, and M. Abbod, "Enhanced hidden markov models for accelerating medical volumes segmentation," in *GCC Conference and Exhibition*, pp. 287–290, 2011.

[180] Y. Zhang, M. Brady, and S. Smith, "Segmentation of brain mr images through a hidden markov random field model and the expectation-maximization algorithm," *Medical Imaging, IEEE Transactions on*, vol. 20, pp. 45–57, Jan 2001.

[181] Z. Jixiang, Z. Xiangling, and P. Zhijun, "Medical image denoising using hierarchical hidden markov model in the wavelet domain," in *ECTS Workshop (Volume:2)*, pp. 857–860, 2009.

[182] Z. Ghahramani, "An introduction to hidden markov models and bayesian networks," *International Journal of Pattern Recognition and Artificial Intelligence*, vol. 15, no. 01, pp. 9–42, 2001.

[183] K. M. Mullen, "Continuous global optimization in R," *Journal of Statistical Software*, vol. 60, no. 6, pp. 1–45, 2014.

[184] J. Lee, "A first course in combinatorial optimization," *Cambridge Texts in Applied Mathematics*, vol. 36, 2004.

[185] P. T. Unger M. and B. H., "Global relabeling for continuous optimization in binary image segmentation," in *Energy Minimization Methods in Computer Vision and Pattern Recognition*, pp. 104–117, 2011.

[186] G. Strang, "Maximal flow through a domain," *Mathematical Programming*, vol. 26, no. 2, pp. 123–143, 1983.

[187] S. Balocco, O. Basset, C. Cachard, and P. Delachartre, "Spatial anisotropic diffusion and local time correlation applied to segmentation of vessels in ultrasound image sequences," in *Ultrasonics, 2003 IEEE Symposium on*, vol. 2, pp. 1549–1552 Vol.2, Oct 2003.

[188] M. Holzer, F. Schulz, and D. Wagner, "Engineering multilevel overlay graphs for shortest-path queries," *J. Exp. Algorithmics*, vol. 13, pp. 5:2.5–5:2.26, 2009.

[189] D. Wagner and T. Willhalm, "Geometric speed-up techniques for finding shortest paths in large sparse graphs," *European Symposiumm on Algorithms (ESA)*, vol. 2832, pp. 776–787, 2003.

[190] B. Fulkerson, A. Vedaldi, and S. Soatto, "Class segmentation and object localization with superpixel neighborhoods," in *IEEE International Conference on Computer Vision*, pp. 670–677, 2009.

[191] A. Moore, S. J. D. Prince, and J. Warrell, "Lattice cut - constructing superpixels using layer constraints," in *CVPR*, pp. 2117–2124, 2010.

[192] D. Comaniciu and P. Meer, "Mean shift: a robust approach toward feature space analysis," *IEEE Transactions on Pattern Analysis and Machine Intelligence*, vol. 24, no. 5, pp. 603–619, 2002.

[193] L. Vincent and P. Soille, "Watersheds in digital spaces: an efficient algorithm based on immersion simulations," *IEEE Transactions on Pattern Analysis and Machine Intelligence*, vol. 13, no. 6, pp. 583–598, 1991.

[194] D. Comaniciu, V. Ramesh, and P. Meer, "Real-time tracking of non-rigid objects using mean shift," in *CVPR*, pp. 142–149, 2000.

[195] Z. Luo, Y. Wang, and W. Wang, "Estimating coronary artery lumen area with optimization-based contour detection," *T-MI*, vol. 22, no. 4, pp. 564–566, 2003.

[196] A. Katouzian, E. D. Angelini, B. Sturm, and A. F. Laine, "Automatic detection of luminal borders in ivus images by magnitude-phase histograms of complex brushlet coefficients," in *EMBC*, pp. 3072–3076, 2010.

[197] P. A. Brathwaite, K. B. Chandran, D. D. McPherson, and E. L. Dove, "Lumen detection in human IVUS images using region-growing," in *Computers in Cardiology*, pp. 37–40, 1996.

[198] A. Takagi, K. Hibi, X. Zhang, T. Teo, H. N. Bonneau, P. G. Yock, and P. J. Fitzgerald, "Automated contour detection for high frequency intravascular ultrasound imaging: A

technique with blood noise reduction for edge enhancement," in *Ultrasound Med Biol 2000*, pp. 1033–1041, 2000.

[199] L. Meziou, A. Histace, F. Precioso, B. J. Matuszewski, and M. F. Murphy, "Confocal microscopy segmentation using active contour based on alpha(α)-divergence," in *International Conference on Image Processing*, pp. 3077–3080, 2011.

[200] A. Mondal, S. Ghosh, and A. Ghosh, "Efficient silhouette based contour tracking," in *ICACCI*, pp. 1781–1786, 2013.

[201] H. Aljuaid and D. Mohamad, "Object tracking simulates babysitter vision robot using gmm," in *SoCPaR; Hanoi*, pp. 60–65, 2013.

[202] D. Beymer and K. Konolige, "Real-time tracking of multiple people using continuous detection," in *ICCV Frame-Rate Workshop*, 1999.

[203] L. Xie, G. Zhu, Y. Wang, H. Xu, and Z. Zhang, "Real-time vehicles tracking based on kalman filter in a video-based its," in *ICCCAS (Volume 2)*.

[204] P. Abolmaesumi, M. Sirouspour, and S. Salcudean, "Real-time extraction of carotid artery contours from ultrasound images," in *CBMS*, 2000.

[205] J. Cheng, S. Foo, and S. Krishnan, "Watershed-presegmented snake for boundary detection and tracking of left ventricle in echocardiographic images," in *IEEE T-ITB 10(2)*, pp. 414–416, 2006.

[206] T. Behrens, K. Rohr, and H. Stiehl, "Robust segmentation of tubular structures in 3-d medical images by parametric object detection and tracking. systems, man, and cybernetics, part b," in *IEEE Trans. Cybern. (Volume:33 , Issue: 4)*, 2003.

[207] J.-L. Jones, E. Essa, X. Xie, and J. Cotton, "Interactive segmentation of lumen border in OCT," in *CMBE*, 2013.

[208] J.-L. Jones, X. Xie, and E. Essa, "Combining region-based and imprecise boundary-based cues for interactive medical image segmentation," *Int J Numer Method Biomed Eng, volume 30, issue 12*, p. 16491666, 2014.

[209] A. Schenk, G. Prause, and H.-O. Peitgen, "Local cost computation for efficient segmentation of 3d objects with live wire," in *Proc. SPIE Int'l Symp. Medical Imaging: Image Processing, vol. 4322*, pp. 1357–1364, 2001.

[210] A. Falco and J. Udupa, "A 3D generalization of user-steered live-wire segmentation," in *Med Image Anal, vol. 4*, pp. 389–402, 2000.

[211] C. Aldasoro and A. Bhalerao, "Volumetric texture segmentation by discriminant feature selection and multiresolution classification," *Medical Imaging, IEEE Transactions on*, vol. 26, pp. 1–14, Jan 2007.

[212] L. K., W. X., D. Chen, and M. Sonka, "Optimal surface segmentation in volumetric images-a graph-theoretic approach," in *IEEE Transactions on Pattern Analysis and Machine Intelligence*, vol. Volume:28, Issue: 1, pp. 119–134, 2006.

[213] Y. Chen, L. Wang, L. Shi, D. Wang, P.-A. Heng, T.-T. Wong, and X. Li, "Structure-preserving multiscale vessel enhancing diffusion filter," in *International Conference on Image Processing*, pp. 3565–3568, Sept 2010.

[214] R. Manniesing, M. Viergever, and W. Niessen, "Vessel enchancing diffusion," in *Med Image Anal, Volume 10, Issue 6*, pp. 815–825, 2006.

[215] W. T. Freeman and E. H. Adelson, "The design and use of steerable filters," in *IEEE Transactions on Pattern Analysis and Machine Intelligence*, vol. vol. 13, no. 9, pp. 891–906, 1991.

[216] A. Viterbi, "Error bounds for convolutional codes and an asymptotically optimum decoding algorithm," *Information Theory, IEEE Transactions on*, vol. 13, pp. 260–269, April 1967.

[217] D. S. Hochbaum, "50th anniversary article: Selection, provisioning, shared fixed costs, maximum closure, and implications on algorithmic methods today," *Management Science*, vol. 50, no. 6, pp. 709–723, 2004.

[218] Q. Song, J. Bai, M. Garvin, M. Sonka, J. Buatti, and X. Wu, "Optimal multiple surface segmentation with shape and context priors," *Medical Imaging, IEEE Transactions on*, vol. 32, pp. 376–386, Feb 2013.

[219] X. Wu and D. Chen, "Optimal net surface problems with applications," in *Automata, Languages and Programming* (P. Widmayer, S. Eidenbenz, F. Triguero, R. Morales, R. Conejo, and M. Hennessy, eds.), vol. 2380 of *Lecture Notes in Computer Science*, pp. 1029–1042, Springer Berlin Heidelberg, 2002.

[220] D. S. Hochbaum, "An efficient algorithm for image segmentation, markov random fields and related problems," *J. ACM*, vol. 48, pp. 686–701, July 2001.

[221] Y. Boykov and V. Kolmogorov, "An experimental comparison of min-cut/max- flow algorithms for energy minimization in vision," *Pattern Analysis and Machine Intelligence, IEEE Transactions on*, vol. 26, pp. 1124–1137, Sept 2004.

[222] C. J. Armstrong, W. A. Barrett, and B. Price, *All Theses and Dissertations*, vol. 1029, ch. Live surface. The Eurographics Association, 2007.

[223] G. Wagenknecht, A. Poll, M. Losacker, I. Blockx, and A. Van der Linden, "A new combined live wire and active surface approach for volume-of-interest segmentation," in *Nuclear Science Symposium Conference Record (NSS/MIC), 2009 IEEE*, pp. 3688–3692, Oct 2009.

[224] W. Wieclawek and E. Pietka, "Live-wire-based 3d segmentation method," in *Engineering in Medicine and Biology Society, 2007. EMBS 2007. 29th Annual International Conference of the IEEE*, pp. 5645–5648, Aug 2007.

[225] M. Krueger, P. Delmas, and G. Gimel'farb, "On 3d face feature segmentation using implicit surface active contours," in *Image and Vision Computing New Zealand, 2008. IVCNZ 2008. 23rd International Conference*, pp. 1–6, Nov 2008.

[226] B. Appleton and H. Talbot, "Globally minimal surfaces by continuous maximal flows," *Pattern Analysis and Machine Intelligence, IEEE Transactions on*, vol. 28, pp. 106–118, Jan 2006.

[227] X. Dou, X. Wu, A. Wahle, and M. Sonka, "Globally optimal surface segmentation using regional properties of segmented objects," in *Computer Vision and Pattern Recognition, 2008. CVPR 2008. IEEE Conference on*, pp. 1–8, June 2008.

144

[228] Q. Song, X. Wu, Y. Liu, M. Sonka, and M. Garvin, "Simultaneous searching of globally optimal interacting surfaces with shape priors," in *Computer Vision and Pattern Recognition (CVPR), 2010 IEEE Conference on*, pp. 2879–2886, June 2010.

[229] I. Bitter, A. Kaufman, and M. Sato, "Penalized-distance volumetric skeleton algorithm," *Visualization and Computer Graphics, IEEE Transactions on*, vol. 7, pp. 195–206, Jul 2001.